REVISTA CUBANA DE FÍSICA
vol. 29, No. 1E (Ago. 2012)

COVER: Group photo of the participants in "Complex Matter Physics: materials, dynamics and patterns" (March*COM*eeting'12) celebrated in Havana from March 6 to 9, 2012. The picture was taken at the entrance of the University of Havana on March 8, 2012 (Photo: O. Ramos)

La Revista Cubana de Física es una publicación semestral de la Sociedad Cubana de Física

COORDINATES

INTERVIEW

CONTRIBUTIONS

TRUE COMPLEXITY

For some, a meeting on Complexity is like a big sack where can you put whatever you like. Eventually that approach results in a disjoint collection of subjects, were the only common feature is that each author has conveniently sprinkled some of the "magic keywords" to his/her talk or poster, such as "emergent phenomena", "strange attractor" or "self-organization".

We did our best to circumvent that risk in "Complex Matter Physics: materials, dynamics and patterns" (March*COM*eeting'12), celebrated in Havana from March 6 to 9, 2012.

Indeed, the papers presented at the meeting shared important aspects beyond the use of some "magic keywords". In addition to the aim to quantify and model phenomena using mathematical and computational tools, most subjects approached are strongly nonlinear, and contain many degrees of freedom, and the majority of the papers presented deal with applying the notions of unifying complexity to interconnected physical phenomena occurring in materials.

It is fair to say that March*COM*eeting'12 was possible due to the extraordinary support of the Centre for Advanced Study at the Norwegian Academy of Sciences and Letters (CAS) under the project "Complex Matter Science", headed by T. H. Johansen, and also to the contribution of the "Abdus Salam" International Centre for Theoretical Physics (ICTP). The Physics Faculty and the IMRE (University of Havana), as well as the Cuban Physical Society, should be also thanked for their support.

But the key element for the celebration of the meeting was the enthusiastic will to go ahead with the project of most participants: 60 talks and 33 posters where presented by 75 scientists and students from 11 countries, where Cuba (23), Norway (17), France (14) and the U. S. (8) stood out.

The special number of the Revista Cubana de Física that we are presenting here includes 18 papers submitted by the participants, in addition to an interview given by L. Kadanoff, who was assigned the opening talk of the meeting.

March*COM*eeting'12 showed to be an excellent scenario for scientific and human exchange -for one thing, the biggest meeting ever between Norwegian and Cuban physicists. We hope that similar rendezvous will take place in the future.

Ernesto Altshuler
Jon Otto Fossum
Editors

A CONVERSATION WITH LEO KADANOFF

by E. Altshuler

Well known physicist Leo Kadanoff (James Frank Institute, University of Chicago) had an active participation at March*COM*eeting'12: he gave the opening lecture, and also headed the Committee for the selection of the Best Poster. In the short conversation below, we find his opinions on different aspects of contemporary Physics, from "grand unification efforts", to Physics in Cuba.

E. A. Some claim that we are near to reach the "Theory of everything" in Physics -based on the unification of all forces. The recent (possible) discovery of the Higgs boson seems like an important new piece in the jigsaw. After completing it, our job might be just to understand the details of "non-essential" phenomena -so to speak. Do you think we will actually reach a "Theory of everything"? Should the "leftover phenomena" be regarded as less essential to Physics?

L. K. *In the usual discussions, the "theory of everything" means a theory narrowly aimed at unifying our understanding of gravity and the quantum theory of particles and fields. Such an increased understanding will affect only few small parts of science, especially particle physics and cosmology, and perhaps some additional parts of astronomy. Such a discovery would leave most scientific investigations unaltered in intellectual interest, impact, and value. We do not know if this kind of unification is possible and if it would in any way change our view of the world.*

E. A. One may think that the aim of Physics is to provide quantitative descriptions of natural phenomena -regardless their nature. Under that wide-scoped definition, to what extent Chemistry and Biology are being "engulfed" by Physics these days?

L. K. *I work in an institute that contains both physicists and chemists. They have very different views of the natural world, and aim at very different outcomes. Typically, the chemist is impressed by the richness and variety of nature. His or her work is aimed at discovering differences between the behaviors of different things (usually molecules) and understanding these differences. Physicists emphasize the unity of nature. They (we) typically look for similarities among different things, and try to explain how these similarities arise.*

I see biology as being in an unsettled state. Some Governments and big businesses have heavily supported molecular biology in the hope and expectation that it would have an immense and profitable impact upon human disease. However, the impact has been smaller than expected. Many important processes occur not at a molecular scale, but at a considerably larger scale. Neglected subjects like organism biology and environmental biology have begun to move to the fore. All of these subjects can make occasional use of the kinds of unifying perspectives that can be supplied by the methods of physics. Often they need math knowledge. Very often all of biology needs sophisticated instrumentation and sophisticated understanding of how the instrumentation works. These things can come into biology through the work of physicists. However, biology must come to its own view of nature, distinct from that of physics or chemistry, and beyond that of legislators and drug companies. This is happening slowly.

E. A. As in many human endeavors, attractive labels are used to identify some areas of research as extremely new and "hot" -sometimes the label is well justified, sometimes not so well justified, I'd say. What do you think about the use of "Complexity" as a "trademark" in Science? What about the use of the prefix "nano"…?

L. K. *Words can be traps.*

To say that one works on "complexity" might mean that one is working on the generation of general laws which might apply quite broadly to many complex systems. That can be dangerous because such laws might not exist, or because useful laws might be hard to find. It might be better to say that one works on geothermal turbulence, or the structure of clays, or the walls of biological cells. In each of these areas, there are important discoveries to be made and specific phenomena to be explained.

"Nano" is another trap. There are many interesting things in chemistry, biology, and physics that occur on the scale of nanometers. Very few things are interesting mainly because they occur at nanoscales. A scientist can only go a small way toward justifying his/her work by saying it is "nano". The next step is the important one. Why is it interesting? For illuminating some natural behavior? For constructing some practical device? Why? "Nano" is hardly enough.

E. A. I feel that research in "Complexity" has been liberating for some experimental physicists -like me- due to the fact that, thanks to computers, one can find new Physics in simple, inexpensive experiments. In your opinion, to what extent the field of "Complexity" should be used as a "lifesaver" for experimental Physics in developing countries?

L. K. *Computers are liberating, but they are also dangerous.*

My grandchildren tend to use computers as a replacement for contact with the world. It is particularly important for the Latin world that there be a clear and always-present contact between things that happen in the world and things that are seen in our lab computers. The experimentalist who uses a computer to control and experiment is not too exposed to this danger. The simulator who tries to represent something in nature by a computer program is however very exposed to the danger that he/she might lose contact with the real world of experiment.

E. A. After having participated in a couple of scientific Physics events in Havana during the last two of weeks, what's your impression about Physics in Cuba?

L. K. *I was very impressed by the high quality of physics research in Cuba. There are so many people with good ideas!*

E. A. Cuban physicists tend to publish their finest scientific results in well known, high-impact scientific journals, instead of doing it in the Revista Cubana de Física (RCF) -a natural consequence of the highly competitive nature of science nowadays. What strategy would you suggest to increase the scientific level of the papers published in the RCF?

L. K. *Your scholars would like to be known in the rest of the world. This is natural. Publications in high impact journals are a good way to receiving a bit of recognition from abroad.*

However, recognition from the home country is also a good thing. I would suggest that RCF makes a big fuss about the one or two or five best papers published in a given year.

This fuss might take the form of a few pesos, plus a big certificate, plus a chance to present at a local physical society meeting.

Leo Kadanoff, as president of the selection committee for the Best Poster of March*COM*eeting'12, congratulates A. Hernández for the First Prize, with the poster entitled "A rheological model based on nonlocal relations between shear stress and velocity gradients for complex fluids". The work was made in collaboration with Prof. O. Sotolongo ("Henri Poincarè" Group of Complex Systems, Physics Faculty, University of Havana). In the picture, with a white shirt, organizer J. O. Fossum (Physics Department, Norwegian University of Science and Technology), reads the award act. The scene took place at "Ambos Mundos" hotel, Havana, on March 7, 2012. (Photo: O. Ramos)

Rev. Cub. Fis. **29**, 1E6 (2012) CONTRIBUTIONS

EXOTIC BEHAVIOR OF HEXAGONS IN FARADAY WAVES

COMPORTAMIENTO EXÓTICO DE HEXÁGONOS EN ONDAS DE FARADAY

N. Périnet[a], D. Juric[b] and L. S. Tuckerman[c †]

a) Faculty of Science, University of Ontario Institute of Technology (UOIT), Oshawa, Ontario, Canada, L1H 7K4
b) LIMSI-CNRS (UPR 3251), B.P. 133, 91403 Orsay France
c) PMMH (UMR 7636 CNRS - ESPCI - UPMC - UPD), 10 rue Vauquelin, 75005 Paris France, laurette@pmmh.espci.fr[†]
† corresponding author

Three-dimensional numerical simulations of hexagonal patterns in Faraday waves are presented, including details of the velocity field and interface motion. The pattern does not remain hexagonal, but is succeeded by alternation of patterns we call quasi-hexagons and beaded stripes.

Se realizan simulaciones numéricas tridimensionales de patrones hexagonales en ondas de Faraday, incluyendo detalles del campo de velocidades y del movimiento de la intercara. El patrón no permanece hexagonal, sino que es sustituído por patrones que llamaremos cuasi-hexagonales, alternando con patrones de bandas.

PACS: Symmetry breaking flow instabilities, 47.20.Ky; Flow instabilities interfacial, 47.20.Ma; Pattern formation in fluid dynamics 47.54.-r

In 1831, Faraday [1] observed that when a fluid layer is subjected to periodic vertical oscillation of sufficient amplitude, standing waves appear on its surface. These waves may take the form of regular stripes, squares, or hexagons. The experimental observation of more complicated structures, such as quasi-patterns, superlattices or oscillons in the 1990s, has led to a great deal of experimental and theoretical research. Numerical simulations are more recent: the first numerical simulation of Faraday waves was carried out in 2000 for the 2D case by Chen and Wu [2] and by Périnet *et al.* [3] in 2009 for the 3D case .

We summarize our formulation and the numerical methods used to compute the fluid motion; see [3] for a more detailed description. A single-fluid model is used to define the velocity $\boldsymbol{u}$ and pressure p over the entire domain. The viscosity and density are variable, taking the values ν_1, ρ_1 for the denser fluid on the bottom, ν_2, ρ_2 for the lighter fluid at the top and varying abruptly at the surface. The equations we solve are then

$$\partial_t \boldsymbol{u} + (\boldsymbol{u}\cdot\nabla)\boldsymbol{u} = -\frac{1}{\rho}\nabla p + \nu\Delta\boldsymbol{u} \\ -\left[g + a\sin(2\pi f t)\right]\boldsymbol{e}_z + \int \delta(\boldsymbol{x}-\boldsymbol{x}')\sigma\kappa\boldsymbol{n}dV \qquad (1)$$

subject to the additional constraints of incompressibility $\nabla\cdot\boldsymbol{u}=0$ and boundary conditions which are periodic in the horizontal directions and no-slip at the vertical boundaries. In (1), the additional gravitational term arises from the transformation to the oscillating reference frame of the container. The last term incorporates surface tension, with σ the surface tension, κ the local curvature, $\boldsymbol{n}$ the vector normal to the surface and pointing from the lower to the upper fluid, and $\boldsymbol{x}$ and $\boldsymbol{x}'$ the positions of points in the domain and on the interface.

We represent the velocity and pressure on a staggered MAC mesh [4] which is fixed and uniform. The moving interface, defined by $z = \zeta(x,y,t)$, is computed by a front-tracking [5]/immersed-boundary [6] method on a semi-Lagrangian triangular mesh which is fixed in the horizontal x and y directions and moves along the vertical direction z. The interface is advected and the density and viscosity fields updated. The capillary force is computed locally on the Lagrangian mesh and then incorporated into the Navier-Stokes equations, which are solved by a projection method. The Poisson problem for the pressure is solved via Biconjugate Gradient Stabilized (BiCGStab) iteration preconditioned by the inverse Laplacian.

The horizontal dimensions of the domain are chosen to accommodate a hexagonal pattern. We take $L_x = 2\lambda_c/\sqrt{3}$ and $L_y = 2\lambda_c$, so that large-scale spatial variations are inaccessible. The simulations were run with a spatial resolution of $N_x \times N_y \times N_z = 58\times100\times180$. Each horizontal rectangle is subdivided into 64 triangles to represent the interface. To validate the spatial discretization, we repeated the simulations with a finer resolution of $N_x \times N_y \times N_z = 75\times125\times225$. Although small quantitative changes were seen, the dynamics remained qualitatively unchanged. The time step is limited by the advective step, taking values varying between T/24 000 and T/4000.

The first detailed spatio-temporal experimental measurements of the interface height of Faraday waves were undertaken by Kityk *et al.* [7, 8]. Their optical technique required the two fluid layers to have the same refractive index, which led them to use fluids of similar viscosities and densities: $\rho_1 = 1346\ kg\ m^{-3}$, $\nu_1 = 5.35 \times 10^{-6}\ m^2\ s^{-1}$, $\rho_2 = 949\ kg\ m^{-3}$, $\nu_1 = 2.11 \times 10^{-5}\ m^2\ s^{-1}$ and surface tension $\sigma = 35\ mN\ m^{-1}$. These parameters, especially the density ratio $\rho_2/\rho_1 = 0.7$, differ markedly from most studies of Faraday waves, which use air above either water or silicone oil and so have $\rho_2/\rho_1 \sim 0.001$. At rest, the heavy and light fluids occupy heights of $h_1 = 1.6\ mm$ and $h_2 = 8.4\ mm$, respectively. The imposed vibration has frequency $f = 12\ Hz$ and the Faraday instability leads to subharmonic standing waves, so that $\zeta(x,y,t)$ oscillates with period $T = 2/f = 0.1666\ s$. Floquet analysis [9] for these parameters yields a critical wavelength of $\lambda_c = 2\pi / k_c = 13.2\ mm \gg h_1$, so that the fluid layer is quite shallow.

The critical acceleration obtained by Floquet analysis is $a_c = 25.8\ ms^{-2} = 2.63g$. For $a \gtrsim a_c$, square patterns are observed experimentally and numerically [3, 7, 8]. The simulations described here were carried out at higher acceleration, $a = 38.0\,ms^{-2} = 3.875g = 1.473\,a_c$, starting from zero velocity and an initial randomly perturbed interface. The simulations produced a hexagonal pattern which oscillates subharmonically [3, 7, 8]. Visualizations of representative velocity fields and of the interface throughout an oscillation period are shown in figures 1 and 2. The patterns and their evolution are far from trigonometric in space and in time. The temporal anharmonicity is a consequence of the high viscosity: a high vibration amplitude a is necessary to overcome the damping and so equation (1) is far from homogeneous in time. The spatial anharmonicity is due in part to the fact that the hexagonal pattern succeeds the squares which appear at onset.

After about 10 subharmonic periods, the hexagonal symmetry is broken and the pattern is replaced, first by another pattern we call beaded stripes, and then by alternation between patterns we call quasi-hexagons and nonsymmetric beaded stripes. Figure 3 shows the time evolution of the instantaneous maximum height $\max_{x,y} \zeta(x,y,t)$ and its envelope $\max_{x,y,[t,t+T]} \zeta(x,y,t)$. Surrounding the time-evolution plot are contour plots of the instantaneous interface height at representative times over one subharmonic cycle, i.e. at times $t_i + jT/4$ for $j = 0,\ldots,3$. The maximum height is strongly correlated with the flow pattern. Since the spatial average of the height remains constant, its maximum measures the spatial variation of the interface. Hexagons (t_1) have the highest peaks, followed by quasi-hexagons (t_3, t_5), and then by beaded stripes (t_2, t_4, t_6). The hexagonal patterns are invariant under the usual symmetry operations of rotation by $\pi/3$ and reflection. The beaded striped patterns are instead invariant under the two reflections:

$$\zeta(x,y) = \zeta(x, n\lambda_c - y) \tag{2a}$$

$$\zeta(x,y) = \zeta(m\lambda_c / \sqrt{3} + \tilde{x}_0 - x, y + n\lambda_c) \tag{2b}$$

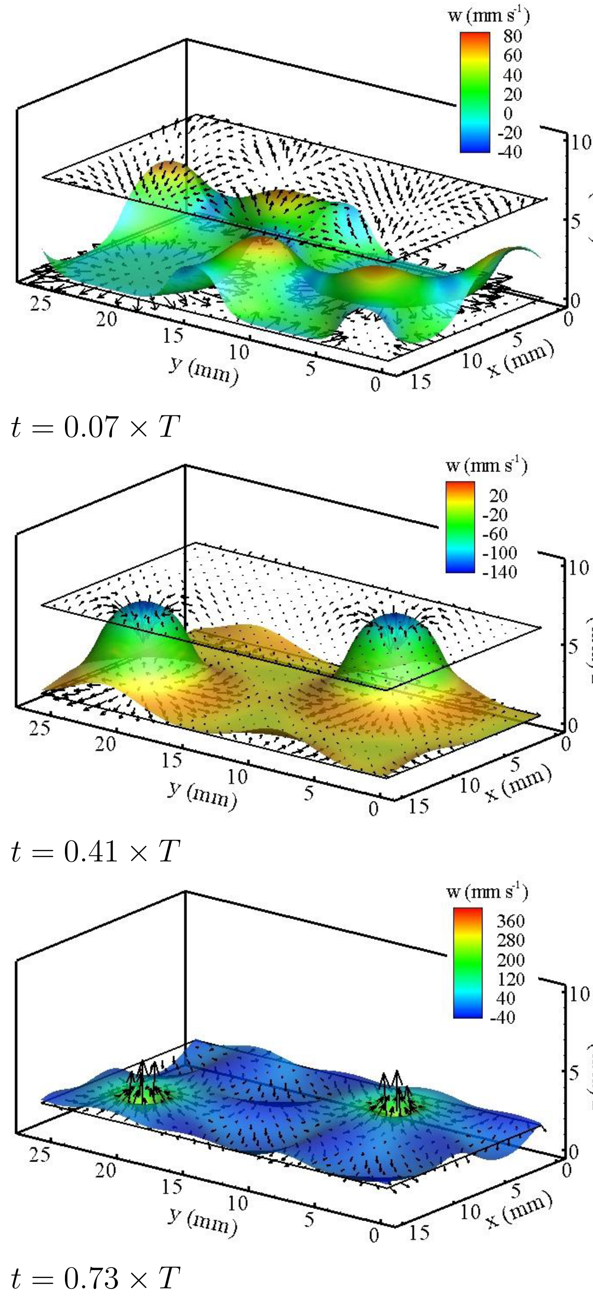

$t = 0.07 \times T$

$t = 0.41 \times T$

$t = 0.73 \times T$

Figure 1: Velocity fields associated with hexagonal patterns.

The quasi-hexagons and nonsymmetric beaded stripes have no exact symmetries but they obey the spatio-temporal symmetry

$$\zeta(x,y,t_{5,6}) = \zeta(m\lambda_c / \sqrt{3} + x_0 - x, y + y_0, t_{3,4} + T/2) \tag{3}$$

That is, the quasi-hexagonal pattern at t_3 is related by a spatial shift-and-reflect operation to that at $t_5 + T/2$ and similarly for the beaded striped patterns at t_4 and t_6. In (2)-(3), $\tilde{x}_0$, x_0 and y_0 are spatial phases whose values depend on details of the initial condition.

The long-time behavior seen in figure 3 could consist of trajectories connecting quasi-hexagonal and beaded striped patterns of each of two phases, i.e. a heteroclinic cycle. An investigation of this hypothesis is currently underway.

[1] M. Faraday, Phil. Trans. R. Soc. Lond. **121**, 299 (1831).
[2] P. Chen and K.-A. Wu, Phys. Rev. Lett. **85**, 3813 (2000).
[3] N. Périnet, D. Juric and L. S. Tuckerman, J. Fluid Mech. **635**, 1 (2009).
[4] F. H. Harlow and J. E. Welch, Phys. Fluids **8**, 2182 (1965).
[5] G. Tryggvason, B. Bunner, A. Esmaeeli, D. Juric, N. Al-Rawahi, W. Tauber, J. Han and Y.-J. Jan, J. Comput. Phys. **169**, 708 (2001).
[6] C. S. Peskin, J. Comput. Phys. **25**, 220 (1977).
[7] A. V. Kityk, J. Embs, V. V. Mekhonoshin and C. Wagner, Phys. Rev. E **72**, 036209 (2005).
[8] A. V. Kityk, J. Embs, V. V. Mekhonoshin and C. Wagner, Phys. Rev. E **79**, 029902 (2009).
[9] K. Kumar and L. S. Tuckerman, J. Fluid. Mech. **279**, 49 (1994).

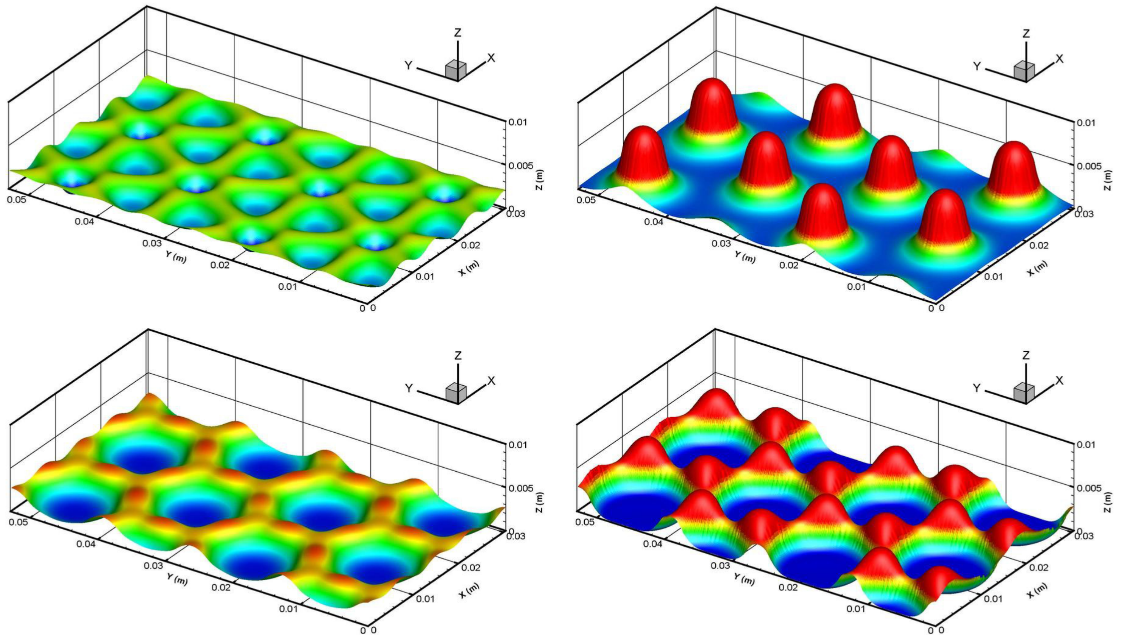

Figure 2: Visualizations of hexagonal interface over one subharmonic oscillation period. The size of the visualization domain is double that of the computational domain in each direction.

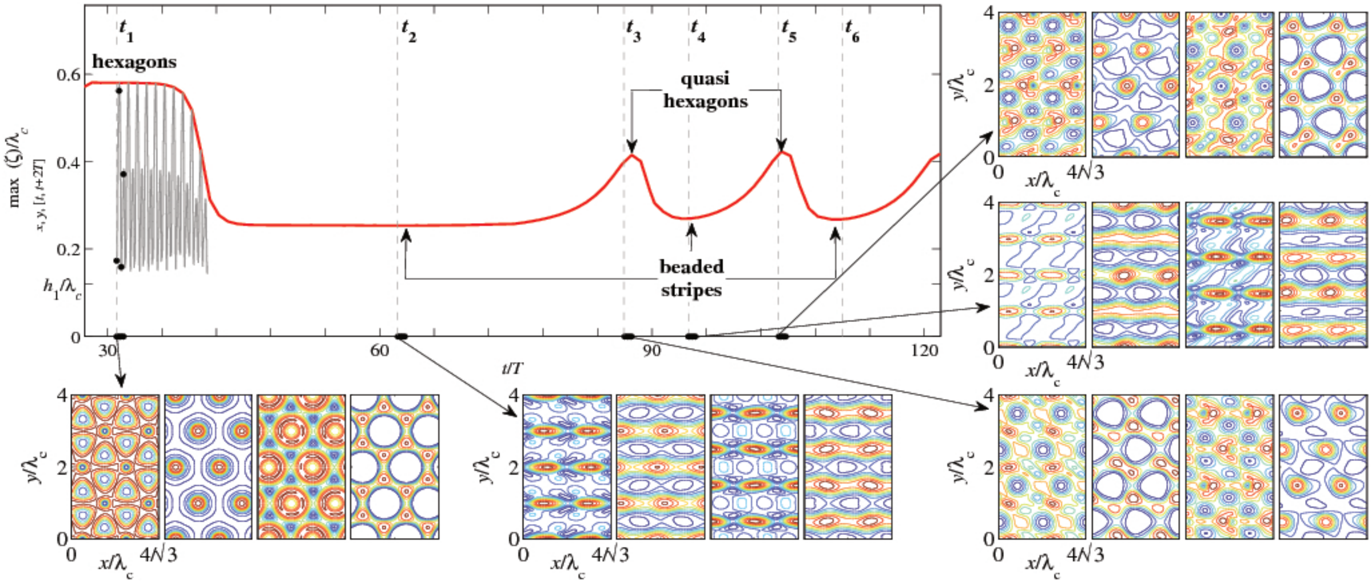

Figure 3: Maximum interface heights $\max_{x,y} \zeta(x,y,t)$ (rapidly oscillating curve) and $\max_{x,y,[t,t+T]} \zeta(x,y,t)$ (smooth curve). Surrounding visualizations show instantaneous contour plots of $\zeta(x,y,t)$. The size of the box has been doubled in each dimension. Visualizations shown at $t_i + j\,T/4$ for $j = 0, 1, 2, 3$, i.e. over one subharmonic period. The hexagonal patterns at time t_1 can be compared with the three-dimensional visualizations shown in figure 3. The pattern consists of beaded stripes at time t_2, quasi-hexagons at t_3 and t_5, and nonsymmetric beaded stripes at t_4 and t_6. Over the large white areas, the interface is very close to the bottom and almost flat. Patterns at t_3 and t_5, and at t_4 and t_6 are related by the spatio-temporal transformation (3).

Rev. Cub. Fis. **29**, 1E9 (2012)

RELAXATION PROCESSES IN COULOMB GLASSES

PROCESOS DE RELAJACIÓN EN VIDRIOS DE COULOMB

J. Bergli[a †] and Y. M. Galperin[a,b,c]

a) Department of Physics, University of Oslo, P.O.Box 1048 Blindern, N-0316 Oslo, Norway, jbergli@fys.uio.no[†]
b) A. F. Ioffe Physico-Technical Institute RAS, 194021 St. Petersburg, Russian Federation
c) Centre for Advanced Study at the Norwegian Academy of Science and L etters, 0271 Oslo, Norway
† corresponding author

Coulomb glasses are materials with electron states localized by the disorder under conditions of long-range interactions between their particles. One realization of a Coulomb glass is a doped semiconductor at low temperatures. Another example is granular metals. Coulomb glasses show complex dynamics typical for other complex systems: sluggish, non-exponential, relaxation of the conductance as well as aging and memory effects similar to those observed in structural glasses. We report dynamical Monte Carlo simulations of relaxation processes in a Coulomb glass. Both the relaxation to equilibrium following an initial temperature quench and during and after a driving by a strong current is studied. We see that out of equilibrium there is an effective electron temperature established on a short timescale, and this relaxes slowly to the bath temperature. We also study the response of the system to an external perturbation and observe how it relaxes after such a perturbation. Both from a random state and after a perturbation from equilibrium we find that the effective temperature relaxes logarithmically.

Los vidrios de Coulomb son materiales con estados electrónicos localizados debido al desorden, cuyas partículas poseen una interacción de Coulomb como, por ejemplo, un semiconductor dopado a baja temperatura, y un metal granular. Los vidrios de Coulomb muestran una dinámica típica de otros sistemas complejas: relajación lenta y no exponencial de la conductividad, y efectos de memoria similar a los observados en vidrios estructurales. En este trabajo, describimos simulaciones de Monte Carlo dinámicas de los procesos de relajación en vidrios de Coulomb. Estudiamos la relajación hacia el equilibrio, después de un enfriado rápido, y durante y después de una perturbación con una corriente eléctrica. Observamos que, fuera del equilibrio, se establece rápidamente una temperatura efectiva del sistema electrónico, y que éste relaja lentamente hacia la temperatura del baño. Estudiamos la respuesta del sistema a una perturbación externa, y la relajación después de la perturbación. Observamos que, en ambos casos, la temperatura efectiva muestra una relajación logarítmica.

PACS: Amorphous semiconductors glasses, 71.23.Cq; Disordered solids, 72.80.Ng; Hopping transport, 72.20.Ee

INTRODUCTION

At low temperatures, disordered systems with localized electrons (*e. g.*, located on dopants of compensated doped semiconductors or formed by Anderson localization in disordered conductors) conduct by phonon-assisted hopping. The theory of this process goes back to around 1970 and is well studied, see Ref. [1] for a review. In recent years, there has been increasing interest in the non-equilibrium dynamics of hopping systems. In particular, the glass-like behavior at low temperatures has been studied both experimentally [2] and theoretically [3]. In this work, we are interested in two features observed in the experiments. Firstly, it was observed that the conductivity relaxes logarithmically as a function of time after an initial quench or perturbation [2]. Secondly, if the system initially in equilibrium is perturbed by some change in external conditions (*e. g.*, temperature or electric field) for a time t_w called the waiting time, the relaxation back towards equilibrium of some quantity like the conductance $G(t,t_w)$ will depend both on t_w and the time t since the end of the perturbation. It is found in certain cases that the relaxation is in fact described by a function $G(t/t_w)$ of the ratio t/t_w. This behavior is called *simple aging* [2].

While simple aging is observed in a range of different systems, we are here particularly concerned with experiments on disordered InO films and porous silicon [2]. The relevant experimental facts can be summarized as follows: (i) After a quench from a high temperature state, the relaxation of conductance is close to logarithmic. (ii) The same is true after driving the system by a strong current. The rate of relaxation depends on the time the system was driven out of equilibrium (waiting time, t_w). When scaled with the waiting time, all curves collapse (simple aging). (iii) If the driving field is too strong, simple aging is no longer observed. (iv) If the waiting time is too long, simple aging is no longer observed.

One question which has been raised is whether the observed glassy behavior is an intrinsic feature of the electron system, or a result of some extrinsic mechanism like ionic rearrangement [4]. In this work, we address the *intrinsic* mechanism by performing dynamical Monte Carlo simulations of the standard lattice model of the electron glass. It is known [3] that during a quench from an initial random state an effective electron temperature,

T_{eff}, is quickly established, and that this temperature slowly relaxes to the bath temperature. We show that the electron temperature relaxes logarithmically over almost three decades in time and that the system demonstrates simple aging behavior in a stress aging protocol (driving by a strong electric current) similar to what is seen in the experiments. While this does not constitute a proof of the intrinsic origin of the glassy behavior, it shows that the model can display the observed behavior.

MODEL

We use the standard tight–binding Coulomb glass Hamiltonian [1],

$$H=\sum_i \epsilon_i n_i+\sum_{i<j}\frac{(n_i-K)(n_j-K)}{r_{ij}}, \qquad (1)$$

K being the compensation ratio. We take e^2/d as our unit of energy where d is the lattice constant which we take as our unit of distance. The number of electrons is chosen to be half the number of sites so that K=1/2. ϵ_i are random site energies chosen uniformly in the interval [-U, U]. In the simulations presented here we used U = 1, which we know gives a well-developed Coulomb gap and the Efros-Shklovskii (ES) law for the conductance [5, 6]. The sites are arranged in two dimensions on a $L \times L$ lattice where in all cases we used L = 1000, which is sufficiently large to give a good estimate of the effective temperature in a single state without any averaging over a set of states. We implement cyclic boundary conditions in both directions.

To simulate the time evolution we used the dynamic Monte Carlo method introduced in Ref. [5], for a more detailed description, see Ref. [7]. In all our simulations we used a phonon temperature T = 0.05, which we know is well into the ES regime for variable range hopping. The graphs show the evolution over 10^8 jumps.

RELAXATION AND EFFECTIVE TEMPERATURE

Let us first relax from an initial random state and measure $T_{eff}(t)$. Shown in Fig. 1 are the energy (inset) and the effective temperature as functions of time. As we can see, the energy graph has almost stopped to decrease, indicating that we have almost reached equilibrium. The same is seen by the effective temperature, where T_{eff} = 0.054, close to the real temperature T = 0.05, in the final state. We see that the effective temperature, after some initial short time, logarithmically decreases in time for about two and a half orders of magnitude. The energy does not show this behavior (as discussed in Ref. [8], it is well fitted by a stretched exponential function). We then applied an electric field E = 0.1 (in units of e^2/d). Shown in Fig. 2 (left) is the energy per site as a function of time. The effective temperature as a function of time is shown in Fig. 2 (left, middle curve). Noting the difference in the timescales we conclude that the energy stabilizes at a new value much faster than the effective temperature.

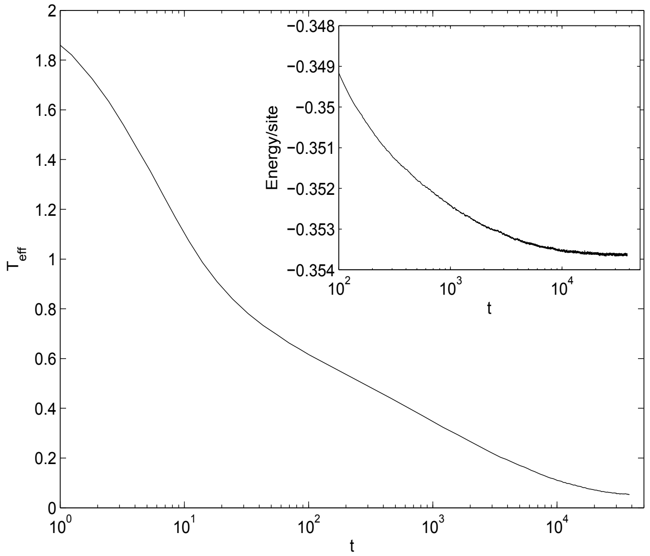

Figure 1: Effective temperature as function of time. The inset shows the energy as function of time.

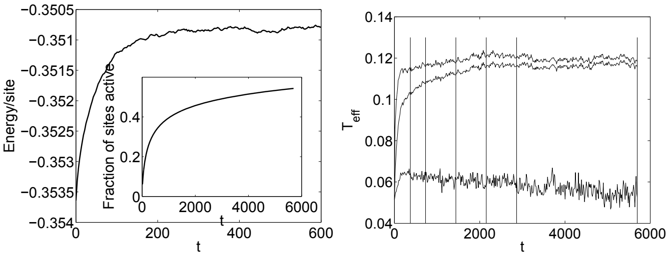

Figure 2: During driving with E = 0.01. Left: Energy as function of time. Inset: The fraction of sites involved in a jump as function of time. Right: Effective temperature as function of time. The curves are from top to bottom the temperature of the sites which were active, the temperature of all sites and the temperature of the sites which were not active. The vertical lines indicate the waiting times in the stress aging protocol (see Fig. 5).

We have also plotted the effective temperature taking into account only those sites which were involved in a jump, Fig. 2 (bottom, upper curve), and those which did not jump, Fig. 2 (bottom, lower curve). As we can see, the sites which are not involved in jumps are still at a temperature close to the phonon temperature. This is not a trivial statement, since the energies of the sites which are not involved in jumps also change due to the modified Coulomb interactions with the sites that jumped. Note that even at the latest time shown, new sites are still being involved, see Fig. 2 (top, inset), even if the energy and effective temperature are more or less stable. When driving with stronger fields we observed some heating also of the sites not involved in any jumps, while the distribution remained close to a Fermi distribution so that the concept of temperature sill has a meaning.

This is shown in Fig. 3. In particular we find it remarkable that also the sites never involved in transitions show a good fit to the Fermi distribution. Normally, we think of energy levels as fixed and occupation numbers changing dynamically in such a way as to maintain the Fermi distribution in the time averaged occupation probabilities. If the energy levels are shifted by

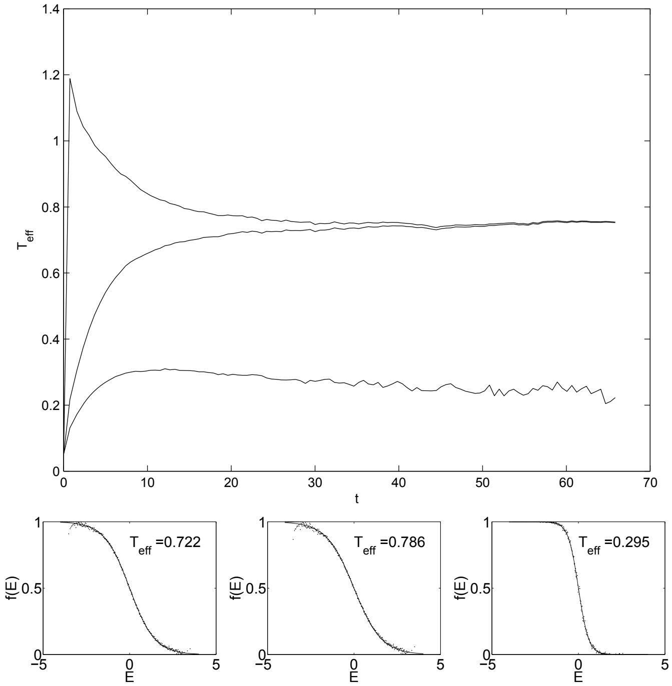

Figure 3: When driving with electric field $E = 1$. Top: T_{eff} as function of time. The curves are from top to bottom the temperature of the sites which were active, the temperature of all sites and the temperature of the sites which were not active. Bottom: Fitted Fermi functions at time $t = 19$. Left: All sites, Center: Sites which took part in a transition, Right: Sites which did not take part in a transition. The points are the data and the curve the fitted function.

some process, the transition rates also have to change, and the occupation numbers will adjust to the new energy level. In our case we have that the occupation numbers of the sites not involved in transitions are fixed, while their energies are pushed around by the interactions with the jumping sites. A natural guess would be that there is no correlation between the energy of a site before the driving starts (and hence the occupation probability of that site) and the shift it receives during driving. One would then guess that the initial Fermi distribution at the real phonon temperature would be scrambled during the driving, and that for the sites not involved in jumps we would not find a well defined Fermi function. The fact that this does not happen indicates that there is certain structure to the nature of the shifts of the energies, and would be an interesting point for further study.

The heating process can also be illustrated in another manner. In Fig. 4 is shown the single particle density of states (DOS) at different times after the start of the driving with $E = 0.1$ (the same as in Fig. 2). Curves for the total DOS as well as for the sites involved and not involved in jumps are shown. The total DOS shows initially a Coulomb gap corresponding to the real phonon temperature. This changes into the more smeared Coulomb gap of T_{eff} on a rather short time-scale. On times longer than this, the curves for jumped and non-jumped sites keep changing as more and more sites are involved in jumps. Thus, the state of the system keeps evolving for times much longer than the one needed for the overall Coulomb gap to adjust to the effective temperature.

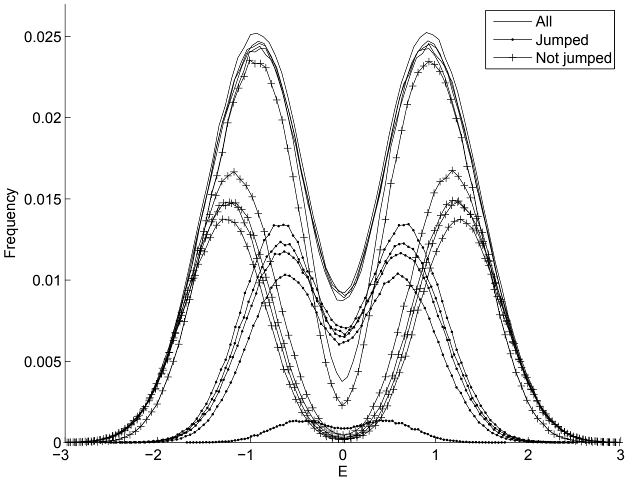

Figure 4: When driving with $E = 0.1$. The density of states at the times $t = 12.5$, 1426, 2851, 4275, and 5696. For the graphs of all sites and jumped sites the lower curves correspond to earlier times and the higher curves to later. For the not jumped sites lower curves correspond to longer times.

STRESS AGING

We now follow the stress aging protocol. This means applying a non-Ohmic field for a certain time t_w and then turning this field off. The heating process of Fig. 2 is exactly such a non-Ohmic driving, and we need only start simulations with zero fields at different points along this curve. We have chosen six t_w, which correspond to the points marked on Fig. 2 with vertical lines.

Figure 5 shows the effective temperature as function of t/t_w after the end of the driving period. Note that the time dependence of the energy is very similar in all cases as shown in Fig. 5 (inset). From Fig. 5 we conclude that there is a logarithmic relaxation of the effective temperature after a driving by a non-Ohmic field just as in the case of relaxation from a random initial state (Fig. 1). Furthermore, we see that the curves for different t_w collapse when time is scaled with t_w when t_w is smaller than some critical value $t_w^{(c)} \approx 2500$. The curve for $t_w = 2865$ seems to lie a little to the left of the collapse curve, and for $t_w = 5696$ this tendency is clear. The collapse of the curves for short t_w is similar to what is observed in the experiments both on indium oxide films and porous silicon [2]. In the case of porous silicon, also the departure from the simple aging at longer waiting times was observed, while sufficiently long times were never reached in the case of indium oxide.

If we compare to Fig. 2 (right) we see that the critical value t_w corresponds to the time where the effective temperature stabilizes. Comparing to Fig. 2 (left) we see that this is a time much longer than the one, which is needed for the energy to stabilize.

We also repeated the stress aging protocol at different driving fields, $E = 0.05$, 0.2, 0.5 and 1. Note that to be in the Ohmic regime we should have $E \lesssim T/10$, so all the fields are well outside of this. For $E = 0.05$ the effective temperature as

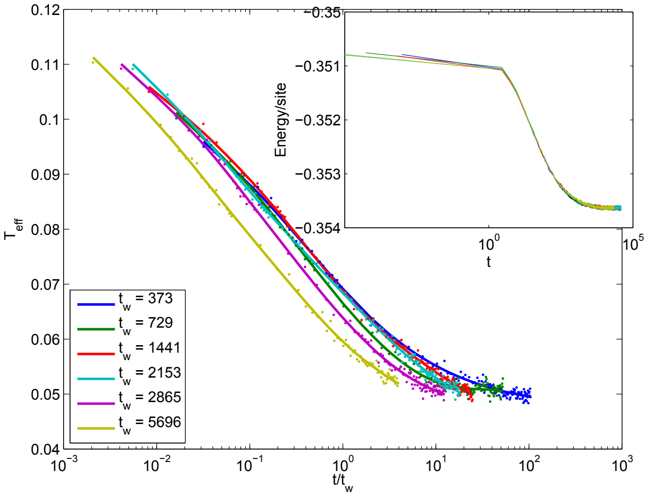

Figure 5: After driving with $E = 0.1$. T_{eff} as function of t/t_w. Inset: Time dependences of the energy for different t_w.

function of t/t_w is shown in Fig. 6 (left). As we see, the general behavior is the same as when driving with $E = 0.1$. For $E = 0.2$ the effective temperature as function of t/t_w is shown in Fig. 6 (right). We see that the curves do not collapse satisfactorily, even for t_w shorter than the time at which T_{eff} stabilizes. This behavior is also observed in the experiments [2], it is characteristic for stronger fields. Further details on these simulations can be found in Ref. [7].

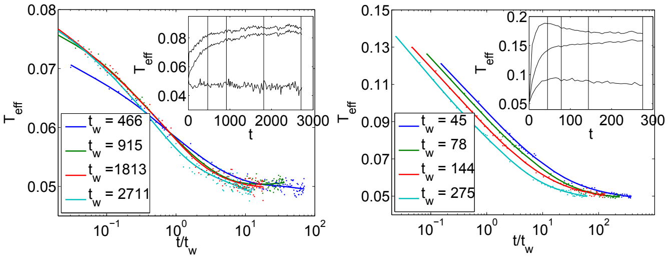

Figure 6: Left: After driving with $E = 0.05$. T_{eff} as function of t/t_w. Inset: The heating curve. Right: After driving with $E = 0.2$. T_{eff} as function of t/t_w. Inset: The heating curve.

CONCLUSIONS

Using the standard lattice model for the Coulomb glass we have demonstrated logarithmic relaxation of the effective temperature after a quench from a random initial state. The same is observed after driving by some non-Ohmic electric field. In the latter case we also observe simple aging when the driving field is not too strong and the waiting time not too long. At longer waiting times or after driving with stronger electric fields we observe departure from the simple aging qualitatively similar to what is seen in experiments. This provides support to the idea that the observed behavior is an intrinsic feature of the electronic system.

The Monte Carlo approach allows us to access several properties, which are not available either in the experiments or the mean field theory. When applying a non-Ohmic field both the average energy and the effective temperature increase and saturate at a level above the equilibrium one. We find that the saturation of energy is much faster than the saturation of effective temperature.

We also see that the heating mainly affects those sites which were involved in jumps. At moderate driving fields the energies of the remaining sites are shifted by the changing Coulomb interactions, but there is no systematic shifts, and the best fitting Fermi distribution is still at or close to the bath temperature. At stronger fields there is also some heating of the sites which were not involved in jumps, and the distribution still follows a Fermi function.

[1] B. I. Shklovskii and A. L. Efros, Electronic properties of doped semiconductors (Springer, Berlin, 1984).
[2] A. Vaknin, Z. Ovadyahu, and M. Pollak, Phys. Rev. Lett. **84**, 3402 (2000); Phys. Rev. B, **65**, 134208 (2002); Z. Ova-dyahu and M. Pollak, Phys. Rev. B **68**, 184204 (2003); V. Orlyanchik and Z. Ovadyahu, Phys. Rev. Lett. **92**, 066801 (2004); S. Bogdanovich and D. Popović, Phys. Rev. Lett. **88**, 236401 (2002); J. Jaroszyński and D. Popović, Phys. Rev. Lett. **96**, 037403 (2006); T. Grenet , J. Delahaye, M. Sabra, and F. Gay, Eur. Phys. J. B **56**, 183 (2007); V. K. Thorsmølle and N. P. Armitage, Phys. Rev. Lett. **105**, 086601 (2010); Ariel Amir, Stefano Borini, Yuval Oreg, and Yoseph Imry, Phys. Rev. Lett. **107**, 186407 (2011).
[3] M. Müller and L. B. Ioffe, Phys. Rev. Lett. **93**, 256403 (2004); Eran Lebanon and Markus Müller, Phys. Rev. B **72**, 174202 (2005); Ariel Amir, Yuval Oreg, and Yoseph Imry, Phys. Rev. Lett. **103**, 126403 (2009); A. M. Somoza, M. Ortuño, M. Caravaca, and M. Pollak Phys. Rev. Lett. **101**, 056601 (2008).
[4] Z. Ovadyahu, Phys. Rev. B **78**, 195120 (2008).
[5] D. N. Tsigankov and A. L. Efros, Phys. Rev. Lett. **88**, 176602 (2002).
[6] A. Glatz, V. M. Vinokur, J. Bergli, M. Kirkengen, and Y. M. Galperin J. Stat. Mech. P06006 (2008); J. Bergli, A. M. Somoza, and M. Ortuño Phys. Rev. B **84**, 174201 (2011).
[7] J. Bergli and Y. M. Galperin, Phys. Rev. B **85**, 214202 (2012).
[8] M. Kirkengen and J. Bergli Phys. Rev. B **79**, 075205 (2009).

INSTABILITY REVEALS CLUSTERING IN COHESIVE GRANULAR MATTER

LA INESTABILIDAD REVELA "CLUSTERING" EN MATERIA GRANULAR COHESIVA

J.-C. Géminard

Laboratoire de Physique de l'Ecole Normale Supérieure de Lyon, CNRS, Université de Lyon, Lyon
jean-christophe.geminard@ens-lyon.fr

We lately reported on a periodic pattern which spontaneously forms at the surface of a thin layer of a cohesive granular material submitted to in-plane stretching [1] or to bending [2]. The mechanism responsible for the instability is the *strain softening* exhibited by humid granular materials above a typical strain. The present short article gives the opportunity to review the potential physical origin of the cohesion in granular materials and, then, to discuss one experimental example which points out the fundamental role played by the clustering in the mechanical response of the cohesive materials.

Recientemente, hemos reportado la formación espontánea de un patrón periódico en la superficie de una lámina fina de material granular cohesivo sometido a estiramiento en el plano [1] o a pandeo [2]. El mecanismo responsable de dicha inestabilidad es el reblandecimiento que exhiben los materiales granulares húmedos por encima de cierta deformación típica. Este artículo corto nos brinda la oportunidad de revisar el posible origen físico de la cohesión en los medios granulares, y de discutir un ejemplo experimental que sugiere el papel fundamental que juega el "clustering" en la respuesta mecánica de los materiales cohesivos.

PACS: Classical mechanics of granular systems, 45.70.-n; pattern formation in granular systems, 45.70.Qj; wetting in liquid-solid interfaces, 68.08.Bc; Adhesion at solid surfaces and interfaces, 68.35.Np

INTRODUCTION

Adding even small minute amounts of liquid can change dramatically the mechanical properties of sand. During the building of sand castles, one observes a transformation from a fluidlike to a sticky and deformable material with increasing water content. Indeed, at very low water content, the formation of partially developed capillary bridges leads to a fast increase of tensile strength whereas, for large enough fluid content, tensile strength is nearly constant [1]. Cluster formation was identified as the main mechanism responsible of such a behavior [2].

POTENTIAL SOURCES OF COHESION

The granular matter is cohesive when attractive forces between the grains are at play. The aim of the present section is to briefly review the potential sources of interaction between the grains.

To begin with a source of cohesion which is one of the most difficult to account for [3], we mention that, due to friction, the grains, if made of a dielectric material, can acquire a static electric charge when flowing. In a dry atmosphere, if the container is not grounded, the electrostatic force can be large enough to lift grains of millimetric size [4]. The charge is difficult to estimate. So are the resulting interaction forces. However, we note that, for solid grains made of a dielectric material, the charge of all the grains has the same sign, which leads to repulsive forces and, thus, not to cohesion [5].

The electroclamping of the particles is a second, but peculiar, source of cohesion which is worth mentioning here [6]. Some authors reported the possibility to induce and, thus, to tune the cohesion of granular materials by applying an external electric field [7].

Finally, even when the grains are electrically neutral, they are subjected to an attractive electrostatic force arising from the polarisability of the material. In order to evaluate the intensity of the associated effect, one can compare the magnitude of the Van der Waals force between two spheres of radius R separated by the minimum distance δ, $F_{VdW} = AR/12\delta^2$, where A is the Hamaker constant [8], with the weight of one grain, $W = 4/3\pi r^3 \rho g$, where g is the acceleration due to the gravity and ρ the density of the material the grains are made of. The force F_{VdW} diverges if the grains are smooth and in contact but, in practice, the distance δ is limited by the roughness of the grain surface. For a typical value of the Hamaker constant of about 10^{-19} to 10^{-21} J and a typical size $\delta \sim 100$ nm associated with the roughness, one estimates that the Van der Waals force is significant for grains having a radius of about a few micrometers or less, thus for fine powders only.

Like electrostatic interactions, magnetic interactions can lead to cohesion. Even if this case is again peculiar, particles having an induced or permanent magnetic moment can attract each other. Experiments [9] and, accordingly, numerical simulations [10] show that, because of long-range interactions, the effects of the magnetic interactions on the angle of repose remains weak even if the forces associated with the bead-bead interactions can be significantly larger than the weight of the beads.

Together with the Van der Waals interaction, the most frequent source of cohesion is the capillary force associated with the liquid bridges that spontaneously form at the contact points between the grains in contact with a humid atmosphere. This latter case will be thoroughly discussed in the next section but, before ending this list of the main potential cohesion sources, we mention that, in some cases, the liquid at the contact points between the grains mediates chemical reactions that result in solding the grains to each other. Such solid bridges form, for instance, for glass beads in contact with a humid atmosphere [11] or immersed in water [12]. Again, the magnitude of the associated cohesion is difficult to estimate because the strength of the solid contacts is largely system dependent. The same conclusion holds true for sticky grains.

The next section focusses on the special case of the cohesion due to the liquid bridges formed at the contact between the grains.

HUMIDITY RELATED COHESION

For grains having a typical size from tens to hundreds of micrometers, the main source of cohesion is the formation of capillary bridges between the grains [13, 14, 15, 16]. In order to approach the phenomenon, one can estimate that, for a bridge at equilibrium between two smooth grains of diameter *d*, the typical value of the force is γd, where γ denotes the surface tension of the liquid-vapor interface [8, 13]. Note that the result is independent of the bridge size and that, in such conditions, the capillary forces would be important for any grains smaller than the capillary length (constructed with the density of the beads material), $\sqrt{\gamma / \rho g}$ which is of the order of 1 *mm*. The conclusion that, independent of the water content, grains smaller than 1 *mm* would naturally remain stuck to each other is obviously contradicted by everyday experience.

In practice, the roughness of the grain surface makes the situation slightly more complicate. Indeed, when the grains are not smooth, depending on the amount of water at a contact between two grains, one can identify three different regimes, namely the *asperity*-, the *roughness*- and the *sphere*-regimes [14]. For grains in contact with a humid, but reasonably dry atmosphere (relative humidity smaller than typically 70%), one must thus consider that two neighbouring grains are connected by a series of small bridges at the scale of the roughness and not by a single bridge.

Another experimental feature is that the water is not homogeneously distributed in the bulk of the granular material [17, 18]. First, due to the heterogeneity of the packing at the grain scale, the nucleation is easier at some contacts. We mention, even if the phenomenon is out of the scope of the present article, that the thermally activated nucleation of the liquid bridges in the material leads to an ageing of its mechanical properties, for instance of the angle of avalanche [12, 19, 20]. Second, even at equilibrium, the geometry of the bridge is entirely imposed by the thermodynamic equilibrium with the vapor and by the boundary conditions. Thus, an increase of the water content mainly leads to an increase in the number of bridges and not to a change in the volume of the existing bridges [21]. Due to the history of the bridges formation, the material consists of an assembly of wet clusters. As a consequence, for instance, the discharge of a wet granular material through an orifice involves the flow of clusters instead of individual particles [22], leading to a larger effective size of the flowing particles [23].

The mechanical properties of the cohesive granular matter are the subject of many experimental and theoretical studies [24, 25, 26, 27]. The authors mainly focussed on the assessment of the tensile stress and shear modulus as a function of the water content. Here, we understand by tensile stress the maximum stress necessary to open a cut plane in the bulk of the granular material. However, it is well-known that the force due to a liquid bridge decreases when the grains are pulled apart [28]. This feature at the contact level leads, at the level of the granular material, to a *stretch-thinning* behavior that leads to the mechanical instability of the material under tensile forces [1] and to the formation of fractures whose origin qualitatively differs from that of the fractures more classically observed in compression [29].

The *stretch-thinning* properties of the cohesive granular matter have been recently studied by H. Alarcón and F. Melo [30, 31]. For the purpose of the present article, let us very briefly summarize the conclusions. First, the tensile stress indeed decreases when the material is stretched. The maximum tensile stress, σ_s, increases when the humidity content, R_H, is increased and the grain size, *d*, decreased. The associated shear modulus is proportional to the tensile stress: $G \propto d\sigma_s$. The decrease of the tensile stress, when two blocks of the cohesive granular are pulled apart, is characterized by a distance $\delta \sim \sigma_s d^2 / \gamma_f$, where γ_f has the dimension, and the order of magnitude, of a surface energy.

We shall see in the next section, that such properties explain the dependence of the typical size associated with the fracturing of a thin, cohesive, granular layer on the layer thickness *h*, grain size *d* and relative humidity R_H.

INSTABILITY AND FRACTURING OF A THIN COHESIVE GRANULAR LAYER

Spreading a thin layer (typically 1 *mm*) of cohesive granular matter (flour, for instance) onto an elastic membrane and then stretching it by pulling two opposite ends reveals a very intriguing and beautiful pattern (Fig. 1). In Ref. [1], we provided an explanation for the well-defined angle the fractures make with the stretching direction and reported the dependence of the wavelength on the experimental parameters.

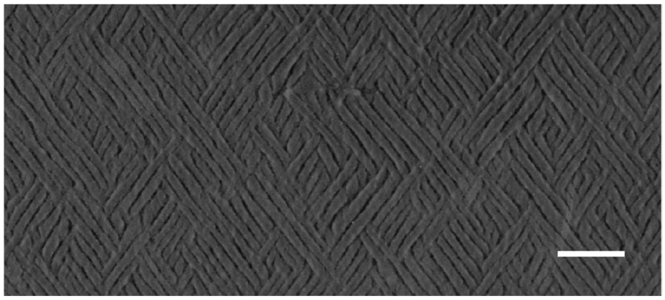

Figure 1: Fracture pattern that spontaneously forms when a cohesive granular layer is stretched on top of an elastic membrane. The layer is stretched along the left-to-right axis and the scale bar is worth $1\ cm$. The granular material consists of spherical glass-beads (USF Matrasur, sodosilicate glass, bead diameter $d = 0$ - $45\ \mu$m). The free surface of the layer (thickness, $h = 1.5\ mm$ is imaged from above by means of a digital camera (Konica-Minolta, A200). Two linear arrays of LEDs, placed at two opposite sides, about $20\ cm$ away from the sample, a few centimeters above the table plane, provide grazing light and, thus, a good contrast when the upper surface of the material is deformed (see [1] for details).

The angle that the fractures make with the stretching direction is independent, for spherical glass beads, of the size d of the particles, of the layer thickness h and of the relative tive humidity, R_H. As a matter of fact, the elongation of the membrane in a given direction produces a contraction in the perpendicular direction. As a result, in the perpendicular direction, the grains are pushed against each other. The tensile stress σ_s is thus involved in the stretching direction whereas the much larger elastic modulus E of the material the grains are made of is involved in the perpendicular direction. The stress is negligible in the stretching direction and one can account for the experimental angle by considering the Mohr criterion for a pure compression in the perpendicular direction [32]. The stripes make the angle $\pm\alpha$ with the stretching direction, with $\alpha = \frac{4}{\pi} + \frac{\Phi}{2}$ and $\tan\Phi = \mu$, the internal friction coefficient.

The typical spacing between the fractures is governed by the *stretch-thinning* properties of the material as proven by results obtained for a pure uniaxial stretching [1] or for a pure bending [2]. Indeed, due to the strain softening, in response to the overall stretch, the system spontaneously tends to modulate the deformation: Regions of large deformation are associated with a smaller modulus and regions of large modulus are associated with a smaller deformation, which results in an overall decrease of the energetic cost. In turn, the modulation induces a shear deformation in the thickness h of the sample, which is associated with an energetic cost. Thus, the wavelength is governed by the balance of the gain associated with the modulation of the horizontal strain and of the loss associated with the induced shear. The main result of the theoretical analysis is that the wavelength is proportional to the layer thickness and that, in the limit of small liquid bridges (small cohesion),

$$\lambda = 4\sqrt{\frac{2}{G}\frac{\partial\sigma}{\partial\theta}}\,h, \tag{1}$$

the slope $\frac{\partial\sigma}{\partial\theta}$ accounting for the decrease of the tensile stress σ when the uniaxial strain θ is increased [1].

In the light of the recent assessment of the mechanical properties of the cohesive granular matter [30, 31], one can understand where the dependence of the wavelength of the grain size and humidity comes from. Indeed, one can write $\frac{\partial\sigma}{\partial\theta} = \frac{\sigma_s}{\theta_m}$ and, then, $\lambda = 4\sqrt{2\sigma_s / G\theta_m}\,h$, where θ_m is the characteristic uniaxial strain associated with the rupture of the material. From the latter relation and from $G \propto d\sigma_s$, one leads to $\lambda \propto h/\sqrt{d\theta_m}$. Denoting nd the typical size of a cluster and considering that the maximum distance over which the grains can be pulled apart before the rupture is governed by the roughness of the surface, one obtains $\theta_m = \delta/nd$ and, then, $\lambda \propto h\sqrt{n/\delta}$, where δ is a length which characterizes the roughness (δ is found independent of the grain size d for our samples). We find that the whole set of experimental data is correctly described taking $n = 1 + \sigma_s d^2 / \gamma^* \delta$. The only adjustable parameter $\gamma^\star$ is found to be of the order of $10^{-3}\ J/m^2$ for glass beads in equilibrium with a humid atmosphere.

The conclusion is that the phenomenon is drastically dependent of the properties of the grain surface, in particular to the roughness, as expected at small relative humidity R_H, in the asperity or capillary regimes [14]. The phenomenon also points out the importance of the heterogeneity of the water concentration in the system. Indeed, the dependence of λ on R_H is only due to the dependence of the cluster size n on the humidity content.

CONCLUSIONS

The present article was the opportunity to briefly review the physical mechanisms at play in the cohesion of the granular matter and to illustrate, in a simple experiment, that the properties at the contact scale and the heterogeneity of the water distribution at the scale of a few grains play a crucial role in the mechanical response of the material subjected to a tensile deformation. The *stretch-thinning* feature of the adhesion force leads to the formation of a pattern whose characteristics have been related with microscopic parameters. Note finally that the mechanical instability should be observed in any material exhibiting a negative sensitivity to the strain increase, might prove to be more general and, thus, deserves further investigation.

ACKNOWLEDGMENTS

The author acknowledges financial support from Contract N° ANR-09-BLAN-0389-01.

[1] H. Alarcón, O. Ramos, L. Vanel, F. Vittoz, F. Melo and J.-C. Géminard, Phys. Rev. Lett. **105**, 208001 (2010).

[2] J.-C. Géminard, L. Champougny, P. Lidon and F. Melo, Phys. Rev. E **85**, 012301 (2012).

[3] E. Mersch, G. Lumay, F. Boschini and N. Vandewalle, Phys. Rev. E **81**, 041309 (2010).

[4] B. Andreotti, Y. Forterre and O. Pouliquen, *Les milieux granulaires: entre fluide et solide*, (EDP Sciences, CNRS Editions, Paris, 2011).

[5] T. Pahtz, H. J. Herrmann and T. Shinbrot, Nat. Phys. **6**, 364 (2010).

[6] P. W. Dietz and J. R. Melcher, Indust. Eng. Chem. Fund. **17**, 28 (1978).

[7] J.-F. Métayer, P. Richard, A. Faisant and R. Delannay, J. Stat. Mech. P08003 (2010).

[8] J. Israelachvili, *Intermolecular and Surface Forces*, 2 Ed (Academic Press, London, 1992).

[9] A. J. Forsyth, S. R. Hutton, M. J. Rhodes, and C. F. Osborne, Phys. Rev. E **63**, 031302 (2001).

[10] K. Taylor, P. J. King, and M. R. Swift, Phys. Rev. E **78**, 031304 (2008).

[11] N. Olivi-Tran, N. Fraysse, P. Girard, M. Ramonda and D. Chatain, Eur. Phys. J. B **25**, 217 (2002).

[12] H. Gayvallet and J.-C. Géminard, Eur. Phys. J. B **30**, 369 (2002).

[13] L. Bocquet, E. Charlaix, F. Restagno, C. R. Physique **3**, 207 (2002).

[14] T. C. Halsey and A. J. Levine, Phys. Rev. Lett. **80**, 3141 (1998).

[15] N. Mitarai and F. Nori, Adv. Phys. **55**, 1 (2006).

[16] F. Soulié, *Cohésion par capillarité et comportement mécanique de milieux granulaires*, Thèse de Doctorat, Université Montpellier 2 (2005).

[17] M. Scheel , R. Seemann , M. Brinkmann , M. Di Michiel, A. Sheppard , B. Breidenbach and S. Herminghaus, Nature **7**, 189 (2008).

[18] M. Scheel , R. Seemann , M. Brinkmann , M. Di Michiel, A. Sheppard and S. Herminghaus, J. Phys.: Condens. Matter **20**, 494236 (2008).

[19] L. Bocquet, E. Charlaix, S. Ciliberto, J. Crassous, Nature (London) **396**, 735 (1998).

[20] N. Fraysse, H. Thomé and L. Petit, Eur. Phys. J. B **11**, 615 (1999).

[21] J.-C. Géminard and H. Gayvallet, Phys. Rev. E **64**, 041301 (2001).

[22] V. Richefeu, *Approche par éléments discrets 3D du comportement de matériaux granulaires cohésifs faiblement contraints*, Thèse de Doctorat, Université Montpellier 2 (2005).

[23] E. Freyssingeas, M.-J. Dalbe and J.-C. Géminard, Phys. Rev. E **83**, 051307 (2011).

[24] T. H. Kim and C. Hwang, Eng. Geol. **69**, 233 (2003).

[25] T. Gröger, U. Tüzün and D. M. Heyes, Powder Tech. **133**, 203 (2003).

[26] F. Radjai and V. Richefeu, Phil. Trans. R. Soc. A **367**, 5123 (2009).

[27] P. C. F. Møller and D. Bonn, Eur. Phys. Lett. **80**, 38002 (2007).

[28] C. D. Willett, M. J. Adams, S. A. Johnson and J. P. K. Seville, Langmuir **16**, 9396 (2000).

[29] J.-Y. Delenne, M. S. El Youssoufi, F. Cherblanc and J.-C. Bénet, Int. J. Numer. Anal. Meth. Geomech. **28**, 1577 (2004).

[30] H. Alarcón, *Comportamiento mecánico de una capa de material granular sometida a deformaciones en el plano*, PhD Thesis, Universidad de Santiago de Chile, Santiago de Chile (2012).

[31] H. Alarcón, J.-C. Géminard and F. Melo, *to be published in* Phys. Rev. E (2012).

[32] R. M. Nedderman, *Static and Kinematics of Granular Materials*, (Cambridge University Press, Cambridge, England, 1992).

Rev. Cub. Fis. **29**, 1E17 (2012)　CONTRIBUTIONS

CLAY ALIGNMENT IN ELECTRIC FIELDS

ALINEACIÓN DE ARCILLAS EN CAMPOS ELÉCTRICOS

R. C. Castberg[a †], Z. Rozynek[b], J. O. Fossum[b,d ‡], K. J. Måløy[a,d *], P. Dommersnes[c,d] and E. G. Flekkøy[a,d]

a) Department of Physics, University of Oslo, P.O. Box 1048, NO-0316, Oslo, Norway,
rene@castberg.org†, k.j.maloy@fys.uio.no*
b) Department of Physics, NTNU, Høgskoleringen 5, NO-7491, Trondheim, jon.fossum@ntnu.no‡
c) Matieres et Systemes Complexes, Universite Paris 7, 75253, Paris, France
d) Centre for Advanced Study at the Norwegian Academy of Science and Letters, Drammensveien 78, NO-0271 Oslo, Norway
†, ‡, * corresponding authors

The response of rotational alignment of lithium fluorohectorite (Li-Fh) to an external electric field has been studied by employing image analysis. Large aggregates consisting of many single clay particles were prepared using a sedimentation technique in order to control both their shapes and sizes. Such aggregates have a layered structure which was confirmed by wide-angle X-ray scattering (WAXS) studies. Measuring the electric-field-induced alignment of these particles we obtained a data collapse by plotting $\ln(\theta)$ versus t/E^2, where θ is the rotational angle, t is time and E is the electric field strength.

Se estudia la respuesta de la alineación rotacional de la fluorohectorita de litio (Li-Fh) debido a un campo eléctrico externo mediante análisis de imágenes. Se prepararon grandes agregados consistentes en muchas partículas individuales de arcilla usando una técnica de sedimentación, con el objetivo de controlar tanto sus formas como sus tamaños. Tales agregados poseen una estructura a capas, lo que fue confirmado por dispersión de rayos X de ángulo ancho (WAXS). Midiendo el alineamiento inducido por campo eléctrico de las partículas, obtuvimos un colapso de los datos en un gráfico $\ln(\theta)$ vs. t/E^2 donde θ es el ángulo de rotación, t es el tiempo, y E es la intensidad del campo eléctrico.

PACS: Electrorheological fluids, 47.65.Gx; self-assembly (nanofabrication), 81.16.Dn; X-ray scattering in structure determination, 61.05.cf

INTRODUCTION

On application of an external electric field, clay particles suspended in non-polar and non-conductive carrier fluids (such as silicone oil) will rotate and align themselves [1] such that their stacking direction is normal to the electric field direction. Once these particles have aligned themselves, they will eventually start forming chain-like structures [2, 3, 4]. In order to understand the processes behind chain formation, we have to understand how the individual particles initially orient themselves with the field. From preliminary observations, we find that for small particles this process takes a couple of *ms*, for this reason we prepared larger particles which were easier to manipulate. In this work optical measurements were made of the particles aligning themselves in the electric field and we show that there is a E^2 dependency on the rotation rate.

SAMPLE PREPARATION

Lithium fluorohectorite (Li-Fh) was purchased from Corning Inc., New York in the form of a white powder. Li-Fh is a synthetic 2:1 smectite clay having the nominal chemical formula $Li^{+}_{1.2}[[Mg_{4.8}Li_{1.2}]Si_8O_{20}F_4]^{1.2-}$ per unit cell, where Li is an interlayer exchangeable cation (not to confuse with Li in the crystaline sheet); for more details on structure see reference [5]. Li-Fh has a surface charge of 1.2 e-/unit cell and is a polydisperse clay with platelet diameters ranging from a few hundred *nm* up to several μm [6]. In order to have a better control on the particle shape and size (parameters that may influence the rotation time when particles are subjected to *E*-fields), it was decided to prepare the samples as follows. The Li-Fh powder was mixed with deionized water and stirred for 12 *h* at RT. Next, the solution was transferred to a flat Petri dish and then left for 3 days at RT for water evaporation. During that time the individual clay particles sediment, and generally lie flat on the bottom of the dish and consequently stack on one another as sketched in Figure 2 (a). In order to obtain different particle thicknesses' four different clay concentrations were used, namely 0.5, 1, 2 and 4 *wt*.%. In this proceeding we will present data from the 2 *wt*.%. Once the samples have dried, they were carefully cut into small pieces with desired lengths and widths (see Figure 1).

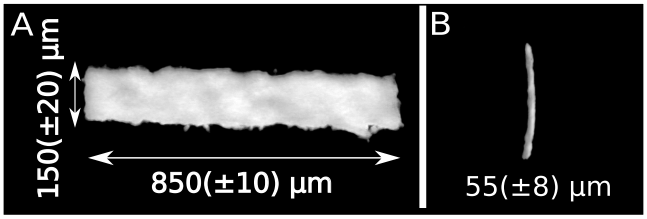

Figure 1: Optical microscopy images of the sample showing length of around 0.85 *mm* (A) and thickness of around 55 μm (B).

SAMPLE CHARACTERISATION

The sample shown in Figure 1, with thickness of around

55 μm, was measured at our home laboratory (NTNU, Norway) using a NanoSTAR X-ray instrument from Bruker AXS, setup in a wide-angle X-ray scattering (WAXS) configuration during the present experiments. This instrument is equipped with a CuKα micro-source emitting X-rays at wavelength of 1.5418 $\AA$; and a 2-D detector that collects Bragg diffraction rings. The equipment enabled the investigation of both the orientational distribution of the clay platelet stacks and the characteristic interlamellar distance for monitoring the intercalated water content. The X-ray beam is directed such that it is normal to the sedimentation direction, as shown in Figure 2 (a), i.e. the thickness of the particle. The beam has a diameter of about 0.4 mm and the available scattering q-range for the setup used here was: 0.08 - 1 $\AA^{-1}$.

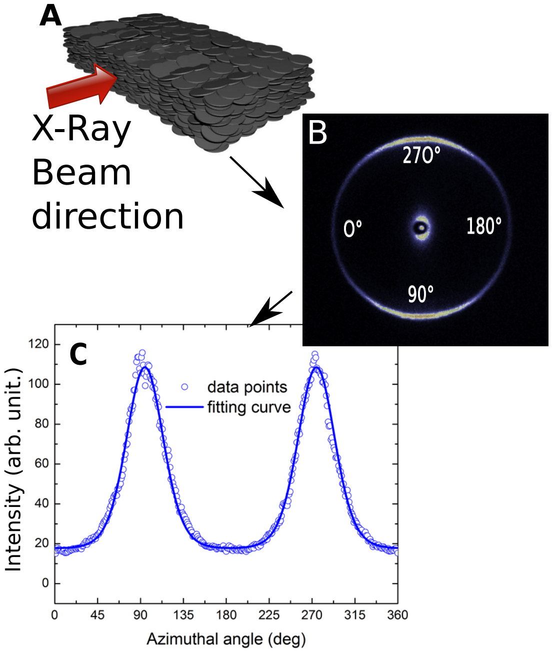

Figure 2: (A) Clay platelets forming an aggregate, (B) resulting in an asymmetry in the WAXS data. (C) The azimuthal plot is made by radial integration of the 2-D WAXS pattern. The parametric fit (solid line) is used to calculated the nematic order parameter (here $S_2 = -0.34 \pm 0.02$).

An example of the two-dimensional WAXS pattern is shown in Figure 2 (b). The 001 Bragg ring that originates from the clay interlamellar distance (between clay crystalline sheets) is anisotropic indicating that the clay particles have a preferential orientation. Since the scattering intensity peaks at 90º and 270º and the direction of the X-ray beam is horizontal, one can conclude that the clay particles are oriented with their stacking direction normal to the X-ray beam, as sketched in Figure 2 (a). When the 2-D WAXS pattern is integrated along the radial direction with a narrow q-range (2θ-angle) around the Bragg ring, one can obtain a 1-D azimuthal plot, as presented in Figure 2(c). This can be fitted to a parametric function (such as Maier-Saupe, see [7, 8]) in order to calculate the nematic order parameter (S_2), which is a qualitative measure of the clay particles' orientation distribution. In this case, the S_2 was found to be -0.34 ± 0.02 (remark: $S_2 = 0$ and $S_2 = -0.5$ indicate no preferential orientation and perfect alignment, respectively).

EXPERIMENTAL SET-UP AND ANALYSIS

The experimental set-up is sketched in Figure 3. Castor oil was used as a hosting liquid to fill the cell. The castor oil has a high viscosity (~ 1000 cSt), ensuring that the particles rotate slowly enough to obtain accurate data. The particle is placed in the centre of the cell such that it is completely surrounded by the castor oil. Initially the particle (prepared as described in the sample preparation section) is aligned with the major axis normal to the electric field, and the narrowest side aligned parallel to the electric field. When the field is then applied the particle starts to rotate such that the major axis is eventually aligned parallel to the field. Each measurement is filmed at 30 fps and then the recording is processed using MATLAB by tracking the particle from frame to frame (using the regionprops function). Its angle is calculated by fitting an ellipse to the particle and measuring the angle of the major axis. For each of the measured field strengths the same particle was used, ensuring that the experiments were as similar as possible.

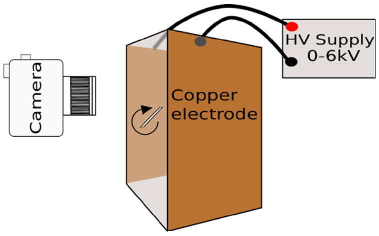

Figure 3: Experimental setup: A video camera is used to film the rotating particle in a glass cell. The two copper electrodes are connected to a high voltage supply capable of supplying up to 5 kV DC. Resulting in an electric field of up to 500 V/mm.

RESULTS AND DISCUSSION

The results for tracking the same particle at different field strengths can be seen in Figure 4. In this plot we see the angle of the particle plotted against the time. It can be clearly seen that the rotation time for the lowest fields (100 V/mm) are considerably longer than for the highest fields (500 V/mm).

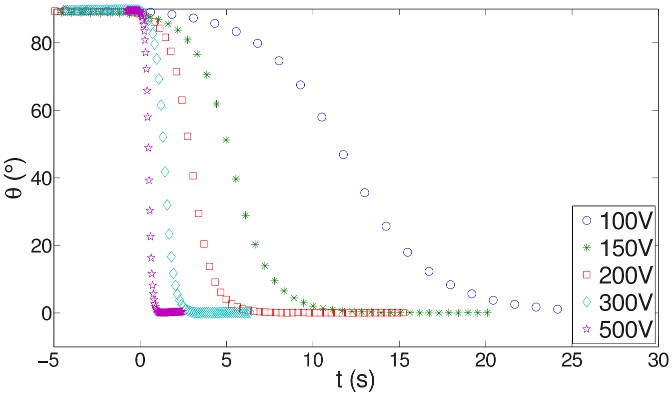

Figure 4: Angle of rotation for a single particle at different electric field strengths. Particle size: $0.85 \times 0.15 \times 0.055$ mm

This is expected as there is an equilibrium between the torque (T) applied from the electric field and the drag of the oil. The torque due to drag in the rotational plane can be written as[9]:

$$T_d = -\zeta_{rot}\dot{\theta}, \tag{1}$$

where ζ_{rot} is the specific rotational drag coefficient in the plane the particle rotates.

The torque due to the electric field is [10,11]

$$\vec{T}_E = (\overline{\chi}\vec{E})\times\vec{E}, \tag{2}$$

which can then be written as

$$T_E = \chi_0 E^2 \sin(\theta)\cos(\theta), \tag{3}$$

where χ_0 is the effective polarizability involving geometric factors. As the data is for the same particle, i.e. the shape and structure are the same, χ_0 is considered a constant.

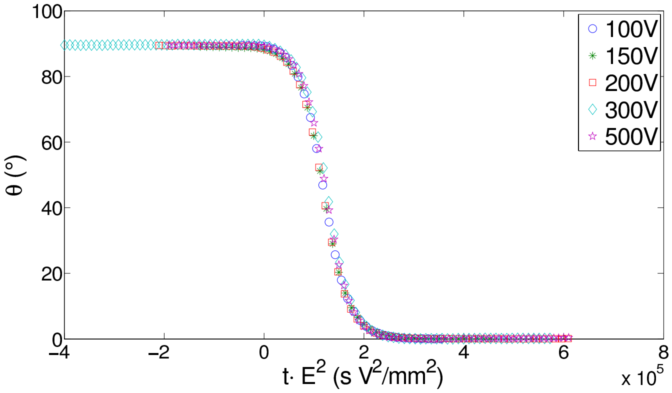

Figure 5: Data collapse of Figure 4, θ plotted against time multiplied by E^2 for different field strengths. Particle size: $0.85 \times 0.15 \times 0.055$ *mm*

We are operating in the low Reynolds number regime ($Re < 0.01$), and can ignore any inertial effects, hence the electric torque balances the hydrodynamic torque giving

$$\dot{\theta} = -\frac{\chi_0 E^2}{2\zeta_{rot}}\sin(2\theta) = -\frac{1}{2\tau}\sin(2\theta) \tag{4}$$

and thus we obtain

$$\tau \propto \frac{1}{E^2} \tag{5}$$

This is confirmed by way of a data collapse by plotting θ against $t \cdot E^2$, where t is the time and E is the field strength. This can be seen in Figure 5. We should note that we have not treated the anisotropic effects of the dipole that would be encountered as the cylinder rotates. For a more detailed study the reader is referred to Doi and Edwards [9] Solving equation Eq. (4) results in

$$\ln\left(\frac{\tan(\theta)}{\tan(\theta_0)}\right) = -\frac{t-t_0}{\tau}, \tag{6}$$

where t_0 is the time the field is applied, and the corresponding angle $\theta_0 = \theta(t_0)$. We can observe this in Figure 6 where we plot $\ln(\tan(\theta))$ against $t \cdot E^2$ and can see an exponential cut-off, with a slope of -3.4 × 10^{-5}.

CONCLUSION

From the data we can clearly see that θ scales with time as E^2 as the electric field strength is changed. In future work we wish to determine the effect of the particle geometry, and how multiple water layers affect the rotation time, as in these experiments we only had 1 water layer, and whether the intercalated cations contribute to the dipole moment.

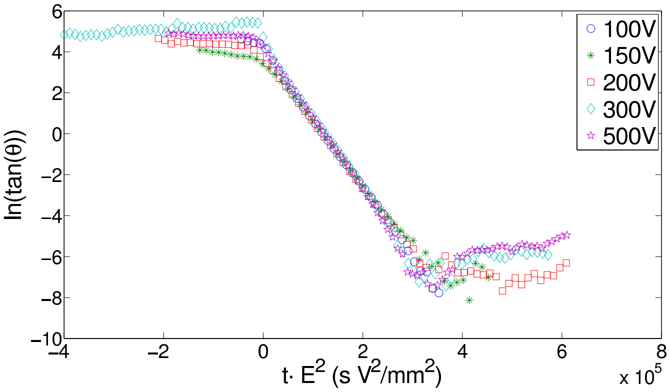

Figure 6: Data collapse of Figure 4, $\ln(\tan(\theta))$ plotted against time multiplied by E^2 for different field strengths. Particle size: $0.85 \times 0.15 \times 0.055$ *mm*

ACKNOWLEDGEMENTS

This work was supported by the Research Council of Norway through the Nanomat program, project number 182075 and the FRINAT program, project number: 171300.

---

[1] J. O. Fossum, Y. Méheust, K. P. S. Parmar, K. D. Knudsen, K. J. Måløy and D. M. Fonseca, Europhys. Lett. **74**, 438 (2006).

[2] B. Wang, M. Zhou, Z. Rozynek and J. O. Fossum, J. Mater. Chem. **19**, 1816 (2009).

[3] Z. Rozynek, K. D. Knudsen, J. O. Fossum, Y. Méheust, B. Wang and M. Zhou, J. Phys: Condens. Mat. **22**, 324104 (2008).

[4] Z. Rozynek, H. Mauroy, R. C. Castberg, K. D. Knudsen and J. O. Fossum, Rev. Cub. Fis. **29**, 1E37 (2012).

[5] H. Hemmen, L. R. Alme, J. O. Fossum and Y. Méheust, Phys. Rev. E **82**, 036315 (2010).

[6] P. D. Kaviratna, T. J. Pinnavaia and P. A. Schroeder, J. Phys. Chem. Solids **57**, 1897 (1996).

[7] Y. Méheust, K. D. Knudsen and J. O. Fossum, J. Appl. Cryst. **39**, 661 (2006).

[8] Z. Rozynek, B. Wang, J. O. Fossum and K. D. Knudsen, Eur. Phys. J. E. **35**, 9 (2012).

[9] M. Doi and S. Edwards, *The Theory of Polymer Dynamics*, (Oxford University Press, USA, 1986).

[10] P. Zijlstra, M. van Stee, N. Verhart, Z. Gu and M. Orrit, Phys. Chem. **14**, 4584 (2012).

[11] H-Y Hsu, N. Sharma, R. S. Ruoff and N. A. Patankar, Nanotechnology **16**, 312 (2005).

Rev. Cub. Fis. **29**, 1E20 (2012)

STRUCTURAL STUDIES OF MIXED NANO-SPHERES AND POLYMERS

ESTUDIOS ESTRUCTURALES EN MEZCLAS DE NANO-ESFERAS Y POLÍMEROS

A. Washington[a], X. Li[a], A. Schofield[c], K. Hong[b], M. R. Fitzsimmons[e] and R. Pynn[a,b,d]

a) Center for the Exploration of Energy and Matter and Indiana University Department of Physics, Bloomington, Indiana, USA
b) Oak Ridge National Laboratory, Oak Ridge, Tennessee, USA
c) School of Physics and Astronomy, University of Edinburgh, Mayfield Road, Edinburgh, Scotland
d) Center for Advanced Studies, Norwegian Academy of Science and Letters, Oslo, Norway
e) Los Alamos National Laboratory, Los Alamos, New Mexico, USA

A newly developed neutron scattering technique known as Spin Echo Small Angle Neutron Scattering (SESANS) allows real-space density correlations to be probed in bulk samples over distances ranging from ~20 *nm* to up to several microns. We have applied this technique to study correlations between polymer-stabilized poly(methyl methacrylate) (PMMA) spheres suspended in either dodecane or decalin. As expected, the data show that for colloid volume factions below about 40%, correlations between PMMA spheres are accurately described by the Percus-Yevick hard-sphere model. When a small amount of polymer is added to the colloidal suspension and when the carrier fluid is a good solvent for the polymer, short-range correlations between PMMA spheres are increased by the presence of the polymer depletant and are in reasonably agreement with calculations using an integral equation model. When higher concentrations of polymers are added, we find that long-range, power-law correlations develop between spheres, even though the sample flows freely. When the solvent is not a good solvent for the polymer depletant, correlations between PMMA spheres are unaffected by the addition of small quantities of polymer.

Una nueva técnica de dispersión de neutrones conocida como espín-eco de dispersión de neutrones de bajo ángulo (SESANS, según sus siglas en inglés) permite medir correlaciones de densidad en el espacio real, para muestras masivas, sobre distancias que van desde unos 20 *nm*, hasta algunas micras. Hemos aplicado esta técnica al estudio de las correlaciones entre esferas poliméricas estabilizadas de polimetil-metacrilato (PMMA) suspendidas en dodecano o decalina. Como se espera, los datos muestran que, para fracciones volumétricas inferiores al ~40%, las correlaciones entre las esferas de PMMA se describen bien por el modelo de Percus-Yevick de esferas-rígidas. Cuando se adiciona una pequeña cantidad de polímero a la suspensión coloidal, y cuando el fluido portador es un buen solvente para el polímero, se incrementan por la presencia del depletante de polímero, y muestran un acuerdo razonable con cálculos según un modelo basado en una ecuación integral. Cuando se usan concentraciones mayores de polímero, encontramos correlaciones de largo alcance entre esferas, del tipo ley de potencia, aún cuando la muestra fluye libremente. Cuando el solvente no disuelve bien el depletante de polímero, las correlaciones entre esferas no se afectan si se agregan pequeñas cantidades de polímero.

PACS: Neutron scattering in structure determination, 61.05.fg; polymer solutions flow properties, 47.57.Ng; structure of polymer solutions , 61.25.he; correlations collective effects, 71.45.Gm

INTRODUCTION

When sterically-stabilized colloidal spheres of poly(methyl methacrylate) (PMMA) are suspended in a hydrocarbon solvent, small angle neutron scattering (SANS) from the mixture can be described using the Percus-Yevick model for hard-sphere correlations [1]. In the present work, our goal was to probe the changes induced in the correlations between the colloidal spheres when an attractive force between them is turned on. To generate this force, we have added small amounts of polymer to generate a depletion interaction between the spheres [7]. Rather than measure the correlations using traditional SANS, we have chosen to use a new technique called spin-echo SANS or SESANS.

SESANS AND SANS

SANS is a widely used method for interrogating the structure of materials on length scales between a few nanometers and roughly 100 *nm*. SANS measurements of a colloidal fluid are described as a product of a form factor –the Fourier transform of the density distribution within each colloidal particle– multiplied by a structure factor which contains information about inter-particle correlations. Unfortunately, much of the latter information is found at large values of the neutron's wavevector transfer, *Q*, where the scattering is strongly damped by the form factor. This makes traditional SANS a good tool for measuring form factors, i.e. the structure of non-interacting monodisperse particles, but a rather poor one for measuring inter-particle correlations in colloids.

SESANS overcomes some of the disadvantages of SANS by Fourier transforming the neutron scattering signal and providing a correlation function in real space [2]. It is more sensitive to inter-particle correlations than traditional SANS because it exactly Fourier transforms the scattering signal –including the weak signal at large *Q* which contains information about correlations– before noise is added by the measurement. In addition to this advantage, SESANS measures the same pair correlation function even when a sample scatters strongly whereas SANS patterns obtained with concentrated, strongly scattering dispersions have to be corrected for multiple scattering of neutrons. Finally, the length scale probed by SESANS is larger than for SANS, which makes it a good tool for exploring correlation functions in colloidal fluids containing particles of a few hundred nanometers in diameter.

The correlation function, *G(z)*, measured by SESANS is a projection of the usual Debye density-autocorrelation function on to a particular direction, *z*. For isotropic fluids such as those studied here the choice of direction onto which the Debye function is projected is irrelevant. Mathematically, *G(z)* is given by the Abel transform of the Debye correlation function [5].

SESANS works by encoding the scattering angle of each neutron into the Larmor precession phase accumulated as the neutron passes through suitably designed magnetic fields [6]. In a SESANS experiment, the cosine of the total Larmor phase is averaged over the scattered neutron beam and measured as a neutron polarization. Because of the cosine factor, the neutron polarization represents a Fourier transform of the scattered neutron intensity.

We have constructed a SESANS apparatus that can be installed on neutron scattering instruments that provide a polarized neutron beam and the measurements described here have been obtained with this equipment mounted on the Asterix reflectometer at the Los Alamos Neutron Science Center (LANSCE). An account of the SESANS technique, which includes a description of the apparatus used in the measurements described here, is given in reference [6].

RESULTS

The colloidal samples we have used in our experiments were prepared using a published method [3]. The resulting PMMA particles, which had diameters between 200 *nm* and 250 *nm* depending on the sample batch, were suspended in either dodecane or decalin at concentrations between 30% and 50% by volume. In order to adjust the neutron scattering contrast between the PMMA spheres and the carrier fluid, mixtures of deuterated and hydrogenated solvents were used. Decalin is both a reasonable solvent for the polymer depletant used in our experiments (polystyrene) and has an optical refractive index which is close to that of PMMA, ensuring that the van der Waals interactions between the PMMA spheres is minimized. Dodecane, on the other hand, is a relatively poor solvent for polystyrene. For PMMA concentrations up to at least 40% by volume, SESANS shows that the correlations between PMMA particles in freshly sonicated samples are well described by the Percus-Yevick, hard-sphere theory for both dodecane and decalin solvents, as shown in Figures 1 (a) and 1 (b).

When small concentrations of polymer depletant are added, the short-range correlations between particles are increased when they are suspended in decalin. A calculation using integral-equation theory [4] shows that the data in Figure 1 (a) can be described using a short-range, attractive potential that is roughly $2kT$ deep. The magnitude of this potential appears to be approximately the same for polymer molecular weights of 110 *kDa* and 900 *kDa* when the same weight percentage of polymer depletant is used. When the particles are dispersed in dodecane, the addition of polystyrene does not change the inter-particle correlations, at least for polystyrene concentrations up to 1% by weight (cf. Figure 1 (b)). This is probably due to the fact that the PS moelcules tend to collapse in the poor solvent, significantly reducing the depeletion forces.

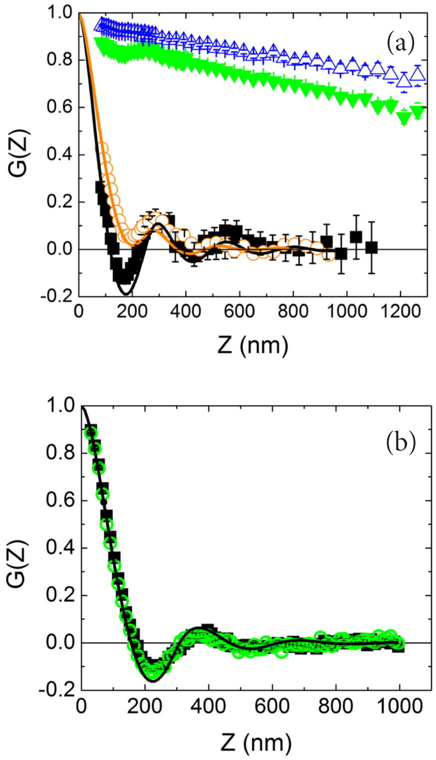

Figure 1: (a) The inter-particle correlation function *G(z)* for 40% suspensions of 260-*nm*-diameter PMMA spheres in decalin measured by SESANS. Solid squares –PMMA spheres alone; open circles– PMMA with 0.2% 900 *kDa* polystyrene; open triangles PMMA with 1% 900 *kDa* polystyrene; inverted triangles PMMA with 0.5% 900 *kDa* polystyrene. Dark line is Percus-Yevick calculation and the lighter line is result of integral equation calculation with "sticky" spheres. (b) *G(z)* for a 40% suspension of PMMA spheres in dodecane (solid squares) and with 1% 110 *kDa* polystyrene (open circles). The line is calculated from the Percus-Yevick theory.

For larger concentrations of depletant in the decalin system (greater than roughly 0.3% by weight for polymers with molecular weights of either 110 *kDa* or 900 *kDa*), SESANS indicates that correlations extend out to distances of many particle diameters and that the correlation function *G(z)* is roughly a linear function over much of the range of inter-particle distances probed (cf. Figure 1 (a)). The correlations eventually disappear at sufficiently large values of z, indicating the maximum size of the aggregates that have been formed. The linear behavior of $G(z)$ is consistent with a power-law behavior of the Debye correlation function. Although the maximum aggregate size often increases with time over periods of several hours, aggregates can be broken up easily by stirring and sonication. The short-range correlations in aggregates appear to be independent of aggregate size but are slightly different from those obtained with weak sticky potentials that do not result in aggregates. This presumably results from jamming of particles once aggregates are formed.

ACKNOWLEDGEMENTS

This work was funded by the U.S. Department of Energy through its Office of Basic Energy Sciences, Division of Material Science and Engineering (Grant No. DE-FG02-09ER46279). The Los Alamos Neutron Science Center is funded by the U.S. Department of Energy's Office of Basic Energy Sciences under contract DE-AC52-06NA25396 with Los Alamos National Security LLC.

---

[1] A. Moussaid, W. C. K. Poon, P. N. Pusey and M. F. Soliva, Phys. Rev. Lett. **82**, 225 (1999).
[2] R. Pynn, M. R. Fitzsimmons, H. Fritzsche, M. Gierlings, J. Major and A. Jason, Rev. Sci. Instrum. **76**, 053902 (2005).
[3] L Antl, J. W. Goodwin, R. D. Hill, R. H. Ottewill, S. M. Owens, S. Papworth, and J. A. Waters, Colloids And Surfaces **17**, 67 (1986).
[4] X. Li, C. -Y. Shew, Y. Liu, R. Pynn, E. Liu, K. W. Herwig, G. S. Smith, J. L. Robertson and W. -R. Chen J. Chem. Phys. **132**, 174509 (2010).
[5] R. Andersson, L. F. Van Heijkamp, I. M. De Schepper and W. G. Bouwman., J. Appl. Cryst. **41**, 868 (2008).
[6] R. Pynn, R. Ashkar, P. Stonaha, A. L. Washington, Physica B **406**, 2350 (2011).
[7] W. C. K. Poon, J. Phys: Condensed Matter **14**, R859 (2002).

THE SHIFTING SHAPES OF FRICTIONAL FLUIDS

LAS FORMAS CAMBIANTES DE LOS FLUIDOS CON FRICCIÓN

B. Sandnes[a †], E. G. Flekkøy[b], K. J. Måløy[b] and J. A. Eriksen[b]

a) Multidisciplinary Nanotechnology Centre, College of Engineering, Swansea University, Singleton Park, Swansea SA2 8PP, UK, b.sandnes@swqansea.ac.uk†
b) Department of Physics, University of Oslo, Sem Sælandsvei 24, PO Box 1048 Blindern, 0316 Oslo, Norway
† corresponding author

Remarkable shapes and patterns appear in multiphase flow experiments with frictional fluids. Here we explore the rich dynamics, and map the emerging morphologies in a phase diagram.

Se observan interesantes formas y patrones en experimentos multifásicos sobre fluídos con fricción. Aquí, exploramos esa rica dinámica, y "mapeamos" las morfologías emergentes en un diagrama de fases.

PACS: Pattern formation in granular systems, 45.70.Qj; multiphase flows, 47.55.-t; compaction granular solids, 45.70.Cc; general flow instabilities, 47.20.-k.

INTRODUCTION

While displacement patterning in dry granular materials [1,2] and density matched granular suspensions [3-5] have been studied before, the world of settling granular mixtures, where inter-particle friction plays a dominant role, remains largely unexplored. Here we focus on pattern formation in such a frictional fluid, and find a surprising diversity in the morphologies that emerge. Based on our experimental and theoretical results [6-8] we draft a crude phase diagram of the different pattern formation modes we encounter and the phase boundaries between them.

EXPERIMENT

The experiment is simple: Air contained in a syringe is injected into a generic granular-liquid mixture confined in a 500 μm gap between two parallel glass plates of a Hele-Shaw cell (Fig. 1). The syringe pump is driven at a constant compression rate q, and the volume of compressible air in the syringe, V_{air}, adds an adjustable compliance (or stiffness) to the system. The initial filling fraction of granular material –glass beads of 100 μm average diameter– is denoted φ, where we normalize by the close-packing fraction, i.e. $\varphi = 1$ for consolidated grains. The invading air/fluid interface displaces the mixture, and the shifting balance between the contending forces (pressure, frictional, viscous and capillary forces) determines the dynamics as we explore the full range of the chosen experimental variables. In the following we give a somewhat brief description of the most characteristic morphologies that we observe, and refer to a recent paper [8] for more detail regarding experimental setup, results and theoretical considerations.

FRICTIONAL REGIME

Frictional fingers. At low compression rate ($0.01 < q < 0.1$ *ml/min*) the invading interface moves slowly and bulldozes up granular material until a layer forms that jams in the gap of the cell. The interface becomes unstable, and fingers of air develop that spawn side-branches as they grow, creating a random labyrinthine structure [6,7]. Fig. 2 (a) shows an example of these frictional fingers, where the dense granular front is seen as a dark band along the interface.

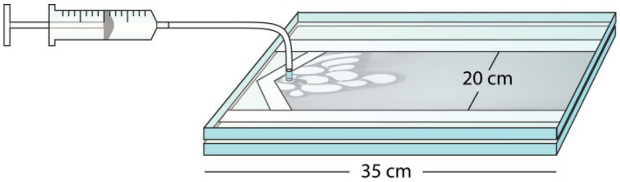

Figure 1: Air is injected into a granular-liquid mixture confined in the gap of a Hele-Shaw cell.

The gas pressure is balanced by the surface tension of the interface and the opposing frictional stress. These forces act locally, and the fingers develop a characteristic width that is independent of system size (unlike viscous fingers). Surface tension acts to widen the curved finger tip, while friction opposes wide fingers since they accumulate thick granular fronts. The characteristic width represents a balance between these two opposing influences. If we increase the amount of granular material in the system, the increased friction shifts the balance, resulting in narrower fingers.

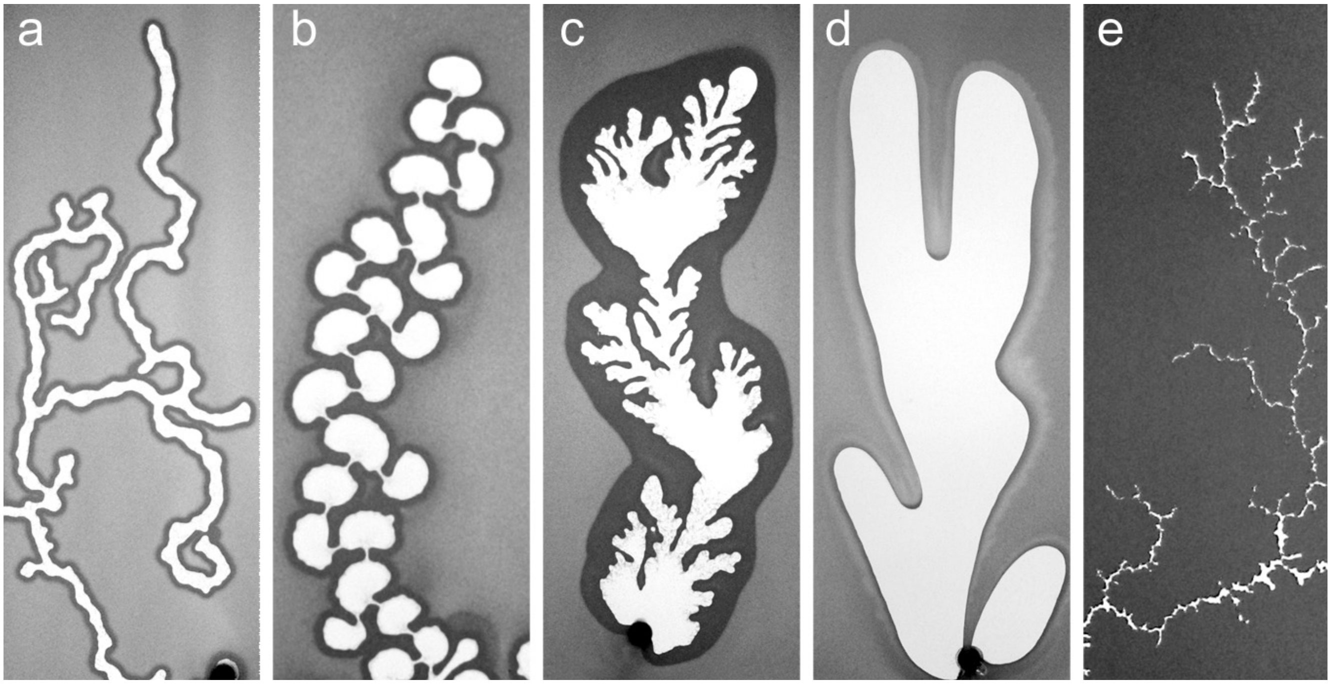

Figure 2: Shapes of air in frictional fluids. (a) frictional fingers (low rate, low packing fraction, high stiffness), (b) stick slip bubbles (low rate, intermediate solid fraction, low stiffness), (c) fluidized front "corals" (intermediate rate), (d) viscous fingers (high injection rate) and (e) fractures (high packing fraction).

Stick slip bubbles. Fig. 2 (b) shows a string of bubbles that have appeared in a stick slip fashion, one by one, at approximately 10 minutes intervals. The pump rate is the same as for the frictional fingers, but by either increasing the packing fraction or by increasing the compliance of the system (or both), the dynamics changes abruptly to this new dynamic mode. Each bubble scoops up a thick granular front, and breaking through this front requires a high gas pressure. In the stationary period, the constant driving of the pump compresses the gas and the pressure slowly builds until the jammed granular front finally yields. The interface yields at its weakest point, from which a narrow channel breaks through the jammed packing. The compressed gas expands, and a bubble inflates in the granular-liquid mixture.

VISCOUS REGIME

Fluidized front (corals). At flow rates greater than roughly 0.1 *ml*/*min*, the motion of the front is fast enough that fluid forces inside the packing overcome friction and prevent jamming of the front. The active front is continuously fluidized by the moving interface, and we are in a domain where viscous forces dominate the dynamics. Fig. 2 (c) shows a peculiar looking "coral" structure that grows at intermediate flow rates. The pattern develops in a two-stage process: first a bubble expands. Then narrow fingers start to invade the fluidized front surrounding the bubble. The less viscous gas penetrates the (more viscous) fluidized mixture driven by the pressure gradient across the front in a process of local viscous fingering. When one finger gets ahead of the rest, it accelerates, evolving into another bubble.

Viscous fingers. Cranking up the pump rate above 10 *ml*/*min* results in another transition in the system: As Fig. 2 (d) shows, there is no longer a dark front of accumulated granular material surrounding the interface. The granular material is re-suspended by the flow, and we are now effectively dealing with a granular suspension. The Saffman-Taylor instability [9] in granular suspensions has been studied by other authors [3,4], and like Chevalier *et al.* [3], we find an early destabilization and branching of the viscous fingers due to the noise associated with the granularity of the suspension (Fig. 2 (d)).

SOLID REGIME

Fractures. What happens when we increase the packing fraction considerably? At $\varphi \sim 0.9$ the granular material fills the gap in the cell, but is not fully compacted into a close packed configuration. The material is a solid, yet deformable (porous) medium. Fig. 2 (e) shows that injection of gas into this system results in fractures. The fractures are several particle diameters wide, and the morphology is fractal of appearance. The fractures grow intermittently, in a stick slip fashion similar to the bubbles in Fig. 2 (b).

Porous media. If the packing fraction is increased further, the system ultimately reaches the close packing limit ($\varphi = 1$), and is effectively a consolidated porous medium. The displacement of fluid occurs in the pore space network defined by the rigid granular matrix. Local fluctuations in the threshold capillary pressures of pores, in addition to the viscous pressure gradient in the cell, determine the displacement dynamics [9-12]. There are two main pattern formation modes: Capillary fingering at low rates, where viscous forces are negligible and pores are invaded in sequence depending on their threshold capillary pressure, and viscous fingering at high rates, where the displacement dynamics is governed by the pressure field in the cell. Capillary fingering progresses from pore to pore in random directions, forming compact structures in an invasion percolation process. Viscous fingers in porous media on the other hand follow the pressure gradient in the cell generated by the displacement of the fluid. They grow in thin branching fingers towards the edge of the cell in fractal structures that look similar to those obtained in diffusion limited aggregation (DLA) processes.

PHASE DIAGRAM

Summarizing the results, Fig. 3 shows a qualitative phase diagram of the morphologies as a function of compression rate (q) and the inverse of the packing fraction (φ^{-1}), i.e. from high to low packing fraction. Both axes are log-scale, and the phase borders are intended as "guides to the eye" only.

The medium changes character from porous medium to deformable solid to frictional fluid as the packing fraction decreases. Each of these regimes have characteristic morphologies associated with them, and at low rate these are capillary fingering (porous media), fractures (deformable media) and frictional bubbles and fingers (frictional fluids) respectively.

The fluid dynamics of granular mixtures changes character from frictional to viscous flows (fluidized front, viscous fingering) as the rate is increased, and the two-phase flow in porous media undergoes a transition from capillary to viscous fingering for increasing rate. The fracture mode seems reasonably rate-independent within the limited parameter range studied here.

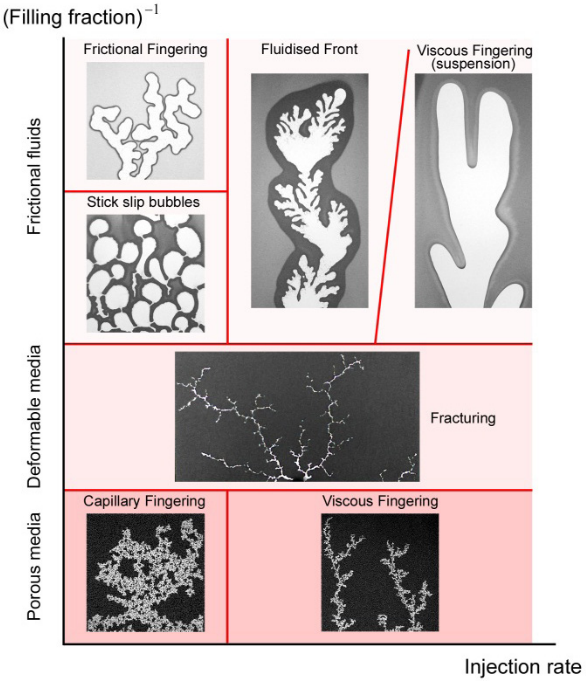

Figure 3: Phase diagram of pattern formation modes obtained by varying the packing fraction and compression rate over several orders of magnitude.

HYDROPHOBIC GRAINS

So far we have considered displacement of a granular fluid mixture by a gas. While the pattern formation is to a large degree governed by the specifics of the system, it is interesting to speculate whether the mechanisms are of a more general nature. Figure 4 shows the result of an "inverted" experiment: A layer of dry hydrophobic grains (0.1 – 0.4 *mm* diameter) is confined in a Hele-Shaw cell (gap ~ 0.6 *mm*). As water is slowly injected into the cell, the dry hydrophobic material is pushed aside by invading water fingers (seen in black in the figure). The resulting patterns and the dynamics are similar to the frictional fingering process depicted in Figure 2 (a) as it is controlled by the capillary forces at the interface, and the frictional interactions in the granular material. The specific nature of these interactions are however expected to be different (dry vs. lubricated grains, incompressibility of the invading phase etc.), and will be investigated in future work.

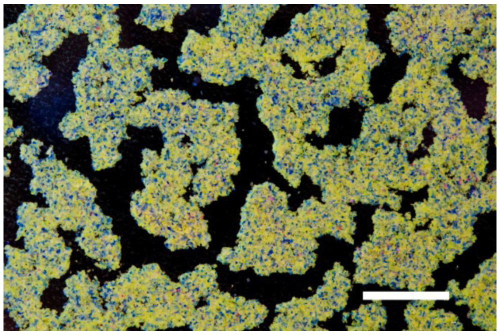

Figure 4: Fingers of water (black) penetrating dry hydrophobic granular material. Scale bar: 1 *cm*.

CONCLUSIONS

We find that the fluid dynamics of granular mixtures is highly complex indeed. Interactions between pressure, frictional, viscous and capillary forces conspire to produce an ever changing landscape of shapes and patterns as the experimental conditions change. Here we have presented characteristic morphologies that emerge as a result of displacement by a gas, and we have outlined the physical mechanisms at play. By mapping the displacement dynamics onto a phase diagram, we provide a means of predicting the type of dynamics occurring for a given set of conditions.

ACKNOWLEDGEMENTS

Dedicated to Henning A. Knudsen and Howard See.

---

[1] X. Cheng, L. Xu, A. Patterson, H. M. Jaeger and S. R. Nagel, Nat. Phys. **4**, 234 (2008).
[2] Ø. Johnsen, R. Toussaint, K. J. Måløy and E. G. Flekkøy, Phys. Rev. E **74**, 011301 (2006).
[3] C. Chevalier, A. Lindner and E. Clement, Phys. Rev. Lett. **99**, 174501 (2007).

[4] C. Chevalier, A. Lindner, M. Leroux, and E. J. Clement, Non-Newton. Fluid Mech. **158**, 63 (2009).
[5] Ø. Johnsen, C. Chevalier, A. Lindner, R. Toussaint, E. Clément, K. J. Måløy, E. G. Flekkøy and J. Schmittbuhl. Phys. Rev. E **78**, 051302 (2008).
[6] B. Sandnes, H. A. Knudsen, K. J. Måløy and E. G. Flekkøy, Phys. Rev. Lett. **99**, 038001 (2007).
[7] H. A. Knudsen, B. Sandnes, E. G. Flekkøy, and K. J. Måløy, Phys. Rev. E **77**, 021301 (2008).
[8] B. Sandnes, E. G. Flekkøy, H. A. Knudsen, K. J. Måløy and H. See, Nat. Commun. **2**, 288 (2011).
[9] P. G. Saffman and G. Taylor, Proc. R. Soc. London, Ser. A **245**, 312 (1958).
[10] K. J. Måløy, J. Feder and T. Jøssang, Phys. Rev. Lett. **55**, 2688 (1985).
[11] G. Løvoll, Y. Meheust, R. Toussaint, J. Schmittbuhl and K. J. Måløy, Phys. Rev. E **70**, 026301 (2004).
[12] R. Lenormand, Physica A **140**, 114 (1986).

PIPE FLOW AS AN EXCITABLE MEDIUM

EL FLUJO DE TOBERA COMO MEDIO EXCITABLE

D. Barkley

Mathematics Institute, University of Warwick, Coventry CV4 7AL, UK, D.Barkley@warwick.ac.uk

The dynamics of turbulent patches (puffs) in pipe flow are related to the dynamics of action of potentials in nerve cells.

Se relaciona la dinámica de los “parches turbulentos” (“puffs”) en el flujo por tubos, con la dinámica de los potenciales de acción en células nerviosas.

PACS: Flow transition to turbulence, 47.27.Cn; action potential propagation in nervous system axons, 87.19.lb,pipe flow, 47.60.-i;

INTRODUCTION

This work explores the connection between the transition to turbulence in pipe flow and the dynamics of excitable media, as exemplified by nerve cells. The primary goal is to leverage years of extensive analysis of excitable media to understand the dynamics of pipe flow. There are several active areas of research in pipe flow that can be analyzed in this context [1, 2].

Figure 1 conveys the essential message and serves to motivate this work. Two very different physical systems are shown. The first is pipe flow, Fig. 1 (a). Fluid moves through a straight pipe with a circular cross section. The pipe is considered to be sufficiently long that end effects are not important. In the quiescent, or unexcited state, flow through the pipe is laminar and individual fluid parcels move in straight lines parallel to the pipe axis. The second system is the axon of a nerve cell, Fig. 1 (b). Here in the quiescent state, or resting state, the cell membrane is polarized with the inside of the cell at a lower voltage potential than the outside. In both systems the quiescent state is stable to small, sub-threshold perturbations and hence the systems remain in the quiescent state indefinitely unless perturbed sufficiently.

Consider now the response of these systems to large, super-threshold, perturbations. For pipe flow, Fig. 1 (c), a typical perturbation might be the injection of a small jet of fluid in the upstream region of the pipe [3]. Assuming the non-dimensional flow rate is in the relevant range, a localized patch of turbulence can be created which moves down the pipe at approximately constant speed. Such a patch of turbulence is called a puff. A typical experimental measurement of a puff would be the fluid pressure near the pipe wall for example. A key point is that the strength and spatial extent of the puff are essentially constant as the puff moves down stream and these features are determined by the nonlinear dynamics of the flow and not by the initial perturbation.

Likewise, a resting nerve axon can be stimulated by the injection of current, Fig. 1 (d). The response is a pulse of depolarization, known as an action potential, which travels down the axon. The standard measurement is the membrane potential, i.e. the voltage difference between the inside and outside of the cell. As with the puff, the shape and speed of the action potential are dictated by properties of the medium and not the stimulus initiating it.

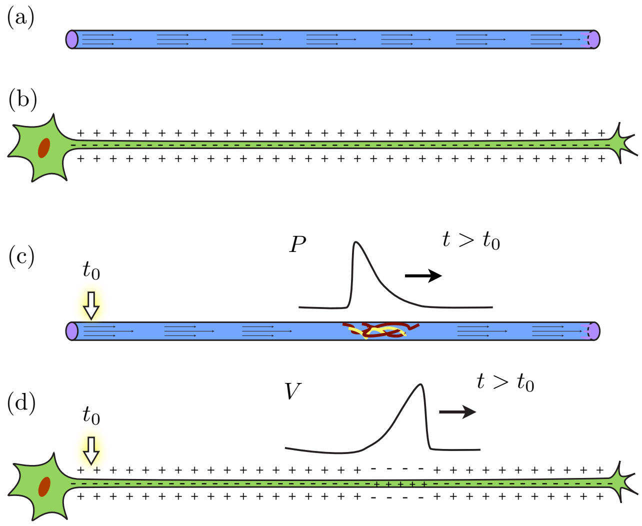

Figure 1: Cartoon illustrating the analogy between pipe flow and a nerve axon. In the absence of stimulation, both systems remain in the quiescent state: (a) flow through the pipe is laminar and (b) the axon is negatively polarized. Following an appropriate stimulation at some time t_0, a localized patch of turbulence moves down the pipe (c) and an action potential propagates down the axon (d).

While Fig. 1 is only a cartoon, the shape of the pressure and voltage signals shown are representative of those of real systems [3, 4]. The two signals share the same features apart from the fact that they are approximately the mirror images of one another. This is not an coincidence, but rather a manifestation of the fact that pipe flow is an excitable medium, similar in many respects to a nerve axon.

EXCITABLE MEDIA

We begin by reviewing concepts from excitable media. For the moment ignore the spatial aspects and just consider local excitable dynamics. Excitable systems are characterized as follows. (See Fig. 2.) They have a linearly stable fixed point, known as the rest state, such that small, sub-threshold perturbations of the rest state return to it without large excursion. Excitable systems additionally possess a nonlinear threshold such that super-threshold perturbations are highly amplified into what is called the excited state. The system does not remain in the excited state indefinitely, but moves into a refractory (or recovering) state and then eventually to the rest state. In the refractory phase, the system is further from the threshold than when in the rest state and hence is it more difficult to excite the system from the refractory state than from the rest state. In some cases it is impossible to excite the system directly from the refractory state. Generally the timescale associated with the nonlinear amplification into the excited state is very much faster than the time scale associated with relaxation to the rest state. The timescale associated with recovery varies considerably from system to system. (See [5, 6] for background on excitable systems.)

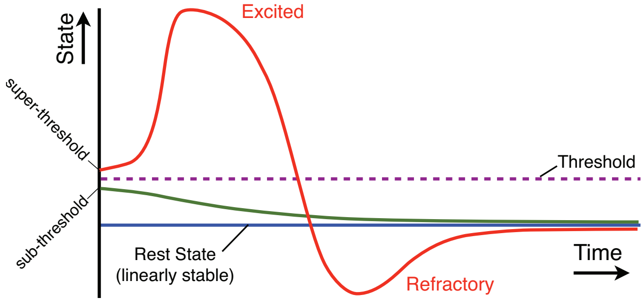

Figure 2: Schematic diagram illustrating excitability. The states of a characteristic excitable system are shown as a function of time. The rest state (blue) is a fixed point. Sub-threshold perturbations (green) of the rest state return directly to it. Super-threshold perturbations (red) are amplified into the excited state. They then go through a refractory phase before returning to the rest state.

Nerve cells are the classic example of an excitable system. The electrophysiological basis of excitability was uncovered by Hodgkin and Huxley in their groundbreaking study of squid giant axons [4]. The details are not important here, and rather than focus on the full mechanism, we consider the simplified FitzHugh-Nagumo model [7]. This model captures the essence of excitability in many physiological system and yet in amenable to straightforward analysis. In its most basic form the model is given by the following equations

$$\dot{V} = V - \frac{V^3}{3} - W + I, \tag{1}$$

$$\dot{W} = a(V + bW + c). \tag{2}$$

The variable V corresponds to membrane voltage while the variable W captures the collective effect of slow recovery of ion channels in the cell membrane. V is called the excitation variable and W the recover variable. I represents the magnitude of a stimulus current. a, b, and c are parameters with typical values $a = 0.08$, $b = -0.8$, $c = 0.7$.

Figure 3 shows a phase portrait for the FitzHugh-Nagumo model together with illustrative trajectories. The dynamics in phase space is organized by the system nullclines: the curve on which $\dot{V}$ and $\dot{W}$ are zero. The V-nullcline is cubic and the middle branch is responsible for the nonlinear threshold for excitation. W provides linear negative feedback and importantly is responsible for the slow recovery. Trajectories and corresponding time series are shown for sub-threshold and super-threshold perturbations. Thus, while the model does not contain many physiological details, it does capture the essence of excitability and provides a clear geometric picture of it.

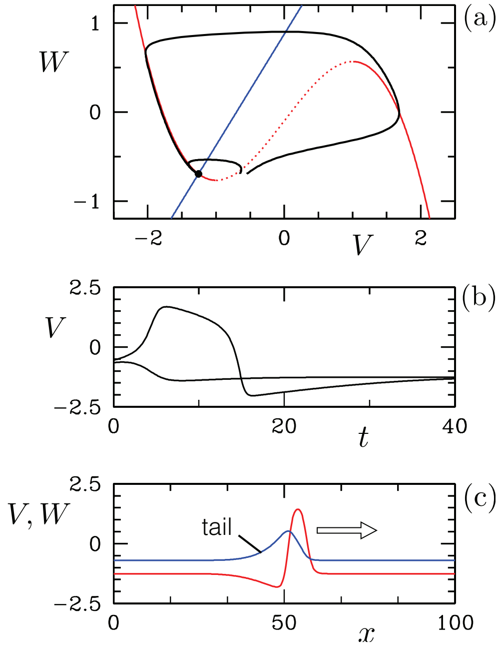

Figure 3: Dynamics of the FitzHugh-Nagumo equations. (a) Phase portrait showing the V-nullcline (red) and W-nullcline (blue) together with trajectories starting from two initial conditions. Both trajectories eventually approach the stable fixed point where the nullclines intersect. (b) Time series for the two trajectories shown in (a). (c) Action potential in the model with spatial coupling (excitable medium). Both the V (red) and W (blue) variables are plotted. A solitary pulse propagates to the right with fixed shape and constant speed. There is a refractory tail behind the pulse.

We return now to spatial aspects and excitable media. For modeling the propagation of action potentials along a nerve axon, the spatial dimension of the axon is taken into account and the FitzHugh-Nagumo model becomes

$$\partial_t V = V - \frac{V^3}{3} - W + I + \partial_{xx} V, \tag{3}$$

$$\partial_t W = a(V + bW + c), \tag{4}$$

where x represents distance along the axon. Figure 3 (c) shows a propagating action potential in the model. Once initiated, an excitation is able to sustain itself through propagation: the pulse excites adjacent medium (to the right in the figure) from the rest state to the excited state, while at the back side of the pulse, the is medium becomes un-excited, going through the refractory phase before returning to the rest state. Within the refractory tail behind the pulse it is not possible to re-excite the system.

PIPE DYNAMICS

Consider now the behavior of puffs in transitional pipe flow. Figure 4 shows a puff from direct numerical simulation of the Navier-Stokes equations [1, 8]. The flow is from left to right. A localized patch of turbulence travels down the pipe (rightward) at approximately fixed speed, maintaining approximately constant size. The two variables plotted reveal the strong similarity between puffs and the action potentials just considered: turbulent fluctuations play the role of the excitation variable while the mean flow, or mean shear, plays the role of the recovery variable.

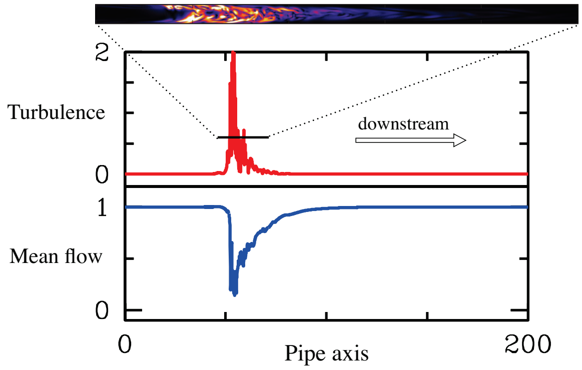

Figure 4: Puff in a direct numerical simulation of transitional pipe flow in a pipe 200 diameters long at Reynolds number 2000. The turbulent fluctuations and mean flow are sampled along the pipe axis at one instant in time. Specifically, the red curve shows the magnitude of transverse fluid velocity (scaled up by a factor of 6) while the blue curve shows the centerline velocity, relative to the mean velocity. A visualization shows the turbulent kinetic energy within the portion of the pipe containing the puff.

To better understand the connection between puffs and action potentials, consider the following model for transitional pipe flow [1]

$$(\partial_t + U\partial_x)q = q\left(u + r - 1 - (r+\delta)(q-1)^2\right) + \partial_{xx}q,$$

$$(\partial_t + U\partial_x)u = \epsilon_1(1-u) - \epsilon_2 uq - \partial_x u,$$

where q represents the turbulent fluctuations and u represents the mean shear. The parameter r plays the role of Reynolds number and U accounts for downstream advection by the mean velocity.

The core of the model is seen in the q-u phase plane in Fig. 5 (a). The trajectories are again organized by the nullclines. The nullclines intersect in a stable, but excitable, fixed point corresponding to laminar parabolic flow. This is the rest state. The u dynamics with $\epsilon_2 > \epsilon_1$ captures in the simplest way the behavior of the mean shear. In the absence of turbulence ($q = 0$), u relaxes to $u = 1$ at rate ϵ_1, while in response to turbulence ($q > 0$), u decreases at a faster rate dominated by ϵ_2. Values $\epsilon_1 = 0.04$ and $\epsilon_2 = 0.2$ give reasonable agreement with pipe flow. The q-nullcline consists of $q = 0$ (turbulence is not spontaneously generated from laminar flow) together with a parabolic curve whose nose varies with r, while maintaining a fixed intersection with $q = 0$ at $u = 1 + \delta$, ($\delta = 0.1$ is used here). The upper branch is attractive, while the lower branch is repelling and sets the nonlinear stability threshold for laminar flow. If the rest state is perturbed beyond the threshold (which decreases with r like r^{-1}), q is nonlinearly amplified and u decreases in response. The similarity to the nullclines for the FitzHugh-Nagumo system are evident.

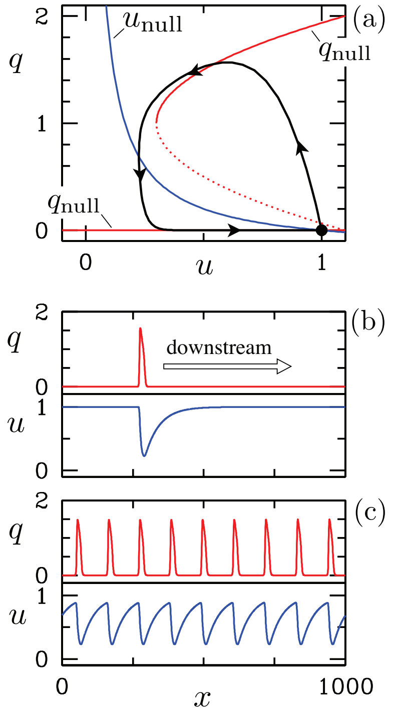

Figure 5: Puffs in the model system. (a) Phase planes shows nullclines for $r = 0.7$. The fixed point (1,0) corresponds to parabolic flow. (b) Solution snapshot at $r = 0.7$. This solution is plotted in the phase planes with arrows indicating increasing x. (c) Sequence of puffs at approximately the maximum density supported by the system.

Figure 5 (b) shows a puff in the model and should be compared both with the puff in Fig. 4 and with the FitzHugh-Nagumo action potential seen in Fig. 3. Two important properties of puffs can now be readily understood. The first concerns the shape of the puff in relationship to that of the action potential. While both structures are moving to the right, they do so for different reasons. As already stated, the action potential travels to the right by exciting the medium to its right. The refractory tail is to the left. By contrast, for the turbulent puff, the excitation from the rest state to the excited state occurs on the left side of the puff and the refractory tail is on the right side. (While not stated in these terms, the physics of this has well understood since at least 1973 [9].) The reason the puff moves to the right is due to the overall downstream motion of fluid within the pipe. This is captured by the parameter U in the model. In the absence of this downstream advection, puffs move to the left (at least for most Reynolds numbers). If experiments were routinely performed in a frame of reference in which the mean flow were zero, the shape of the puff and the direction of propagation would be related exactly as they are for action potentials in physiological media.

The other feature that is evident from this analysis concerns the separation of adjacent puffs. It has been shown in pipe flow that the degree of recovery downstream of a puff dictates how susceptible the flow is to re-excitation into turbulence [10]. This effect is due to the refractory tails on the downstream side of puffs –the slow recovery of u in the model. If one attempts to excite a second puff closely behind a first puff, either the second puff will fail to excite, or if it does, it will either combine with the first puff or move away from it until a characteristic separation is established. Figure 5 (c) shows a number of puffs in the model. The density is at, or nearly at, the maximum supported by the medium.

CONCLUSIONS

In this short paper I have presented ideas connecting the dynamics of transitional pipe flow to the behavior of action potentials in excitable media. I have argued that these systems are closely related and that this relationship is helpful in understanding the dynamics of pipe flow. The analysis can be extended to include more realistic behavior for turbulence, since after all, turbulence is not a single scalar quantity. Extending to other shear flows is difficult, but work as be begun along these lines and appears promising [2].

---

[1] D. Barkley, Phys. Rev. E **84**, 016309 (2011).
[2] D. Barkley, J. Phys: Conf. Seri. **318**, 032001 (2011).
[3] K. Avila, D. Moxey, A. de Lozar, M. Avila, D. Barkley and B. Hof, Science **333**, 192 (2011).
[4] A. Hodgkin and A. Huxley, J. Physiol-London **117**, 500 (1952).
[5] J. Tyson and J. Keener, Physica D **32**, 327 (1988).
[6] J. Keener and J. Sneyd, *Mathematical Physiology*, 2nd Ed. (Springer, New York, 2008).
[7] E. M. Izhikevich and R. FitzHugh, Scholarpedia **1**, 1349 (2006).
[8] D. Moxey and D. Barkley, Proc. Nat. Acad. Sci. **107**, 8091 (2010).
[9] I. Wygnanski and H. Champagne, J. Fluid. Mech. **59**, 281 (1973).
[10] B. Hof, A. de Lozar, M. Avila, X. Tu and T. M. Schneider, Science **327**, 1491 (2010).

Rev. Cub. Fis. **29**, 1E31 (2012) CONTRIBUTIONS

SOLIDIFICATION OF A CORNSTARCH AND WATER SUSPENSION

SOLIDIFICACIÓN DE UNA SUSPENSIÓN DE MAICENA Y AGUA

S. R. Waitukaitis† and H. M. Jaeger

The James Franck Institute and The Department of Physics, The University of Chicago, USA, swaitukaitis@uchicago.edu†
† corresponding author

We report on an investigation of the solidification of a cornstarch and water suspension during normal impact on its surface. We find that a finite time after impact, the suspension displays characteristics reminiscent of a solid, including localized stress transmission, the development of a yield stress, and some elastic energy storage. The time dependence of these characteristics depends on the thickness of the cornstarch layer, showing that the solidification is a dynamic process driven by the impacting object. These findings confirm previous speculations that rapidly applied normal stress transforms the normally fluid-like suspension into a temporarily jammed solid and draw a clear distinction between the effects of normal stress and shear stress in dense suspensions.

Se presenta una investigación de la solidificación de una suspensión de maicena y agua durante el impacto normal en su superficie. Se encuentra que, un tiempo finito después del impacto, la suspensión presenta características de un sólido, incluyendo la transmisión local de estrés, el desarrollo de un límite de elasticidad, y el almacenamiento de engreía elástica. La dependencia del tiempo de estas características depende del espesor de la capa de maicena, mostrando que la solidificación es un proceso dinámico impulsado por el objeto impactante. Estos resultados confirman anteriores especulaciones sobre la rápida aplicación del estrés normal que transforma la suspensión del estado fluido a un estado atascado temporalmente y establecen una distinción clara entre los efectos de la aplicación del estrés normal y el estrés tangencial en suspensiones densas.

PACS: Shock waves in fluid dynamics, 47.40.Nm; suspensions complex fluids, 47.57.E-; liquid-solid transitions, 64.70.D-

INTRODUCTION

Shear-thickening suspensions, such as a mixture of cornstarch and water, are typically studied in rheometry experiments where shear or tensile stress is measured as a function of the shear rate [1, 2, 3, 4]. The results of these experiments are typically categorized as either reversible or discontinuous. In the former, the change in the suspension's apparent viscosity is small and is generally attributed to the formation of "hydroclusters", small groups of particles interacting through lubrication forces [1, 2, 5, 6]. In the latter, the change in viscosity can appear divergent. This behavior is often associated with forcing the particulate phase across the jamming threshold [3, 4, 7, 8, 9], similar to the creation of "shear-jammed" states in dry granular systems [10]. While these experiments are relevant to the investigation of steady-state shear phenomena, they cannot be expected to apply to large-scale, transient disturbances such as the response during rapidly applied normal stress on the suspension surface. Recent experiments [14, 15] with driven, immersed spheres have shown that applied normal stress can lead to jammed regions of suspension transmitting stress to system boundaries. Even so, these measurements have not given the details of how such jammed regions form. We study this solidification process by investigating the stress transmission through a suspension of cornstarch and water during surface impact. Our results show that the growth of the jammed region is directly linked to the dynamics of the disturbance.

RESULTS AND DISCUSSION

The experimental apparatus is shown in Fig. 1. An aluminum rod ($D = 1.86\ cm$, $M = 0.368\ kg$) is allowed to fall-freely or is shot via slingshot into a large tub ($30 \times 30 \times 30\ cm$) of cornstarch and water suspension. The precise time of impact is determined with the aid of an accelerometer embedded in the rod as well as a high-speed camera, which gives independent access to the instantaneous rod velocity and position. An immersed force sensor simultaneously records the stress transmitted to the container bottom directly below the rod.

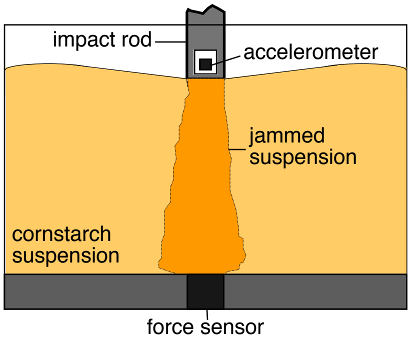

Figure 1: Experimental setup. The impact rod (grey) hits the cornstarch surface, creating a jammed region of suspension (dark orange) which transmits stress to the force sensor at the container bottom.

Fig. 2 shows a typical profile for the force on the rod F_{rod} and the force on the sensor at the container bottom F_b as a function the time after impact with a fill height H = 10.5 *cm* (impact velocity v_0 = 2.0 *m*/*s*, packing fraction ϕ = 0.49 and suspending fluid viscosity η = 1.0 *cP*). Even for modest impact velocities, this produces an incredibly large force on the rod. In this case, the maximum pressure on the rod face is about 500 *kPa* and the maximum deceleration ~35 *g*. The peak force on the rod does not necessarily show temporal correspondence with the peak force on the container bottom, indicating that the force on the rod is not solely a consequence of stress transmission to the container bottom (as is the case for smaller *H*). For the value of *H* in Fig. 2, a slow initial buildup of the force measured on the container bottom F_b is followed by an abrupt jump to its maximum value of ~7 *N* at $t \approx 7.5$ *ms*. After this, F_b and F_{rod} slowly die away. This is a consequence of both the slowing of the rod as the transmitted force decelerates it and also the concomitant "melting" of the suspension, as is described in the experiments [14] of von Kann *et al.* Given the area of the sensor is 1.13 *cm* and assuming the pressure on the bottom is roughly constant, we estimate that the total force on the rod is recovered over an area ~10 cm^2. This is much smaller than the full area of the container bottom (900 cm^2), and if we imagine the stress propagates through the suspension in a cone this corresponds to an angle of about 10° (we remark that this likely underestimates the cone angle given that the pressure is presumably not constant and highest directly below the rod).

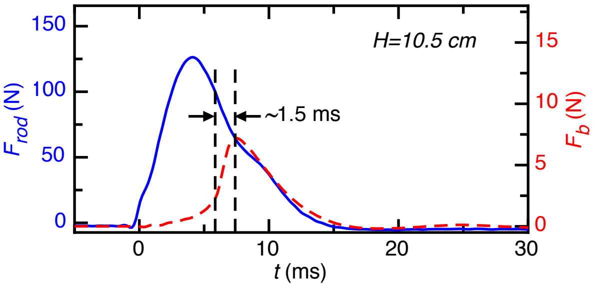

Figure 2: Force on rod F_{rod} (blue curve, left axis) and container bottom F_b (red dashed curve, right axis) vs. time after impact *t*.

The localization evident from Fig. 2 is the first signature jammed region of suspension transmitting the force on the rod to the container bottom in the manner of a solid. Once this solidified region has formed and reaches bottom, other solid-like behaviors are present. For example, in sufficiently shallow containers and sufficiently high impact speeds, the impacting rod can maintain large amounts of momentum once the growing solid has reached bottom. Rather than yielding and flowing along the bottom, however, the solid compresses, stores energy, and causes the rod to bounce off of the suspension surface. Although it is in principle possible that this energy storage comes from dilation causing grains to poke out from the liquid-air interface [3, 7, 8], we can rule out this possibility by observing that the presence a thin water layer on the suspension surface (~0.5 - 1.0 *cm*, which prevents particles from interacting with the air-water interface) does not eliminate the bounce. This leads us to conclude that the energy is in fact stored and released by compression of the grains, as is encountered for the elastohydrodynamic collision between fluid-coated steel spheres in "Stoke's Cradle" experiments [11, 12, 13]. In addition to transmitting stress locally on the container bottom, the jammed region also has a yield stress and can store elastic energy.

We can use shape of the F_b vs. *t* curves to probe the dynamic details of the solidification process. In particular, the time of the peak can be thought of as the time required for the leading edge of the growing solid to reach the lower boundary. In Fig. 2, for example, knowing that the peak occurs at $t \approx 7.5$ ms and *H* = 10.5 *cm* allows us to determine that, on average, the suspension solidifies at a rate of ~15 *m*/*s* (for v_0 = 2.0 *m*/*s*). From the sharp upturn to the peak in Fig. 2 (from about 5 - 7 *ms*), we can make a rough estimate of the width of the leading edge of the solidification region as $\delta \approx v_0 \Delta t \approx 4$ *mm*. Given that once the solid reaches bottom it must compress a little to develop the peak in F_b, this is likely an overestimate of the front width, but even so it indicates that the front is spatially well-defined in comparison to the size of the solidified region once it hits bottom (~10 *cm*).

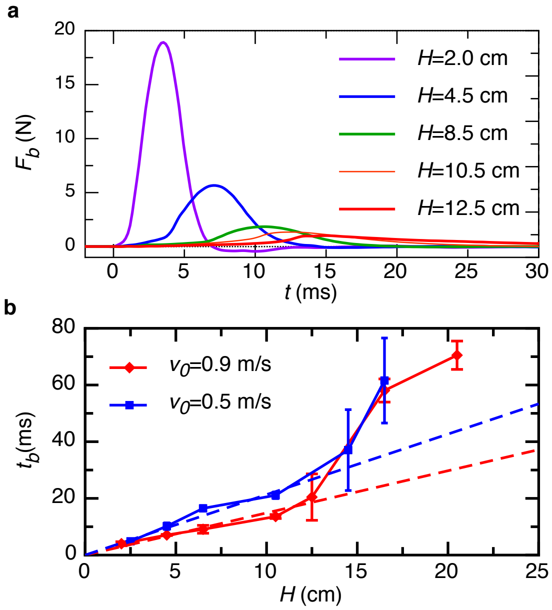

Figure 3: (a) Force on the container bottom (F_b) vs. time for impact at v_0 = 0.9 *m*/*s* and different fill heights *H*. (b) Time t_b for the peak in F_b vs. container height *H*. The error bars show the standard deviations over 3+ individual measurements.

We can gain more insight into this time-dependent solidification by investigating the F_b vs. *t* curves for different *H*, as in Fig. 3 (a). As might be expected, the scale of the recovered force decreases monotonically with increasing *H* and occurs later in time. The weaker force is a result of the decreased speed of the rod when the solid hits bottom as well as the continued spreading of the stress-cone for deeper containers. Plotting the time of the force peak t_b vs. *H* maps a trajectory of the solid growth, as in Fig. 3 (b). Rather than growing at a constant velocity, the solid develops quickly at first and then slows down. This is reminiscent of the rod trajectory and suggests that the speed of growth is influenced by the speed of the rod (see ref. [16] for example). To test this, we can plot the front trajectories for different impact speeds, which shows that higher speed impacts produce fronts with faster initial speeds (see the curves for $v_0 = 0.5$ and 0.9 m/s in Fig. 3 (b)). From fitting the portions of these curves before the slow-down we obtain an initial growth rate ~10 times faster than the speed of impact.

At first glance, the dependence of the solidification speed on the rod velocity seems similar to shocks in jammed granular systems [17]. A closer look, however, reveals important differences. The speed at which these fronts propagate seems to scale linearly with the impact speed. In the jammed granular system, two types of propagation are encountered, neither of which scale linearly. In the first case, when the impact speed is low, the front speed is constant and is simply set by the degree to which the grains are pre-compressed before impact (this is essentially sound propagation). In the case of high impact speed, the front speed scales like $v^{1/5}$ as a consequence of the impact causing the already compressed grains to compress further still. These sharp differences can be understood simply by realizing that the system here, unlike the granular system, is *not jammed* before impact; the impact causes it to jam. Given that it is initially unjammed, it cannot support sound propagation through the particle matrix, and it is therefore not surprising that the front speed is not constant but instead depends on the impactor velocity.

CONCLUSIONS

While previous experiments have suggested that under applied normal stress solidified regions of suspension can transmit stress to boundaries, our results give insight into the dynamic details of how this solidification occurs. We show that the solidified region is highly localized, extending over a very small area on the opposing boundary from the impact site. We find that the speed at which the suspension solidifies is set by the speed of the disturbance, with faster solidification occurring for more rapidly applied stress, and that the fronts are spatially well-defined. These results highlight distinct differences between steady-state, shear driven situations and phenomena driven by normal stress, showing that the latter is dominated by the inherently transient character of driving the suspension into the jammed state.

ACKNOWLEDGEMENTS

We thank Wendy Zhang, Tom Witten, Vincenzo Vitelli, Carlos Orellana, Sidney Nagel, Marc Miskin, William Irvine, Qiti Guo, Jake Ellowitz, Justin Burton, and Eric Brown for insightful discussions. This work was supported by the NSF through its MRSEC program (DMR-0820054). S. R. W. acknowledges support from a Millikan fellowship.

---

[1] N. J Wagner and J. F. Brady, Physics Today **62**, 27 (2009).
[2] X. Cheng, J. H. McCoy, J. N. Israelachvili and I. Cohen, Science **333**, 1276 (2011).
[3] E. Brown, N. A. Forman, C. S. Orellana, H. Zhang, B. W. Maynor, D. E. Betts, J. M. DeSimone and H. M. Jaeger Nature Materials **9**, 220 (2010).
[4] E. E. Bischoff-White, M. Chellamuthu and J. P. Rothstein, Rheol. Acta **49**, 119 (2010).
[5] J. F. Brady and G. Bossis, Annu. Rev. Fluid Mech. **20**, 111 (1988).
[6] B. J. Maranzano and N. J. Wagner, J. Chem. Phys. **114**, 10514 (2001).
[7] E. Brown, H. Zhang, N. A. Forman, B. W. Maynor, D. E. Betts, J. M. DeSimone and H. M. Jaeger, Phys. Rev. E **84**, 031408, (2011).
[8] E. Brown and H. M. Jaeger, M. Phys. Rev. Lett. **103**, 086001 (2009).
[9] M. E. Cates, M. D. Haw and C. B. Holmes, J. of Phys: Cond. Matt. **17**, S2517 (2005).
[10] D. Bi, J. Zhang, B. Chakraborty and R. P. Behringer, Nature **480**, 355 (2011).
[11] R. H. Davis and J. -M. Serayssol, J. Fluid Mech. **163**, 479 (1986).
[12] C. Donahue, C. Hrenya and R. Davis, Phys. Rev. Lett. **105**, 034501 (2010).
[13] C. Donahue, C. Hrenya, R. Davis, K. Nakagawa, A. Zelinskaya and G. Joseph, J. Fluid Mech. **650**, 479504 (2010).
[14] S. von Kann, J. H. Snoeijer, D. Lohse and D. van der Meer, Phys. Rev. E **84**, 060401 (2011).
[15] B. Liu, M. Shelley and J. Zhang, Phys. Rev. Lett. **105**, 188301 (2010).
[16] S. R. Waitukaitis and H. M. Jaeger, Nature **487**, 205 (2012).
[17] L. R. Gómez, A. M. Turner, M. van Hecke and V. Vitelli, Phys. Rev. Lett. **108**, 058001 (2012).

Rev. Cub. Fis. **29**, 1E34 (2012) CONTRIBUTIONS

FIELD INDUCED MICROPARTICLE STRUCTURE FORMATION IN FLUIDS

FORMACIÓN DE ESTRUCTURAS EN FLUIDOS INDUCIDAS POR CAMPO

G. Helgesen[a,b,c †], M. Knaapila[a] A. T. Skjeltorp[a,b,c], H. Høyer[a], J. Cernak[d]

a) Institute for Energy Technology, Kjeller, Norway, geir.helgesen@ife.no†
b) Department of Physics, University of Oslo, Norway
c) Centre for Advanced Study at The Norwegian Academy of Science and Letters, Oslo, Norway
d) P. J. Safarik University in Kosice, Slovak Republic
† corresponding author

We review how magnetic and electric fields can be used to create microparticle structures within fluids such as water, oil, polymers, or ferrofluids. The particular arrangement of the electrodes will strongly influence the morphology of the clusters or networks formed, as will also rotating or oscillating fields do. The structure and dynamics of such pattern formation will be described for various types of particles, such as colloidal microspheres, carbon nanoparticles, and metal particles.

Revisamos cómo los campos eléctricos y magnéticos pueden utilizarse para crear estructuras a partir de micropartículas en fluidos como agua, aceite, polímeros o ferrofluidos. El arreglo de electrodos utilizado influye poderosamente la morfología de los “clusters” en las redes que se forman, como también lo hacen los campos rotatorios u oscilatorios. Se describen la estructura y dinámica de la formación de éstos patrones para varios tipos de partículas, tales como microesferas coloidales, nanopartículas de carbono, y partículas metálicas.

PACS: Electrohydrodynamics, 47.65.-d; magnetohydrodynamics in fluids, 47.35.Tv; pattern formation in fluid dynamics, 47.54.-r

INTRODUCTION

Formation of aligned structures within fluids can be obtained by a range of techniques. It is known that mechanical shear in a flowing fluid can align nanoparticles in the fluid into linear chain-like structures [1]. Allowing the fluid to pass above a surface containing protruding micro- or nanostructures leads to similar effects. Static (DC) or oscillating (AC) electric fields may be employed to assemble and align uncharged dielectric particles. Similarly, relatively weak magnetic fields may be used to align dia- or paramagnetic particles.

The motion of charge-neutral particles in a fluid induced by inhomogeneous electric field (AC or DC) is called dielectrophoresis [1]. Magnetophoresis is the similar effect of motion of dia-/paramagnetic particles induced by inhomogeneous magnetic fields [1]. In these two processes a single particle will first be polarized (electrically or magnetically) by the difference in the dielectric constant or the magnetic permeability between the particle and its surrounding carrier fluid. This induced dipole is then pushed away from or attracted toward the source of the field by the field gradient. If another similar particle is placed in the neighborhood of the first, they interact with dipolar forces and will be attracted or repelled depending on the angle between a vector $\boldsymbol{r}_{ij}$ joining their centers and the direction of the external field. Thus, spherical microparticles in an external field interact via the dipolar potential

$$U \propto \sum_{i\neq j} \frac{1}{r_{ij}^3}\left[\sigma_i\cdot\sigma_j - 3\left(\sigma_i\cdot\boldsymbol{u}_{ij}\right)\left(\sigma_j\cdot\boldsymbol{u}_{ij}\right)\right], \tag{1}$$

where σ_n is the electric dipole moment $\boldsymbol{p}_n$, or the magnetic moment $\boldsymbol{m}_n$, of the n-th particle, see Table 1. Here, $\boldsymbol{u}_{ij}$ is a unit vector in the direction of $\boldsymbol{r}_{ij}$. In addition, any gradient in the external E- or H-field gives rise to a single particle force with a direction that depends only on the difference ε_2 - ε_1 of the dielectric constants, or μ_2 - μ_1 of the permeabilities, of the particles and the fluid, respectively. This is outlined in Table 1.

MICROPARTICLE ALIGNMENT IN FLUIDS

Figures 1 (a) and 1 (b) show some examples of dielectrophoretic alignment of microparticles using AC electric fields. Figure 1 (c) shows chain formation of magnetic particles in water in a very weak magnetic field [2] and Fig. 1 (d) shows alignment of nonmagnetic polystyrene spheres dispersed in a ferrofluid [3] in a constant magnetic field $H \approx 800\ A/m$ [4]. The growth dynamics of such chains follow the cluster-cluster aggregation model [5] where the typical cluster length L grows with time t as $L(t) \sim t^z$ with $z \approx 0.5$ [6]. Also, the distribution of cluster sizes at different times can be rescaled to a common, “universal” functional form [4]. Using an in-plane rotating magnetic field circularly shaped aggregates can be obtained instead of linear strings [7]. Similar structures have been found in experiments

Table I
Electric and magnetic force expressions

External *E*-field Force on electric dipole p	$F_{edip} = (p \cdot \nabla) E_0$	
Dipole moment of sphere with radius a inside fluid	$p = 4\pi\varepsilon_1 \left(\frac{\varepsilon_2 - \varepsilon_1}{\varepsilon_2 + 2\varepsilon_1} \right) a^3 E_0$	Dielectric constants: ε_1 for fluid ε_2 for particles
Dielectrophoretic force on spherical particle	$F_{DEP} = 2\pi\varepsilon_1 K(\varepsilon_1, \varepsilon_2) a^3 \nabla \left(E_0^2 \right)$	$K(\varepsilon_1, \varepsilon_2) = \left(\frac{\varepsilon_2 - \varepsilon_1}{\varepsilon_2 + 2\varepsilon_1} \right)$ Clausius-Mosotti factor
External *H*-field Force on magnetic dipole m	$F_{mdip} = \mu_0 (m \cdot \nabla) H_0$	
Magnetic moment of sphere inside fluid	$m = 4\pi\mu_1 \left(\frac{\mu_2 - \mu_1}{\mu_2 + 2\mu_1} \right) a^3 H_0$	Magnetic permeabilities: μ_1 for fluid μ_2 for particles
Magnetophoretic force on spherical particle	$F_{MAP} = 2\pi\mu_1 K(\mu_1, \mu_2) a^3 \nabla \left(H_0^2 \right)$	$K(\mu_1, \mu_2) =$ magnetic Clausius-Mosotti factor

and computer simulations of soft magnetic microparticles in uniaxial and biaxial magnetic fields [8] and 3-D networks of strings inside composites have been found using triaxial magnetic fields [9].

PARTICLE ALIGNMENT FOR CONDUCTIVE COMPOSITES

Field-assisted microparticle alignment in polymer dispersions is a convenient and efficient way to create conductive composites with very low loading of conductive fillers. Typical schemes to do this is shown in Fig. 2. A very low volume fraction of conductive nano- or microparticles, such as carbon black (CB), carbon nano-disks and cones (CNC), graphite or metal particles, is dispersed in the polymer and made into a thin (10 – 100 μm) layer on top of a pair of in-plane metal electrodes as shown in Fig. 2 (a) - (c) [10, 11, 12]. The electrodes may be electrically insulated from the polymer dispersion using a plastic foil. Then, an AC voltage is applied between the electrodes and after a few seconds to about a minute, the conductive particles are assembled and aligned into chains by the electric field. These chains may span the gap between the electrodes, thus making a conductive channel in the polymer matrix. The field may alternatively be applied between a bottom and a top electrode giving rise to conductive chains from one side of the layer to the other, Fig. 2 (d). The polymer can then be cured by heat or UV-light and the conductive chains are locked in place. Finally, the electrodes may be detached from the electrodes (Fig. 2 (c)), creating a free-standing film that is conductive either in-plane or perpendicular to the sheet.

The growth speed depends on the *E*-field strength and particle concentration as well as the configuration and separation of the electrodes [13]. Typical concentration of filler particles in these conductive films are 0.2 – 1.0 vol-%. This is well below the isotropic percolation limit for conductivity in such mixtures which is typically 2 – 5 *vol*-%. During the alignment, the electrical conductivity of the material rises from the conductivity of the pure polymer ~10^{-6} S/m up to 10^{-3} – 10 S/m, depending on the type of filler particle. This conductivity increase takes place during the first minute of alignment and after that there is only a smaller increase as the chains reach their optimal configuration [11, 12]. Some type of chain rearrangement such as merging of two nearby chains and formation of “branched roots” at the electrodes may be seen but this has only a minor influence on the conductivity. After curing of the polymer the conductivity remains fixed. Figure 3 (a) and (b) show the cross section of a sample containing

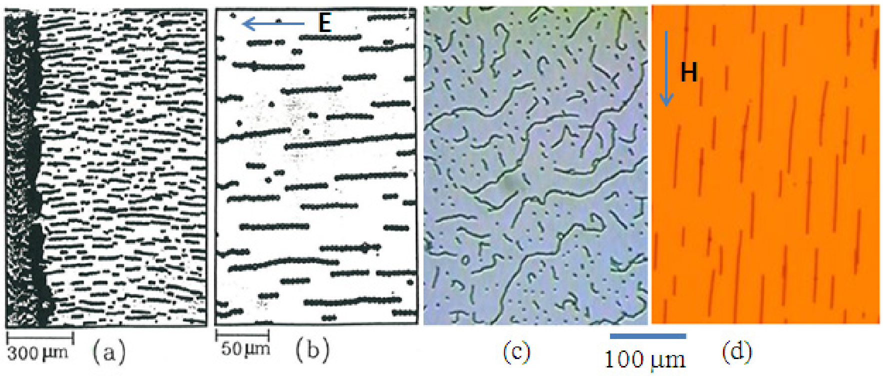

Figure 1: (a) and (b) Electric alignment of 5 μm polystyrene spheres in water at field frequency $f = 1$ kHz and $E = 5$ V/mm. (c) Permanent magnetic microbeads in a very weak in-plane magnetic field. (d) Alignment of 4 μm polystyrene microspheres in a ferrofluid.

0.2 *vol*-% CNC with field perpendicular to the layer (Fig. 2 (d)) before and after the alignment process [11].

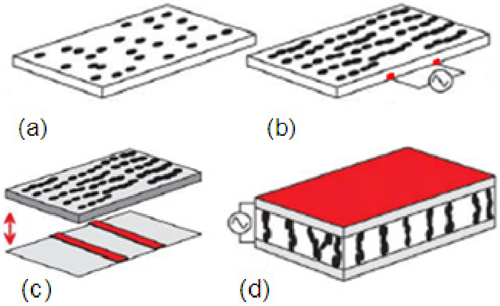

Figure 2: Alignment of particles in thin layers into conductive strings.

An array of electrodes with length 2 *cm* and spacing 100 μm and a field with frequency $f = 1$ *kHz* and strength $E = 200$ *V*/*mm* were used to produce the in-plane CNC channels seen in Fig. 3 (c) [10]. Using two needle-shaped gold electrodes on top of a 250 μm thick silicon substrate, the single CB string seen in Fig. 3 (d) was formed in about 100 *s* in an AC field with $E = 300$ *V*/*mm* [14, 15]. After UV curing, the substrate was bent slightly, resulting in a reversible resistivity change of the string by about 15%. Such strings may be used as strain sensors. No such change was detectable in a similar, isotropically filled sample containing 12 *vol*-% CB. Thus, the piezoresistivity is an effect of the particle alignment. Similar field-structured composites using magnetic fields and Au-coated Ni particles in epoxy have been studied by Martin *et al.* [16]. Such composites may have interesting thermoresistive, piezoresistive, and chemiresistive properties.

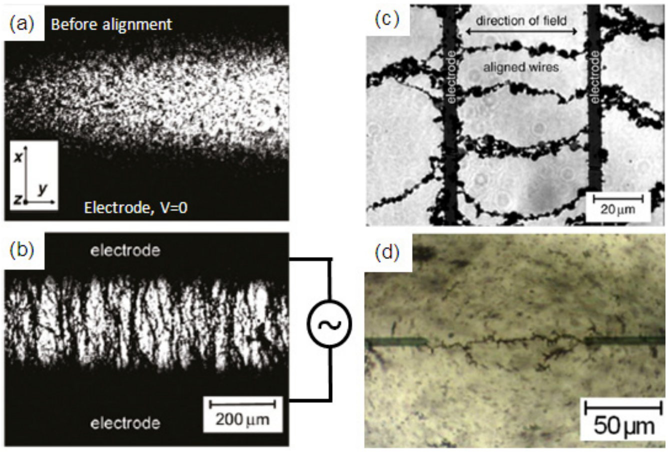

Figure 3: (a) and (b) Cross section of 0.2 *vol*-% CNC in polymer sample before and after field alignment. (c) In-plane alignment of CNC. (d) Single string of CB particles formed between two needle-shaped electrodes.

CONCLUSIONS

Electric or magnetic alignment of particles can be used to create nanostructured conducting composites. Such materials may find applications within the solar energy industry and in electrostatic discharge materials, battery, and sensor applications.

ACKNOWLEDGEMENTS

The authors thank G. K. Johnsen of Institute for Energy Technology and M. Buchanan of CondAlign AS for stimulating discussions, J. P. Pinheiro of n-Tec AS for providing carbon nanoparticles, and J. Kjelstrup-Hansen of University of Southern Denmark for preparing electrodes used in the experiments.

---

[1] H. Bruus, *Theoretical microfluidics* (Oxford University Press, Oxford, 2008).
[2] G. Helgesen and A. T. Skjeltorp, J. Appl. Phys. **69**, 8278 (1991).
[3] R. E. Rosensweig, *Ferrohydrodynamics* (Cambridge University Press, Cambridge, 1985).
[4] J. Cernak, G. Helgesen, and A. T. Skjeltorp, Phys. Rev. E **70**, 031504 (2004).
[5] T. Vicsek and F. Family, Phys. Rev. Lett. **52**, 1669 (1984).
[6] S. Miyazima, P. Meakin, and F. Family, Phys. Rev. A **36**, 1421 (1987).
[7] J. Cernak and G. Helgesen, Phys. Rev. E **78**, 061401 (2008).
[8] J. E. Martin, E. Venturini, J. Odinek and R. A. Anderson, Phys. Rev. E **61**, 2818 (2000).
[9] J. E. Martin, Composites A **36**, 545 (2005).
[10] M. Knaapila, J. P. Pinheiro, M. Buchanan, A. T. Skjeltorp and G. Helgesen, Carbon **49**, 3171 (2011).
[11] M. Knaapila, O. T. Rømoen, E. Svåsand, J. P. Pinheiro, Ø. G. Martinsen, M. Buchanan, A. T. Skjeltorp, and G. Helgesen, Appl. Mater. Interfaces **3**, 378 (2011).
[12] Matti Knaapila, Henrik Høyer, Eldrid Svåsand, Mark Buchanan, Arne T. Skjeltorp and Geir Helgesen, J. Polymer Science B **49**, 399, (2011).
[13] E. Svåsand, G. Helgesen and A. T. Skjeltorp, Colloids and Surfaces A **308**, 67 (2007).
[14] H. Høyer, M. Knaapila, J. Kjelstrup-Hansen, X. Liu and G. Helgesen, Appl. Phys. Lett. **99**, 213106 (2011).
[15] H. Høyer, M. Knaapila, J. Kjelstrup-Hansen, X. Liu and G. Helgesen, J. Polymer Science B **50**, 477 (2012).
[16] J. E. Martin, R. A. Anderson, J. Odinek, D. Adolf and J. Williamson, Phys. Rev. B **67**, 094207 (2003).

DIPOLAR ORDERING OF CLAY PARTICLES IN VARIOUS CARRIER FLUIDS

ORDENAMIENTO DIPOLAR DE PARTÍCULAS DE ARCILLA EN DIVERSOS FLUIDOS

Z. Rozynek[a †], H. Mauroy[b], R. C. Castberg[c], K. D. Knudsen[b] and J. O. Fossum[a,d ‡]

a) Department of Physics, NTNU, Høgskoleringen 5, NO-7491 Trondheim, Norway, rozynek@ntnu.no†, jon.fossum@ntnu.no‡
b) Physics Department, IFE, NO-2027 Kjeller, Norway
c) Department of Physics, University of Oslo, P.O.Box 1048, NO-0316 Oslo, Norway
d) Centre for Advanced Study at the Norwegian Academy of Science and Letters, Drammensveien 78, NO-0271 Oslo, Norway
†, ‡ corresponding authors

We investigate here examples of complexity in composite materials. The objective of the paper is to show that clay particles can be aligned in different hosting media, such as: silicone oil, paraffin-wax, polystyrene and ambient air. The use of an electric field is an easily controllable, non-intrusive manner of inducing such an alignment. Depending on the medium used, a large span in time constants for the orientation and reorganization has been observed. Furthermore, the reorientation may be frozen into the material, thus permanently changing its properties.

Se investigan ejemplos de complejidad en materiales compuestos. El objetivo de este artículo es demostrar que se pueden alinear partículas de arcilla en diferentes medios como aceite de silicona, parafina-cera, poliestireno, y aire. El uso de un campo eléctrico resulta una vía fácilmente controlable y no-intrusiva de inducir el alineamiento. Se observa un amplio rango de constantes de tiempo para la orientación y la reorganización en dependencia del medio utilizado. Aún más, la reorientación puede congelarse en el material, de tal suerte que sus propiedades cambian permanentemente.

PACS: Granular materials rheology, 83.80.Fg; pattern formation in granular systems, 45.70.Qj; rocks magnetic and electrical properties, 91.25.F-; colloids, 82.70.Dd

INTRODUCTION

Application of an external electric field to a suspension of dielectric clay particles induces polarization of the particles. They will consequently re-orient and aggregate, and this results in the formation of a columnar structure parallel to the electric field direction. The clay particles polarize along their silica sheets, i.e. their stacking direction will be normal to the direction of polarization [1]. The mechanism of the polarization in clays is still under discussion, although one hypothesis is that the intercalated ions and water molecules, which are movable, could play a central role in particle electrical polarization. The resulting induced dipole is attached structurally to the clay particle, and this causes clay particles to reorient and interact, as suggested in [1]. However, recent measurements performed by us indicate that the contribution from the outer surface charges may be dominant, and the particle alignment is then determined by its shape, i.e. so that the longest axis of a single clay particle (or aggregate of particles) will be parallel to the direction of *E*-field lines [2].

The clay polarization is a rapid process ($< \mu s$) that is followed by a particle re-orientation with a rotation time proportional to the carrier fluid viscosity and inversely proportional to: firstly the difference in the dielectric constants between particle and medium; and secondly the electric field squared (see also [3]). The time scale for particle rotation is in the range of 10^{-3} to 10^{1} s, for *E*-field between 50 and 2000 V/mm and viscosity of carrier fluid such as silicone oil between 100 and 500 $mPa{\cdot}s$ [2]. If the particle concentration is high enough, and a minimum critical *E*-field is applied, chain formation occurs via a particle dipole-dipole interaction [4].

The phenomena described above may be utilized in many different ways and just a few examples are: (i) Electro-rheological fluids (clay particles in silicone oil) in which the so-called liquid-to-solid reversible transition occurs via the application of an external *E*-field. Such a transition is manifested by changes of ER properties, namely: viscosity, yield stress, storage and loss moduli, etc. [5, 6, 7]. Some examples of application of ER fluids are: fast acting hydraulic valves or clutches [8]. (ii) Nanocomposites (clay particles in polymers), since the aspect ratio of the clay platelets and the interfacial contact area between the clay and matrix are high, the incorporation of small amounts of such inorganic filler into a polymer medium can significantly improve the properties of the resulting polymer/clay nanocomposites. Such nanocomposites can attain a high degree of stiffness and strength [9]. Furthermore, the presence of the dispersed phase results in additional properties, such as flame retardancy or enhanced barrier properties (e.g. gas permeability), when compared to either component [10, 11]. In many situations it is not only the *presence* of the well-dispersed filler but also its *orientational* ordering that may improve certain physical and chemical properties. The electric-field-induced alignment of clay particles can thus be used to obtain and control a range of the desired material properties.

The above examples have clearly an application-oriented character. However, the focus of our studies is on better understanding of basic physics of such complex systems. Apart from already mentioned hosting media, we also here report for the first time structuring from clays in atmospheric air. The common denominator, for all studied systems, is the clay particle alignment in the presence of an *E*-field.

SAMPLES

Two types of clay particles, namely laponite (Lp) and fluorohectorite (Fh) are used in the present investigations. The synthetic Lp clay was purchased from Laponite Inc. and the synthetic Fh clay was purchased from Corning Inc. They both belong to the smectite family of clay minerals. Smectites are 2:1 phyllosilicates that possess a net negative charge on the surface of each crystalline layer. Counter ions are located between these lamellar sheets to balance for that charge. Exchangeable cations such as Na^+, Li^+, Ca^{2+}, Mg^{2+}, Cu^{2+} or Fe^{2+} are common. The chemical formulas are: $Na^{+}_{0.7}[(Mg_{5.5}Li_{0.3})Si_8O_{20}(OH)_4]^{0.7-}$ for Lp clay and $Na^{1.2+}[(Mg_{4.8}Li_{1.2})F_4Si_8O_{20}]^{1.2-}$ for Fh clay, respectively. They are silicates where a fraction of Mg^{2+} ions is substituted by Li^+ in trioctahedral sites resulting in a negative structural charge [12]. Fluorohectorite has been reported from X-ray data to retain a stacked structure of lamellar particles composed of between 20 and 100 unit layers when dispersed in water, whereas laponite is known to exfoliate into single unit layers in aqueous suspensions [13]. The individual Lp clay particle resembles a disc of average diameter around 30 *nm*, whereas the size of Fh clay can be as large as several *µm*.

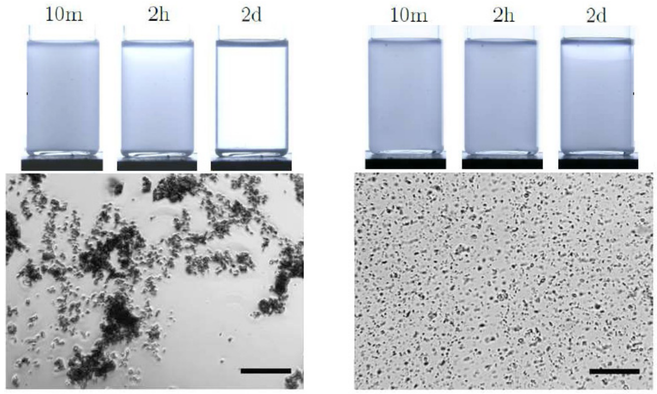

Non-modified Fh

CTAB modified Fh

Figure 1: Microscope images of non-modified Fh (left) and organically modified CTAB-Fh (right) clay particles suspended in silicone oil. The length of the bar corresponds to 200 *µm*. The pictures of the glass vials with samples (top) illustrate the sedimentation dynamics. Adopted from [16].

Clays, in their natural forms, are hydrophilic, or depending on the context they may be referred to as organophobic. When suspended in a non-polar medium, such as silicone oil or polymeric matrix, they tend to form large agglomerates and and consequently sediment (see Figure 1). Addition of surfactants is commonly used to prevent particle agglomeration, which then slows down particle sedimentation, or if the particles are small enough (i.e. magnetic particles in ferrofluids), ensures that they are held in suspension by Brownian motions [14]. Another reason for modifying clays is the ease of uniform dispersion in an apolar polymer matrix. To promote compatibility between the inorganic filler and apolar polymers, it is necessary to chemically modify the inorganic clays by intercalation of organophilic cations, which expand the interlamellar space of the clay, decreasing the interaction among the silicate sheets, and facilitating the diffusion and accommodation of polymeric chains [15].

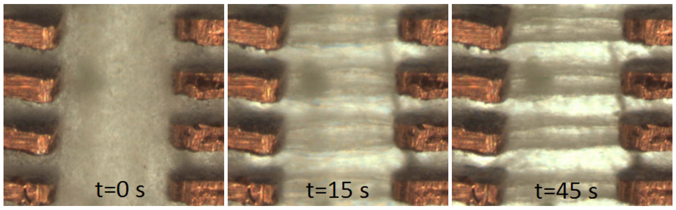

Figure 2: Optical microscopy images of clay/oil suspension without *E*-field applied (left) and a field of 1000 *V*/*mm* (middle and right).

RESULTS

Clays in silicone oil. The preparation of the ER fluid was undertaken by the following procedure. Na-Fh clay powder was crushed with a pestle and mortar, weighed and placed in an oven for 12 *h* at 110 °*C*. The silicone oil was heated at the same conditions. Subsequently, the clay powder and silicone oil were mixed in glass tubes and sealed. The solutions were then vigorously hand-shaken for 2 *min* and placed in an ultrasonic bath for 1 *h*. Before each measurement the samples were hand-shaken again. The clay concentration was approximately 5 *wt*.%.

Firstly, optical observations were conducted. For that purpose the ER fluid was placed between two electrodes with pre-defined shapes as shown in Figure 2. The gap between the electrodes is roughly 1 *mm* and the electric field is applied horizontally.

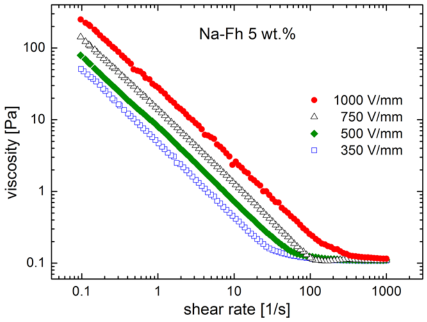

Figure 3: Flow curves for 5 *wt*.% clay particles suspended in silicone oil. Different electric field strengths are used, influencing the shear viscosity.

When no *E*-field is applied, the Fh particles are randomly dispersed into the silicone oil, as shown in Figure 2 (left). Microscopy images of the sample under a DC electric field of 1000 *V*/*mm* taken at different times, 15 *s* and 45 *s* are shown in Figure 2 (middle and right). The formation of column-like structures aligning parallel to the field is clearly observed. Several thin chains are formed first, and these subsequently attract each other resulting in the creation of thicker columns. After a certain time (here several minutes) no major changes in the system are noticeable.

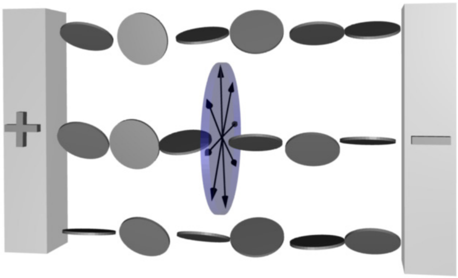

Figure 4: The sketch of the clay alignment in so-called anti-nematic configuration (see text for details).

Imagine now shearing the ER fluid parallel to the *E*-field direction. If the *E*-field is not present, the shear viscosity of such a sample (silicone oil and only 5 *wt*.% of clay) is close that of pure silicone oil. However, once the electric field is applied, so that the particles are oriented against the flow, the shear viscosity of a fluid containing clay particles is expected to increase. As the curves in Figure 3 show, this is also what is seen experimentally.

Clays in paraffin-wax. The particular type of paraffin-wax used here has its melting point around 65 ºC and was chosen for two major reasons: (i) optimal melting and crystallization temperatures, providing both easy composite preparation and appropriate stiffness of the composite when in solid form at room temperature; (ii) a relatively non-polar and non-conductive material that can be used as an electrorheological carrier fluid when in the melted state. Fluorohectorite particles (~5 *wt*.%) were dispersed in the melted paraffin and then poured into a custom-made mould with two electrodes. The electric field strength of 500 *V*/*mm* was applied and kept for a few minutes until the paraffin crystallized and cooled down to room temperature. The solid composite was then investigated using wide-angle X-ray scattering.

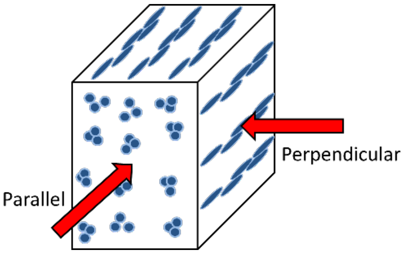

Figure 5: Simple sketch of what the X-ray beam probes in the sample.

When a 2-D X-ray pattern (like those shown in Figure 6) is integrated along the radial direction with a narrow q-range (2θ-angle) around the Bragg ring, one obtains a 1-D azimuthal plot which is then fitted using a parametric function. The fitting allows extracting parameters that are further used to calculate the nematic order parameter (S_2) (for details see [17]). This parameter ranges from -1/2 to 1, where 1 indicates perfectly oriented particles in the nematic configuration, 0 means no orientational order, and finally -1/2 indicates perfectly oriented particles in the anti-nematic configuration [6, 17, 18]. It is expected that the clay particles align in the anti-nematic geometry and the validity of such assumption is tested below.

Several 2-D X-ray images were taken from the same sample at different polar angles, with the rotation axis parallel to the reference direction, which is here the direction of the *E*-field. The nematic order parameter was calculated for four sample positions and the results are presented in Table 1.

Table 1.
Nematic order parameter as a function of the polar angle, with the rotation axis parallel to the direction of *E*-field lines.

Sample rotation	0	30	60	90	Avg
Order parameter	-0.37 ±0.01	-0.35 ±0.01	-0.37 ±0.02	-0.36 ±0.01	-0.36 ±0.01

We observe that the nematic order parameters do not differ significantly from each other indicating that there is no preferential orientation along the polar angle. The arrowed disc shown in Figure 4 represents the plane parallel to the *E*-field direction, and that is in fact the average particle stacking direction. The black arrows indicate that clay normals are oriented without any preferred polar direction.

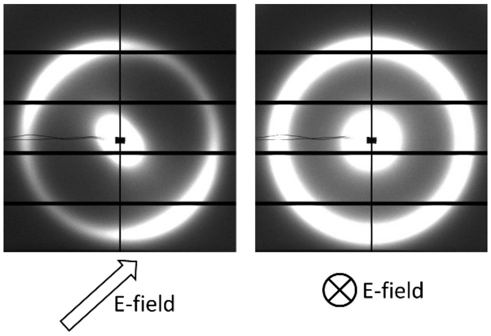

Figure 6: SAXS-patterns from PS/CTAB-Fh with permanently aligned clay chains. Remark: the sample is tilted 45 degrees in the x-y plane.

Clays in polystyrene. When aligning clay particles in liquid media the alignment may be lost after a while when the electric field is turned off. An approach to freeze the chain structure was tested by solidifying the matrix while the electric field was applied. The matrix, styrene monomer, polymerizes to give solid polystyrene polymer (PS). A 1 *wt*.% sample of organically modified CTAB-Fh (see [16] for details) was dispersed in styrene monomer and a small quantity of a radical initiator, benzoyl peroxide, was added. The clay/monomer suspension was filled in square shaped glass capillaries, which were sealed with a flame torch. The capillaries were then immersed in an 80 ºC silicone oil bath, and placed between two plate electrodes. The electric field over the electrodes was set to 830 *V*/*mm*, and the samples were left to polymerize for 7 days. The resulting PS-clay composites were investigated with small angle X-ray scattering (SAXS) at the Dubble beam line at ESRF in Grenoble, France. The samples were probed with the X-ray beam perpendicular and parallel to the direction of clay chains (see

Figure 5). The main ring comes from the characteristic spacing between clay crystalline sheets, and d_{001}~4 *nm*. A pronounced anisotropy of the d_{001} peak is seen in Figure 6 (left) due to clay alignment, i.e. on average, particles orient with their stacking direction parallel to the *E*-field lines. When probed along the chains the pattern looks isotropic, as shown in Figure 6 (right), since there is no preferential orientation of clay particles along the polar angle (see also [18, 19]).

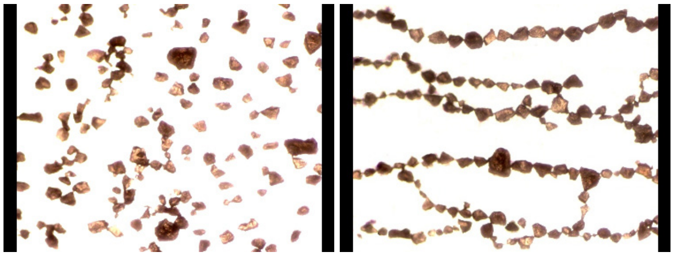

Figure 7: Laponite particle aggregates between two electrodes without *E*-field applied (left) and with an AC *E*-field of 500 *V/mm* (right). The images have been edited to enhance the contrast.

Clays in air. As the final example, we show laponite clay alignment in atmospheric air. Laponite clay powder stored in our laboratory at ~23 º*C* and RH in range between 10 and 30 % was used. Such particles normally form aggregates and their sizes can span a few orders of magnitudes reaching a few *mm*. In the present work the size of the aggregates were between 10 and 100 *μm*. Figure 7 shows clay particle aggregates between two electrodes with no *E*-field applied (left) and with an AC *E*-field of 500 *V/mm* (right). The electrodes were kept horizontally and images were taken from above. Clay particles lied on a thin glass substrate, and when the electric field was applied the set-up was gently tapped, lowering the friction as the particles were momentarily suspended in air.

As can be seen, most of the clay particle aggregates align with their longest axis along the *E*-field direction. However, there are several particles disobeying that rule, and these making bridges between individual chains allowing for charge transport. It is possible that the dominant part of the clay polarization occurs only on the clay aggregate surface, not the bulk, i.e. in the clay galleries. However, it is difficult (if not impossible) to draw a firm conclusion on this point, since we deal here with large aggregates. Therefore our future work will be focused on reducing the complexity of the system by working with *single* clay particles, such as vermiculite.

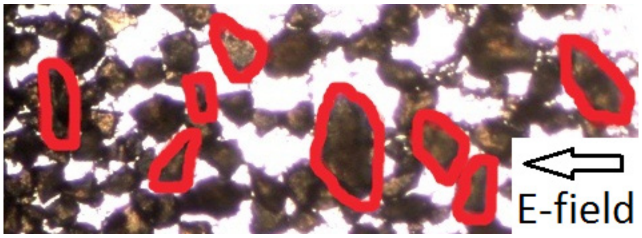

Figure 8: High concentration of laponite particle aggregates between two electrodes with an AC *E*-field of 500 *V/mm* applied. Several particle aggregates (red-color-marked) were not able to re-orient fully with their longest axis along the *E*-field lines due to jamming. This will effectively lower the value of the nematic order parameter.

In Figure 8 we also present structuring from particles in air, but this time the clay concentration is significantly higher. A possible jamming transition may occur where many particles have very little freedom to re-orient (see red-coloured particles). This is an ongoing study and more results are expected in the near future.

CONCLUSION

We have provided examples of recent results from our work on manipulation and orientation of asymmetric particles in external fields. Clay particles are ideal for this purpose due to their inherent large anisotropy and correspondingly high degree of polarizability. When placed in an apolar medium and subjected to an electric field, the particles will orient and organize within a time frame that depends principally on factors such as *E*-field strength and viscosity of the surrounding medium. We have shown how these effects may be induced in various media, with a large span in viscosity, from silicone oil, via polymer matrices to solidified wax, and even air. The clay particles may form chains that span the entire sample volume, thus changing the macroscopic properties of the material. Most notably, there will generally be a large change in the overall rheological behavior, and materials of this kind are therefore highly interesting for applications where the mechanical and structural properties should be manipulated via an electric field.

ACKNOWLEDGEMENTS

This work was supported by the Research Council of Norway through the Programs: NANOMAT project number 182075, and FRINAT project number 171300.

---

[1] J. O. Fossum, Y. Méheust, K. P. S. Parmar, K. D. Knudsen, K. J. Måløy and D. M. Fonseca, Europhys. Lett. **74**, 438 (2006).
[2] R. C. Castberg, Z. Rozynek, J. O. Fossum, K. J. Måløy and P. Dommersnes, work in progress
[3] R. C. Castberg, Z. Rozynek, J. O. Fossum, K. J. Måløy, P. Dommersnes and E. G. Flekkøy, Rev. Cub. Fis. **29**, 1E17 (2012).
[4] J. D. Jackson, *Classical Electrodynamics*, (Wiley 143, 1962).
[5] B. Wang, M. Zhou, Z. Rozynek and J. O. Fossum, J. Mater. Chem. **19**, 1816 (2009).
[6] Z. Rozynek, K. D. Knudsen, J. O. Fossum, Y. Méheust and B. Wang, J. Phys: Condens. Matter. **22**, 324104 (2010).
[7] Y. Méheust, K. Parmar, B. Schjelderupsen and J. O. Fossum, J. Rheol. **55**, 809 (2011).
[8] J. Madeja, Z. Kesy and A. Kesy, Smart Mater Struct. **20**, 105005 (2011).
[9] A. Esteves, A. Timmons and T. Trindade, Quim. Nova **27**, 798 (2004).
[10] S. S. Ray and M. Okamoto, Prog. Polym. Sci. **28**, 1539

(2003).
[11] S. Letaief and C. Detellier, J. Mater Chem. **17**, 1476 (2007).
[12] P. D. Kaviratna, T. J. Pinnavaia and P. Schroeder, J. Phys. Chem. Solids **57**, 1897 (1996).
[13] E. DiMasi, J. O. Fossum, T. Gog and C. Venkataraman, Phys. Rev. E **64**, 061704 (2001).
[14] Z. Rozynek, A. Jozefczak, K. D. Knudsen, A. Skumiel, T. Hornowski, J. O. Fossum, M. Timko, P. Kopecansky and M. Koneracka, Eur. Phys. J. E **34**, 28 (2011).
[15] K. S. Santos, S. A. Liberman, M. A. S. Oviedo and R. S. Mauler, J. Polym. Sci. B: Polym. Phys. **46**, 2519 (2008).
[16] Z. Rozynek, B. X. Wang, J. O. Fossum and K. D. Knudsen, Eur. Phys. J. E **35**, 9 (2012).
[17] Y. Méheust, K. D. Knudsen and J. O. Fossum, J. Appl. Cryst. **39**, 661 (2006).
[18] I. Dozov, E. Paineau, P. Davidson, K. Antonova, C. Baravian, I. Bihannic and L. J. Michot, J. Phys. Chem. B **115**, 7751 (2011).
[19] Z. Rozynek, R. C. Castberg, A. Mikkelsen and J. O. Fossum, work in progress.

VORTEX FLOW AROUND A CIRCULAR CYLINDER NEAR A PLANE

FLUJO DE UN VÓRTICE ALREDEDOR DE UN CILINDRO CERCA DE UN PLANO

M. N. Moura† and G. L. Vasconcelos

Departamento de Fìsica, Universidade Federal de Pernambuco, marcelmoura@yahoo.com.br†
† corresponding author

The study of vortex flows in the vicinity of multiple solid obstacles is of considerable theoretical interest and practical importance. In particular, the case of flows past a circular cylinder placed above a plane wall has attracted a lot of attention recently. In this case, a stationary vortex is formed in front of the cylinder, in contradistinction to the usual case without the plane where a vortex pair is observed behind the cylinder. In the present work, we apply modern complex analysis techniques to obtain the complex potential for the problem of one point-vortex placed in a uniform stream past a circular cylinder above a plane. A typical streamline pattern is also showed.

El estudio de flujos de vórtices en la vecindad de múltiples obstáculos sólidos es de gran interés teórico y de importancia práctica. En particular, el caso de los flujos alrededor de un cilindro circular colocado encima de una pared plana ha atraído mucha atención recientemente. En este caso, se forma un vórtice estacionario delante del cilindro, en contraposición con el caso habitual sin el plano, donde se observa un par de vórtices detrás del cilindro. En el presente trabajo, se aplican modernas técnicas de análisis complejo para obtener el potencial para el problema de un vórtice puntual colocado en una corriente uniforme alrededor de un cilindro circular colocado encima de un plano. Se muestra un esquema de líneas de corriente típico.

PACS: Vortex dynamics (fluid flow), 47.32.C-; vortices in inviscid laminar flows, 47.15.ki; Complex variables, 02.30.Fn

INTRODUCTION

The formation of vortices in viscous flows past cylindrical structures is a problem of considerable theoretical interest and practical relevance for many applications [1]. For example, in the case of a flow past a circular cylinder a pair of counter-rotating vortices forms behind the cylinder at small Reynolds numbers. This vortex pair then goes unstable at higher Reynolds numbers and evolves into a von Kármán vortex street. This system was first studied analytically by Föppl in 1913 [2]. Modelling the vortex flow in terms of point vortices in an otherwise inviscid and irrotational flow, Föppl was able to find stationary configurations for a pair of vortices behind the cylinder and analyze their stability. (Part of Föppl's original stability analysis was however an error, as it has been pointed out by several authors [3, 4].) Because it is amenable to analytical treatment, the point-vortex model is an important tool to study the basic aspects of vortex dynamics in real fluids. In addition, the study of vortex phenomena directly from the Navier-Stokes equation is very costly computationally, which makes the point-vortex model even more attractive.

The problem of vortex flow in the presence of several solid boundaries (obstacles) is much more difficult, and theoretical studies for such cases are more sparse in the literature. One geometry of particular interest is that of a uniform flow past a circular cylinder placed above a planar solid wall, where vortices can form upstream of the cylinder [5]. Here we wish to investigate this problem in terms of a point-vortex model. More specifically, we consider a point vortex of intensity Γ placed in a uniform stream of velocity U past a circular cylinder of radius s, whose center lies at a distance d from a plane; see Fig. 1. The main objective of the present paper is to derive the complex potential for this system. A typical streamline pattern of the flow will also be presented.

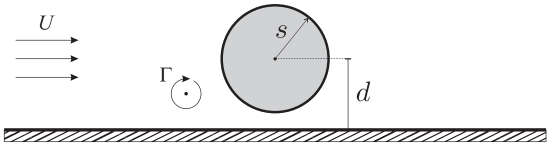

Figure 1: Point vortex in a uniform stream past a circular cylinder above a plane.

Since the fluid domain for the case in study (Fig. 1) is not simply connected (nor can it be reduced to a simply connected region by symmetry arguments), we need to consider conformal mappings between multiply connected domains in order to compute the complex potential for the flow. More specifically, we shall make use of a mathematical formalism recently developed by Crowdy and Marshall [6], which is based on the so-called Schottky-Klein prime function, as discussed next.

METHODOLOGY

We assume that the fluid is inviscid, irrotational, and incompressible, so that the fluid velocity $\vec{v}(x,y)$ is given by the gradient of a potential function: $\vec{v} = \nabla\phi$, where the velocity potential $\phi(x,y)$ obeys Laplace equation: $\nabla^2\phi=0$. Our main goal here is to compute the complex potential $w(z)=\phi(x,y)+i\psi(x,y)$, where ψ is the so-called stream function, for the problem illustrated in Fig. 1. To this end, let us introduce the conformal mapping $z(\zeta)$ from an annular region, $r_0<|\zeta|<1$, in the auxiliary complex ζ-plane onto the fluid domain in the complex z-plane, where the unit circle $|\zeta|=1$ is mapped to the plane boundary and the inner circle $|\zeta|=r_0$ is mapped to the cylinder. Furthermore, the points $\zeta=i$ and $\zeta=-i$ are mapped to $z=0$ and $z=\infty$, respectively; see Fig. 2.

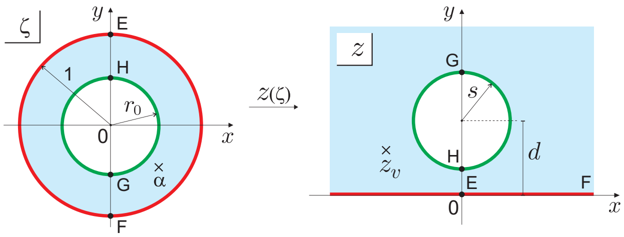

Figure 2: Circular domain in the auxiliary complex ζ-plane (left) and physical domain in the complex z-plane (right).

It is not difficult to see that the function that enacts the desired mapping is given by

$$z(\zeta)=-i\sqrt{d^2-s^2}\left(\frac{\zeta-i}{\zeta+i}\right), \tag{1}$$

whose inverse is

$$\zeta(z)=-i\frac{z-i\sqrt{d^2-s^2}}{z+i\sqrt{d^2-s^2}}. \tag{2}$$

The radius r_0 of the inner circle in the ζ-plane is related to the physical parameters s and d by the following expression:

$$r_0=\frac{1-\sqrt{\frac{d-s}{d+s}}}{1+\sqrt{\frac{d-s}{d+s}}}, \tag{3}$$

as can be easily verified.

Before presenting the complex potential for the problem above, it is instructive to recall [7] that the complex potential for a point vortex of intensity Γ located at position $z=z_v$ (in an unbounded domain) is given by

$$w(z)=\frac{\Gamma}{2\pi i}\log\left(z-z_v\right). \tag{4}$$

Similarly, for a vortex in the presence of a cylinder of radius a, the complex potential can be easily obtained by virtue of the Milne-Thomson circle theorem [8], which yields

$$w(z)=\frac{\Gamma}{2\pi i}\log\left[\frac{z-z_v}{z-a^2/\bar{z}_v}\right]. \tag{5}$$

Here the term in the numerator comes from the contribution to the complex potential from the vortex itself, see Eq. (4); whereas the term in the denominator corresponds to the contribution from the vortex image (inside the cylinder), which is necessary to enforce the boundary condition that the cylinder surface be a streamline of the flow.

For the geometry shown in Fig. 1, where in addition to the cylinder there is an extra boundary (the plane y = 0), the circle theorem is no longer of help, and one has to resort to an alternative approach in order to compute the contribution from the infinite set of vortex images (both inside the cylinder and below the plane). In this case, it is more convenient to compute the complex potential in the auxiliary ζ-plane and then transform it back to the z-plane. Indeed, it can be shown [6, 9] that for a point vortex of unit intensity, located at position $\zeta=\alpha$ in a circular domain in the ζ-plane, the complex potential $w_v(\zeta,\alpha)$ is given by

$$w_v(\zeta,\alpha)=\frac{1}{2\pi i}\log\left[\frac{\omega(\zeta,\alpha)}{|\alpha|\,\omega(\zeta,\frac{1}{\bar{\alpha}})}\right], \tag{6}$$

where $\omega(\zeta,\alpha)$ is the so-called Schottky-Klein prime function, which encodes the geometry of the circular domain.

For the particular geometry shown in Fig. 2, the Schottky-Klein prime function $\omega(\zeta,\alpha)$ can be expressed in a simple form:

$$\omega(\zeta,\alpha)=-\frac{\alpha}{C}P\left(\frac{\zeta}{\alpha},r_0\right), \tag{7}$$

where

$$C=\prod_{n=1}^{\infty}\left(1-r_0^{2n}\right) \tag{8}$$

and

$$P(x,y)=(1-x)\prod_{n=1}^{\infty}\left(1-y^{2n}x\right)\left(1-y^{2n}x^{-1}\right). \tag{9}$$

From the definition of the complex potential $w_v(\zeta,\alpha)$ given in Eqs. (6)-(9), one can verify that it satisfies the appropriate boundary conditions in the ζ-plane, namely, that the unit circle and the inner circle are both streamlines of the flow.

The function $P(x,y)$ given in Eq. (9) is related to the first Jacobi theta function ϑ_1, which appears in the theory of elliptic functions [10]. Indeed, it is possible to derive an expression for the complex potential $w_v(\zeta,\alpha)$ entirely within the framework of elliptic functions. The advantage of the method based on the Schottky-Klein prime function is that it can be rather easily extended to two-dimensional vortex flows around an arbitrary number of obstacles. (This general problem is however beyond the scope of the present work.)

Using the complex potential for a vortex of unit intensity given in Eq. (6), it is possible to obtain the complex potential, $w_U(z)$, due to a uniform stream of velocity U past a cylinder above a plane (with no other flow elements). In this case, it can be shown [11] that the corresponding complex potential, $w_U(\zeta)$, in the ζ-plane is given by

$$w_U(\zeta)=-2\pi Ui\sqrt{d^2-s^2}\left(\frac{\partial w_v}{\partial\bar{\alpha}}-\frac{\partial w_v}{\partial\alpha}\right)\Bigg|_{\alpha=-i}, \tag{10}$$

with w_v as in Eq. (6). Notice that the derivatives in Eq. (10) are evaluated at the point $\alpha = -i$, which is the point that is mapped to infinity by the conformal map $z(\zeta)$, i.e., $z(-i) = \infty$. In the next section we shall use Eqs. (10) and (6) to construct the complex potential for the vortex flow illustrated in Fig. 1.

RESULTS AND DISCUSSION

The complex potential $w(z)$ for the problem of a vortex of intensity Γ placed at position z_v in an uniform stream in the presence of a cylinder and a plane boundary can be obtained by combining Eq. (10) with Eq. (6), multiplied by Γ. This yields

$$w(z) = w_U(\zeta(z)) + \Gamma w_v(\zeta(z), \zeta(z_v)), \tag{11}$$

where $\zeta(z)$ is the inverse mapping given in Eq. (2). As is well known [7], the velocity field $\vec{v} = (u, v)$ can be found by simply taking the derivative of the complex potential:

$$u - iv = \frac{dw}{dz}. \tag{12}$$

This yields a pair of differential equations for $\dot{x} = u(x, y)$ and $\dot{y} = v(x, y)$, which can be numerically integrated to generate the flow streamlines. It is however more convenient to take an alternative approach, namely, perform a contour plot of the stream function $\psi(x, y)$, which can be easily obtained by taking the imaginary part of the complex potential (11). Each level set $\psi(x, y) = c$, with c being a constant, then yields a streamline of the flow. Figure 3 shows the streamline pattern obtained from the contour plot just described for the case when $U = 1$, $\Gamma = -10$, and the vortex is located at $z_v = -1.5 + 0.5i$.

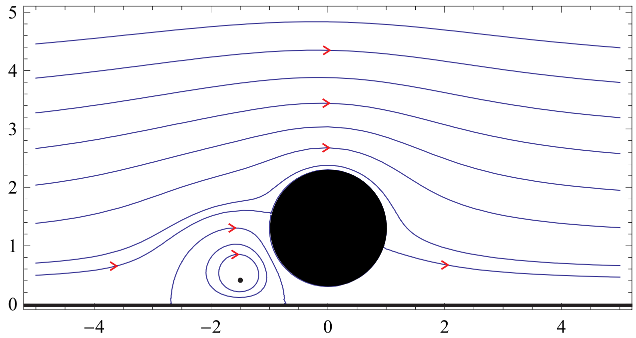

Figure 3: Streamline pattern for the flow studied. The parameters chosen are $\Gamma = -10$, $U = 1$, and $z_v = -1.5 + 0.5i$.

The streamline pattern shown in Fig. 3 displays some interesting features. Of particular interest is the formation of a recirculation zone around the vortex in front of the cylinder. A pattern similar to this was seen in the experiments on flows past a circular cylinder above a plane reported in Ref. [5]. Notice that the recirculation zone acts as an "obstacle" to the oncoming flow, deflecting part of the fluid over the top of the cylinder and thus reducing the flow though the gap. Note also that far above from the cylinder the streamlines tend to be straight lines, meaning that far away from the cylinder one recovers the uniform flow imposed by the uniform stream, as expected.

CONCLUSIONS

We computed the complex potential $w(z)$ for a point vortex in a uniform stream past a circular cylinder placed above a plane wall. From the imaginary part of $w(z)$, we obtained the stream function of the flow whose level sets yield the streamlines. In particular, we presented the streamline pattern for the case when the vortex is placed upstream of the cylinder -a situation that is of interest to the experiments on viscous flows past a cylinder above a plane recently performed by Lin *et al.* [5]. The next step towards a more complete theoretical understanding of the system is to study the vortex dynamics in this geometry, by allowing the vortex to move with the flow velocity (excluding the vortex own contribution) at the vortex position. This analysis is currently in progress.

ACKNOWLEDGMENTS

This work was supported in part by the Brazilian agencies CNPq and FACEPE.

---

[1] B. M. Sumer and J. Fredse, *Hydrodynamics around cylindrical structures* (World Scientific, Singapore, 2006).
[2] L. Föppl, Sitzb. Bayer. Akad. Wiss. **1**, 1 (1913).
[3] S. Tang and N. Aubry, Phys. Fluids **9**, 2550 (1997).
[4] G. L. Vasconcelos, M. N. Moura, and A. M. J. Schakel, Phys. Fluids **23**, 123601 (2011).
[5] W. J. Lin, C. Lin, S. C. Hsieh, and S. Dey, J. Eng. Mech. **135**, 697 (2009).
[6] D. G. Crowdy and J. S. Marshall, Proc. R. Soc. A. **461**, 2477 (2005).
[7] P. G. Saffman, *Vortex Dynamics* (Cambridge University Press, Cambridge, 1992).
[8] L. M. Milne-Thomson, *Theoretical Hydrodynamics* (Dover, New York, 1996).
[9] D. G. Crowdy, Theor. Comput. Fluid Dyn. **24**, 9 (2010).
[10] D. G. Crowdy and J. S. Marshall, Phys. Fluids **17**, 056602 (2005).
[11] M. N. Moura, "Vortex motion around a circular cylinder both in an unbounded domain and near a plane boundary," Master's thesis, Federal University of Pernambuco, 2012.

IMPACT DYNAMICS IN “HARD” AND “SOFT” GRANULAR MATTER

DINÁMICA DE IMPACTO EN MATERIA GRANULAR “DURA” Y “BLANDA”

H. Torres[a ‡], A. González[a ‡], G. Sánchez-Colina[a,b], J. C. Drake[a,b] and E. Altshuler[a †]

a) “Henri Poincarè” Group of Complex Systems, Physics Faculty, University of Havana, 10400 Havana, Cuba, ealtshuler@fisica.uh.cu†
b) General Physics Department, Physics Faculty, University of Havana, 10400 Havana, Cuba
‡ contributed equally as first authors.
† corresponding author

Using a wireless accelerometer, we explore the dynamics of penetration of a sphere falling into very light granular matter prepared with different compactions. The duration of the penetration process until the sphere stops is ~30% bigger for less compacted granular matter, while the maximum penetration depth is ~40% bigger in that case. These outputs are quite remarkable, considering that the differences in the filling factors of the two granular media were smaller than 5%.

Utilizando un acelerómetro inalámbrico, exploramos la dinámica de penetración de una esfera que cae sobre material granular muy ligero, preparado con dos compactaciones diferentes. La duración del proceso de penetración hasta que la esfera se detiene es un ~30% mayor para el medio menos compacto, mientras que la penetración máxima para ese medio es un ~40% mayor. Estos resultados son notables, considerando que la diferencia entre ambos factores de llenado es menor del 5%.

PACS: Granular materials rheology, 83.80.Fg; compaction, granular systems, 45.70.Cc; granular materials, 81.05.Rm

INTRODUCTION

Crater formation by impact in granular matter has been a subject of intense research in the last decade [1-7]. There is still debate about the form of the force law against penetration of the impactor, and how it depends on different experimental parameters, such as the density of the impacting object and the granular matter, the impact speed, the roughness and shape of the impactor, etc. Many of the existing reports concentrate in the study of the maximum penetration depth of the impacting object, and the diameter of the resulting crater. “Dynamical” studies, on the other hand, typically record the vertical position of the impactor during the penetration process [5], and only very few record *directly* its acceleration [6, 7].

In this paper, we use a wireless accelerometer to directly measure the acceleration of a sphere falling into extremely light granular matter, in order to find out how the penetration dynamics depend on the level of compaction of the granular medium.

EXPERIMENT

A cylindrical container of 30 *cm* diameter and 26 *cm* depth was filled with expanded polyestirene particles of density 0.014 ± 0.002 *g*/*cc* and diameter distributed between 2.0 and 6.5 *mm*, peaking at 5.8 *mm* [7]. Near the bottom of the container there was a fine horizontal mesh that allowed air to flow upwards injected by a compressor through a hole at the bottom of the system without loosing any granular material. This setup allowed us to prepare two types of granular matter:

Soft granular matter (SGM): Air was injected from the bottom from zero flow to a maximum, and then decreased back to zero flow (the maximum flow was selected in such a way that it produced visible “turbulence” at the free surface of the grains). The resulting granular medium, had a volume fraction of 0.64 ± 0.01. Using a rotating drum, we found that the maximum angle of stability for SGM was $29.52^o \pm 0.25^o$.

Hard granular matter (HGM): First, SGM was obtained. Then, the container was shaken horizontally for 5 seconds (the oscillations were approximately sinusoidal, with a period of 0.225 ± 0.004 *s* and acceleration amplitude of 1.9 ± 0.3 m/s^2). The resulting volume fraction was of 0.68 ± 0.01, and the maximum angle of stability was $30.29^o \pm 0.50^o$.

The impactor consisted in a 3-axis wireless accelerometer mounted into a 4-*cm* diameter ping-pong ball, in such a way that the *z*-axis of the accelerometer was pointing downwards along the vertical direction. The impactor weighted 23 grams (the lower hemisphere was more massive than the upper to guarantee minimal tilting when traveling through the granular media). The accelerometer had a resolution of 0.0001 *g*, and was able to transmit data in real time at 2.4 *GHz* to a USB node on an external PC, at a data point rate of 120 *Hz* [8].

A small magnet was glued to the top of the ping-pong ball, so the impactor could be "magnetically hanged", through a fixed, thin horizontal plastic plate, from the lower end of a vertical iron rod that initially touched the upper face of the fixed plate. When the rod was lifted up using a computer-controlled electro-mechanical device, the impactor was dropped onto the granular system with very small lateral tilting. The impactor was always released from a height where its lower end was just "touching" the free granular surface.

In the experiment, the vertical acceleration of the impactor was recorded in real time during its penetration into the granular medium (its horizontal acceleration was negligible compared to that along *z*).

RESULTS AND DISCUSSION

Fig. 1 shows the evolution of the vertical acceleration, velocity and position of the sphere as it penetrates the granular matter for HGM (left column) and SGM (right column). Velocity and position graphs were obtained after one and two integrations, respectively, of the acceleration vs. time graph -i.e., the direct output from the accelerometer. The insets have been constructed by plotting the acceleration vs. the calculated position. The positive direction is taken downwards.

Let us examine Figs 1 (a) and (d), as time increases. Initially, $a = 0$, which indicates that the impactor is hanging from the release system. The release process takes less than 70 *ms* both for HGM and SGM, and occurs before the impactor has dropped to a depth of 0.5 *cm* (as suggested by the insets). Then, the downward acceleration increases to average maximum values of 8 ± 1 m/s^2 for HGM and 9 ± 1 m/s^2 for SGM (ideally it should reach 9,8 m/s^2, but the ball is touching the granular surface before being released). After that, *a* increases in the upwards direction due to the action of granular resistance, reaching average minima of 8 ± 1 m/s^2 for HGM and 9 ± 1 m/s^2 SGM respectively. Finally, zero acceleration is reached, meaning that the sphere has stopped moving (in the case of SGM, $a = 0$ only after a few damped oscillations). The final stage of the stopping process occurs sharply within a few-*mm* distance. A major difference between the two media is the duration of the whole process from release to stop: 340 ± 10 *ms* for HDM, and 470 ± 20 *ms* for SGM.

Figs 1 (b) and (e) show the velocity records resulting from integrating in time the acceleration. In both cases, velocity starts at zero, and reaches maxima of 0.7 ± 0.1 *m*/*s* and 1.0 ± 0.1 *m*/*s* for HGM and SGM, respectively. Then, it goes back to zero quite symmetrically in time.

Figs 1 (c) and (f) show the *z*-position resulting from the integration of the velocity records. In the case of HGM, the depth inside the granular matter goes from zero (at the surface) to 0.14 ± 0.01 *m* (approximately in the middle of the granular column). In the case of the SGM, the final depth gives 0,22 ± 0,01 *m* (we checked both values using a thin thread attached to the sphere). Notice that, in the latter case, the ball stops only 4 *cm* from the bottom of the bucket. The damped oscillations of the acceleration at the end of the penetration process may be related to a jammed (more compacted) section of the granular material produced by the impactor itself immediately under it, which acts as a "solid wall". The process is probably enhanced by the proximity of the bottom wall in the case of SGM.

All in all, we have shown that, when a granular system is compacted in such a way that the filling factor decreases just to 94% of its original value, the total penetration time can be reduced to a 70%, the maximum velocity of the impactor can decreased to a 70%, and its maximum penetration depth can be reduced to a 60% of its initial value.

It has been shown before that the equation of motion for penetration of a spherical intruder into a larger system analogous to our SGM can be written as [7]

$$m\frac{d^2z}{dt^2} = mg - \eta\left(\frac{dz}{dt}\right)^2 - \kappa\lambda\left(1 - e^{-\frac{z}{\lambda}}\right), \tag{1}$$

where *m* and *z* are the mass of the sphere and the penetration depth from the free surface, respectively, λ is a characteristic length of the order of the diameter of the container, and the coefficients η and κ characterize the inertial drag, and a depth-dependent friction, respectively. This equation follows well most of the motion [7], but it cannot describe the release process at the very beginning and the final stopping stage (where the acceleration goes suddenly to zero when the ball stops in the bulk of the granular system).

In order to estimate parameters, we use two expressions associated to the motion far from its ends. From (1), it is not difficult to see that

$$\kappa = m\left|s_{a\to 0}\right| e^{z_{a\to 0}/\lambda}, \tag{2}$$

where $s_{a\to 0}$ and $z_{a\to 0}$ are the slope of the *a* vs. *z* graph (see insets), and the depth of the impactor when the acceleration approaches zero, respectively. Assuming $\lambda \sim 0.3$ *m* the resulting values for HGM and SGM cannot be clearly differentiated, and give a value of $\kappa = 1.9 \pm 0.3$ kg/s^2, which is near the value reported in [7] for a 6-*m* long cylinder with SGM. Additionally,

$$\eta = \frac{1}{v_{\max}^2}\left[mg - \kappa\lambda\left(1 - e^{-z_{v_{\max}}/\lambda}\right)\right], \tag{3}$$

where $v_{\max}$ is the maximum speed of the impactor during penetration, and $z_{\max}$ is the depth at which the ball experiences that speed. Equation (3) gives η_{HGM} = 0.16 ± 0.02 *kg*/*m* for HGM and η_{SGM} = 0.05 ± 0.02 *kg*/*m* for SGM. The latter value is close to that estimated in [7].

CONCLUSION

We have shown that, when a granular system is compacted, a small increase in compaction produces an increase in the penetration time, a decrease in the total penetration depth, and a sizable increase in the inertial drag coefficient.

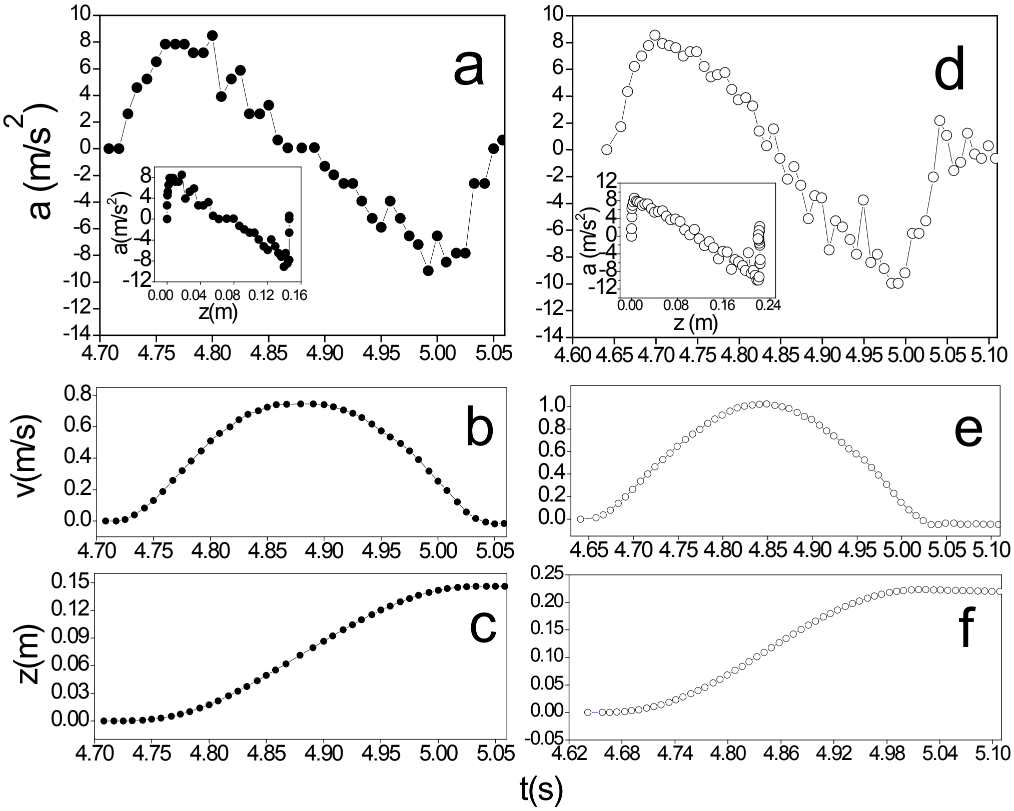

Figure 1: Experimental results. (a) - (c) Vertical acceleration, velocity and position of the impactor vs. time graphs, respectively, for Hard Granular Matter (inset is Acceleration vs. position). (d) - (f) Analogous graphs for Soft Granular Matter. Positive reference points downward.

ACKNOWLEDGEMENTS

We acknowledge C. Pérez-Penichet for contributing to the electronics, O. Ramos and J. Wu for support in the experimental setup, and A. Batista-Leyva, L. Kadanoff and S. Waitukaitis for useful discussions.

---

[1] J. S. Uehara, M. A. Ambroso, R. P. Ohja and D. J. Durian, Phys. Rev. Lett. **90**, 194301 (2003).

[2] A. M. Walsh, K. E. Holloway, P. Habdas and J. R. de Bruyn, Phys. Rev. Lett. **91**, 104301 (2003).

[3] S. J. de Vet and J. R. de Bruyn, Phys. Rev. E. **76**, 041306 (2007).

[4] J. F. Boudet, Y. Amarouchene, and H. Kellay, Phys. Rev. Lett. **96**, 158001 (2006).

[5] H. Katsuragi and D. Durian, Nat. Phys. **3**, 420 (2007).

[6] D. I. Goldman and P. Umbanhowar, Phys Rev. E **77**, 021308 (2008).

[7] F. Pacheco-Vázquez, G. A. Caballero-Robledo, J. M. Solano-Altamirano, E. Altshuler, A. J. Batista-Leyva and J. C. Ruiz-Suárez, Phys. Rev. Lett. **106**, 218001 (2011).

[8] See MMA7660FC ZSTAR3 accelerometer details at www.freescale.com/zstar

[9] T. Brzinski and D. J. Durian, Soft Matter **6**, 3038 (2011).

[10] D. J. Constantino, J. Bartell, K. Scheidler and P. Schiffer, Phys. Rev. E **83**, 0011305 (2011).

TSALLIS FORMALISM IN RADIOBIOLOGY

EL FORMALISMO DE TSALLIS EN LA RADIOBIOLOGÍA

O. Sotolongo-Costa[a †] and O. Sotolongo-Grau[b ‡]

a) "Henri Poincarè" Group of Complex Systems, Physics Faculty, University of Havana, 10400 Havana, Cuba, osotolongo@fisica.uh.cu[†]
b) Departamento de Física-Matemática y Fluidos, UNED, Madrid, osotolongo@dfmf.uned.es[‡]
†, ‡ corresponding authors

We describe how Tsallis' formalism can be applied to the cell survival factor of cells under radiation. Some universal characteristics become revealed with this treatment. This viewpoint has potential applications in clinical radiotherapy.

Describimos cómo el formalismo de Tsallis puede ser aplicado al estudio del factor de supervivencia de células sometidas a radiación. Este tratamiento revela algunas características universales del proceso, y posee aplicaciones potenciales en radioterapia clínica.

PACS: Cell processes, 87.17.-d; dosimetry/exposure assessment of ionizing radiations, 87.53.Bn; radiations effects on biological systems, 87.50.-a.

INTRODUCTION

Radiobiologists have developed some empirical models describing the interaction between radiation and living tissues (see [1] for a review of radiobiology models) capable of finding the survival fraction, F_s, of cells under a radiation dose, D.

Their applicability limits are not clear, so multiple corrections have been developed in order to fit the experimental data. Usually expressed as E=-ln(F_s), the tissue effect gathers together several models of interaction between cells and ionizing radiation. In the linear model, tissue effect is considered linear to the radiation dose, $E = \alpha D$, and the survival fraction, F_s = exp(-αD), is the cumulative survival probability of a cell under any dose D. So, the probability fulfills the additive property, so $F_s[D_1 + D_2] = F_s[D_1] + F_s[D_2]$. However, this model only fits the experimental data for some tissues under low radiation doses [1], so the tissue effect must be corrected to $E = \alpha D + \beta D^2$, called the linear quadratic (LQ) model. But then the survival fraction loses the additive property. Then, the superposition principle is not fulfilled. However, any model of interaction between radiation and living tissues must allow dividing a continuous radiation in finite intervals and the resultant tissue effect must be the same. Indeed, assuming that the dose is additive, the tissue effect is not the sum of the effects for different doses. This suggests that the radiobiological problem must be approached from a non extensive formulation [2]. Here, a general expression for survival fraction is found using the Tsallis entropy [3] definition, and assuming the existence of a critical dose that kills every single cell. This survival fraction expression fits the experimental data even where previous empirical models fail. Using the q-algebra [4, 5] a new expression to find the survival fraction of a whole treatment is shown.

TSALLIS APPROACH TO RADIOBIOLOGY

To apply the maximum entropy principle in the Tsallis version to the problem of finding the survival fraction of a living tissue [6] that receives a radiation, we postulate the existence of some amount of absorbed radiation D_0 (or its equivalent "minimal annihilation effect", $E_0 = \alpha_0 D_0$) after which no cell survives. The application of the maximum entropy principle performs like the usual one but with a few modifications.

The Tsallis entropy is

$$S_q = \frac{1}{q-1}\left(1 - \int_0^{E_0} p^q(E)\, dE\right). \qquad (1)$$

The normalization condition is $\int_0^{E_0} p(E)\, dE = 1,$ and the q-mean value becomes $\int_0^{E_0} E\, p^q(E)\, dE = \langle E \rangle_q < \infty.$

With this definition, all properties of the tissue and its interaction with radiation become included in $\langle E \rangle_q$ and therefore in E_0.

To calculate the maximum of (1) under the above conditions the well known method of Lagrange multipliers [5] is applied, resulting in

$$F_s(D) = \begin{cases} \left(1 - \frac{D}{D_0}\right)^{\gamma} & D < D_0 \\ 0 & D > D_0 \end{cases} \qquad (2)$$

where we introduced $E = \alpha_0 D, \gamma = \frac{2-q}{1-q}, D_0 = \frac{E_0}{\alpha_0}$. Finally, the LQ model is easily recovered from (2) in the limit $q \to 1$ up to order two in a Taylor series expansion [7, 8].

All the information about the kind of radiation, radiation rate, etc is contained in the phenomenological term D_0, whereas tissues are characterized by γ. The exponent γ in this case, as in phase transitions, determines the universality class.

Tsallis based survival fraction properties. The linear model for the tissue effect [1] implies that if the dose is additive the corresponding survival fraction is multiplicative. It is worth to find a link between the additive property of the dose and the probabilistic properties of the cell survival fraction. Let us use the function: $\exp_\gamma(x) = \left(1+\frac{x}{\gamma}\right)^\gamma$ and its inverse function: $\ln_\gamma(\exp_\gamma(x)) = x.$ Then, let us introduce the γ-product of two numbers x and y as

$$x \otimes y = \exp_\gamma\left[\ln_\gamma(x) + \ln_\gamma(y)\right] = \left[x^{\frac{1}{\gamma}} + y^{\frac{1}{\gamma}} - 1\right]^\gamma. \qquad (3)$$

Note that these definitions are not essentially different from the q-exponential and q-logarithm presented in [4]. We are just introducing these definitions to simplify the calculations. Let us now define the "generalized tissue effect" $E = -\frac{E_0}{\gamma}\ln_\gamma(F_s).$ We demand this effect to satisfy the additive property. Then the survival fraction, expressed as

$$F_s = \exp_\gamma\left(-\gamma\frac{D}{D_0}\right), \qquad (4)$$

becomes γ-multiplicative. This implies that the statistical independence of the survival fractions is only possible when $\gamma \to \infty$ ($q \to 1$).

The survival fraction for the sum of the effects after N doses becomes

$$F_s(N,D) = \left[1 - \sum_{i=1}^{N}\frac{D_i}{D_0}\right]^\gamma = \bigotimes_{i=1}^{N} F_s(D_i), \qquad (5)$$

where $\bigotimes_{i=1}^{N}$ denotes the iterated application of the γ-product. On the other hand, if the survival probabilities are independent the effect is not additive and the sum must be redefined as $x \oplus y = x + y - \frac{xy}{\gamma}$. Hence, the total survival fraction is

$$F_s(N,D) = \left[1 - \bigoplus_{i=1}^{N}\frac{D_i}{D_0}\right]^\gamma = \prod_{i=1}^{N} F_s(D_i), \qquad (6)$$

where $\bigoplus_{i=1}^{N}$ denotes the iterated application of the γ-sum.

This equation leads to new insights, as we shall point.

CONSEQUENCES

This model has shown a remarkable agreement with experimental data [7], even in those limits where previous models are less accurate, mainly at high doses. The analysis of the model also provides new hints about the tissue response to radiation: first, the interaction of a tissue with the radiation is universal and characterized by a single exponent (not dependent on the radiation exposure); second, the model includes a cutoff radiation dose above which every single cell dies. Furthermore, previous models can be obtained as particular limiting cases. Besides, as for those models, its mathematical expression is simple and can be easily plotted and interpreted.

Furthermore the model was derived for radiobiological survival fraction but its applicability could be extended to other processes. Indeed, every irreversible phenomena where the individual entities can get a terminal state and that fulfils the conditions: (i) can be described with Tsallis entropy [8], (ii) keeps the maximum entropy principle, (iii) a critical cutoff exists in such a way that no alive entity remains after it, must follow (2).

In particular this could be applied to some biological interactions or clinical treatments as antibiotics or other killer drugs.

Nevertheless the expression (2), understood as survival probability, lacks the extensively property. In other words, for n events following (2) the total survival probability should be found as a composition of the survival probabilities of the successive events. However, there is no straightforward composition rule for those probabilities.

Indeed, a new view introduced by Eq. (6) is that if two doses, X_A and X_B are applied, the resulting probability from their composition has two possible values. If the dose is assumed as additive, $F_{AB} = (1 - D_A - D_B)^\gamma$ (here D is expressed in units of D_0 to simplify), the individual probabilities under the A and B events could not be treated as independent probabilities, $F_{AB} \neq F_A F_B$. On the other hand, if probabilities are multiplicative, $F_{AB} = (1 - D_A)^\gamma (1 - D_B)^\gamma$, doses do not fulfil the superposition principle for the equivalent physical dose, $X_{AB} \neq X_A + X_B$.

In other words, Eq. (6) has revealed, in a formal framework, *the relativity of the applied dose*. This is intuitively known in clinical practice (i.e. doses have not the same effect if continuously applied or splitted in time), but here we have provided a formal basis for this fact, that not only has conceptual importance, but also practical applications, particularly in the isoeffect problem. Results on this issue will be published later.

CONCLUSIONS

A new theoretical expression for the survival fraction of cells under radiation has been found, using the Tsallis formulation of entropy. The existence of a critical value for the absorbed radiation dose under which no entities survive is introduced in the formulation in order to get a proper expression. The new expression depends of two coefficients that characterize the tissue behavior under radiation (γ) and the specific conditions in which the radiation is applied (D_0). Here, the relation between the additivity of the dose and the survival probability has been revealed and conceptualized.

[1] M Tubiana, *Introduction to Radiobiology*, (Taylor & Francis, London, 1990).
[2] C. Tsallis, Braz. J. Phys. **29**, 1 (1999).
[3] E. M. F. Curado and C. Tsallis, J. Phys. A: Math. Gen. **24**, L69 (1991).
[4] C. Tsallis, *Introduction to nonextensive statistical mechanics*, (Springer, New York, 2009).
[5] A. Plastino and A. R. Plastino, Braz. J. Phys. **29**, 50 (1999).
[6] G. G. Steel, in *Basic Clinical Radiobiology for Radiation Oncologists*, edited by G. G. Steel (Edward Arnold Publishers, London, 1993).
[7] O. Sotolongo-Grau, D. Rodríguez-Pérez, J. C. Antoranz and O. Sotolongo-Costa. Phys. Rev. Lett. **105**, 158105 (2010).
[8] O. Sotolongo-Grau, D. Rodríguez-Pérez, J. C. Antoranz and O. Sotolongo-Costa, in *Bayesian inference and maximum entropy methods in science and engineering*, edited by A. Mohammad-Djafari, J. -F. Bercher and P. Bessiere (AIP Conference Proceedings **1305**, 219 (2010)).

Rev. Cub. Fis. **29**, 1E51 (2012)

MULTICANONICAL DISTRIBUTION AND THE ORIGIN OF POWER LAWS

LA DISTRIBUCIÓN MULTICANÓNICA Y EL ORIGEN DE LAS LEYES DE POTENCIA

G. L. Vasconcelos[a †] and D. S. P. Salazar[b]

a) Departamento de Física, Universidade Federal de Pernambuco, Brazil, giovani@df.ufpe.br†
b) Unidade de Educação a Distância e Tecnologia, Universidade Federal Rural de Pernambuco, Brazil
† corresponding author

A multicanonical formalism is applied to the problem of statistical equilibrium in a complex system with a hierarchy of dynamical structures. At the small scales the system is in quasi-equilibrium and follows a Maxwell-Boltzmann distribution with a slowly fluctuating temperature. The probability distribution for the temperature is determined using Bayesian analysis and it is then used to average the Maxwell-Boltzmann distribution. The resulting energy distribution law is written in terms of generalized hypergeometric functions, which display power-law tails.

Un formalismo multicanónico es aplicado al problema del equilibrio estadístico en un sistema complejo con una jerarquía de estructuras dinámicas. A escalas pequeñas el sistema está en cuasi-equilibrio y sigue una distribución de Maxwell-Boltzmann con una temperatura fluctuante. La distribución de probabilidades de la temperatura se determina utilizando el análisis bayesiano y luego esta es usada para promediar la distribución de Maxwell-Boltzmann. La ley de distribución de energía resultante se escribe en términos de funciones hipergeométricas generalizadas, que muestran una cola tipo ley de potencia.

PACS: Complex systems, 89.75.-k; classical ensemble theory, 05.20.Gg; distribution theory, 02.50.Ng

INTRODUCTION

Power law distributions occur in widely diverse physical systems spanning an impressive range of length scales [1]. The appearance of heavy-tailed distributions is often traced to the presence of hierarchical structures in the system [2], whose complex "interaction" may result in violation of the statistical independence of subsystems, thus leading to non-Gibbsian distributions [3]. Despite these insights and the many contributions to the problem [4], it is fair to say that the physical mechanisms behind the emergence of power-law distributions are not yet well understood.

Recently, we introduced [6] a general formalism to describe statistical equilibrium of complex systems with multiple scales where the probability distribution of states displays power-law tails. In this formalism, the hierarchical structure embedding the system of interest is effectively modeled as a set of nested "internal heat reservoirs," where each "reservoir" is described by only one effective degree of freedom, namely, its "temperature." On the basis of a few physically reasonable assumptions, it was possible to show that for a large class of systems the equilibrium distribution can be written explicitly in terms of certain generalized hypergeometric functions, which exhibit power law tails. This family of generalized hypergeometric (GHG) distributions includes, as its first two members, the Boltzmann-Gibbs distribution and the Tsallis distribution [7]. Higher-order members of the GHG family of distributions have been shown to describe remarkably well the statistics of velocity fluctuations in turbulence [5].

The GHG distribution represents a generalization of the canonical distribution for multiscale systems and hence it is also called multicanonical. The main purpose of the present paper is to give an alternative derivation, based on Bayesian analysis, of the multicanonical distribution. Because the derivation of the multicanonical distribution given here tries to parallel (whenever possible) the usual treatment of the canonical distribution, we shall begin our presentation by briefly reviewing the derivation of the canonical distribution.

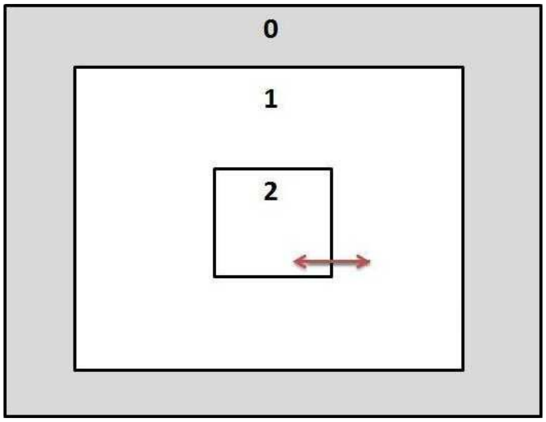

Figure 1: A canonical system in thermal equilibrium at temperature T_0. Arrows indicate energy exchange between the subsystems.

THE CANONICAL DISTRIBUTION

Consider a system in thermal equilibrium at some temperature T_0. We recall that in the canonical formalism the constant temperature constraint is enforced by embedding the system is a much larger system (i.e., a heat bath) capable of giving it energy [8]. We designate the system of interest by the label 2 and the larger system embedding it by the label 1, with the combined system formed by subsystems 1 and 2 being given the label 0; see Fig. 1.

The energies of systems 1 and 2 will be denoted by E_k^1 and E_i^2, respectively, where i and k represent the labels designating the possible states in each system. Let us denote by $p_0(E_{k,i}) = p_0(E_k^1 + E_i^2)$ the probability of finding system 0 in a state corresponding to energy $E_{k,i} = E_k^1 + E_i^2$. In view of the independence between systems 1 and 2, one can then write

$$p_0(E_k + E_i) = p_1(E_k)p_2(E_i), \tag{1}$$

where $p_1(E_k)$ and $p_2(E_i)$ are the probabilities of finding systems 1 and 2 in states with energy E_k and E_i, respectively. Taking the logarithm derivative of (1) with respect to E_k yields

$$\frac{\partial \ln p_0(E_i + E_k)}{\partial E_k} = \frac{d \ln p_1(E_k)}{dE_k} \equiv -\beta_1, \tag{2}$$

where β_1 may be a function of E_k but not of E_i. On the other hand, it is clear that

$$\frac{\partial \ln p_0}{\partial E_k} = \frac{\partial \ln p_0}{\partial E_i} = \frac{d \ln p_2(E_i)}{dE_i}. \tag{3}$$

Comparing (2) and (3), one then concludes that

$$\frac{d \ln p_2(E_i)}{dE_i} = -\beta_1. \tag{4}$$

Since β_1 does not depend on E_i, the preceding equation can be readily integrated, yielding

$$p_2(E_i \,|\, \beta_1) = constant \cdot \exp(-\beta_1 E_i). \tag{5}$$

Since the partition of system 0 into subsystems 1 and 2 is entirely arbitrary, the quantity β_1 must be the same for any partition one chooses. In other words, β_1 is a characteristic of system 0 only, that is,

$$\beta_1 = \beta_0, \tag{6}$$

which implies that

$$p_2(E_i \,|\, \beta_0) = A\exp(-\beta_0 E_i), \tag{7}$$

where A is a constant.

It should be evident that the discussion above is completely symmetrical with respect to labels 1 and 2, so that system 2 (irrespective of its size) obeys the same distribution law as system 1. In then follows from (1) and (7) that the probability of finding any subsystem of system 0 in a state with energy E is given by the Boltzmann-Gibbs (BG) distribution:

$$p(E \,|\, \beta_0) = \frac{g(E)\exp(-\beta_0 E)}{Z_0(\beta_0)}, \tag{8}$$

where $g(E)$ is the density of states and

$$Z_0(\beta) = \int_0^\infty g(E)\exp(-\beta E)dE \tag{9}$$

is the partition function.

It is important to emphasize here that the key step in deriving (8) was the ability to partition the system into two independent subsystems of arbitrary sizes, so that each subsystem is described by the same distribution law. There are however many physical systems, where the relevant probability distributions depend on the scale at which the measurements are made. In such complex systems, the system cannot be partitioned into independent subsystems of arbitrary sizes, and one has to treat each dynamical scale separately, as discussed next.

THE MULTICANONICAL DISTRIBUTION

Here we consider a multiscale system of size L in thermal equilibrium at temperature T_0. We assume that the system possesses a hierarchy of dynamical structures of characteristic sizes $\ell_i = L/b^{i-1}$, with $i = 1, 2, ..., n$, where b is a number greater than 1. (The specific value of b is not relevant here.) We suppose furthermore that there is a wide separation of time scales within this hierarchy with smaller structures having shorter characteristic times. Let us now consider a partition of our system into "nested" subsystems of sizes ℓ_j, as indicated in Fig. 2. We shall designate the subsystem of size ℓ_j by the label j. The "thermodynamic state" of each subsystem j will be characterized by only one parameter, namely, its inverse temperature β_j. As before, we designate the combined system consisting of all subsystems by the label 0.

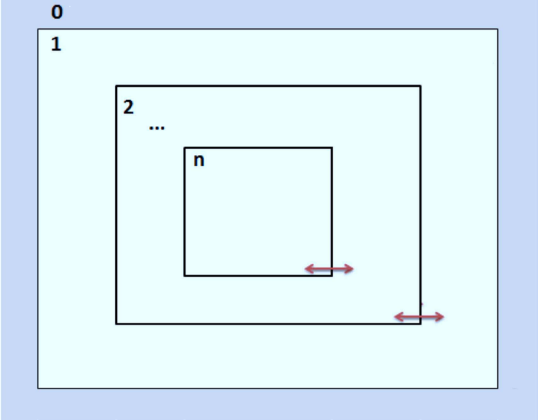

Figure 2: A multicanonical system in thermal equilibrium at temperature T_0.

Let us now focus our attention on the subsystem n of size ℓ_n. Since ℓ_n is the smallest characteristic length scale in the system, it is clear that this subsystem can be arbitrarily divided into two independent subsystems. Thus, repeating the same reasoning that led to Eq. (8), one obtains that the energy distribution law for this subsystem is given by

$$p(E\,|\,\beta_n) = \frac{g(E)\exp(-\beta_n E)}{Z_0(\beta_n)}. \tag{10}$$

Note, however, that owing to the (intermittent) energy exchange between subsystem n and its immediate surrounding, represented by subsystem $n - 1$, the parameter β_n is no longer constant but rather will fluctuate randomly. If we denote by $f(\beta_n)$ the probability density function (PDF) of β_n, then the marginal distribution $p(E)$ for subsystem n reads

$$p(E) = g(E)\int_0^\infty \frac{\exp(-\beta_n E)}{Z_0(\beta_n)} f(\beta_n)\, d\beta_n. \tag{11}$$

Next we wish to compute $f(\beta_n)$. To do so, we shall make use of Bayesian analysis [9]. First recall that subsystem n is embedded in a much larger subsystem $n - 1$, characterized by the parameter β_{n-1}, which is assumed to vary much slower than β_n. We are thus interested in computing $f(\beta_n|\beta_{n-1})$. From Bayes' theorem [9] one has

$$f(\beta_n;\beta_{n-1}\,|\,E) \propto p(E\,|\,\beta_n) f(\beta_n;\beta_{n-1}), \tag{12}$$

where β_{n-1} is considered a (hyper)parameter of the distribution of β_n. In Bayesian parlance, the distribution $f(\beta_n;\beta_{n-1})$ is called the prior distribution, $p(E|\beta_n)$ is the likelihood function, and $f(\beta_n;\beta_{n-1}|E)$ is the posterior distribution. [In Eq. (12) we introduced the notation $f(\beta_n;\beta_{n-1}) \equiv f(\beta_n|\beta_{n-1})$ for convenience.]

Let us assume, as is often done in Bayesian analysis, that the prior distribution is conjugate to the likelihood $p(E|\beta_n)$, meaning that the posterior distribution follows the same parametric form as the prior distribution. If we consider the rather general case where $g(E) \propto E^{\gamma-1}$, $\gamma > 0$, so that $Z_0(\beta_n) \propto \beta_n^{-\gamma}$, it then follows from Eq. (8) that $p(E|\beta_n)$ is given by

$$p(E\,|\,\beta_n) \propto \beta_n^\gamma E^{\gamma-1}\exp(-\beta_n E), \tag{13}$$

which when viewed as the likelihood of the parameter β_n is proportional to a gamma distribution. Now, it is well known [9] that in this case the conjugate prior is also a gamma distribution, and so we have

$$f(\beta_n\,|\,\beta_{n-1}) = \frac{1}{\beta_n\Gamma(\alpha+1)}\left(\frac{\alpha\beta_n}{\beta_{n-1}}\right)^{\alpha+1}\exp\left(-\frac{\alpha\beta_n}{\beta_{n-1}}\right), \tag{14}$$

where α is a constant. In obtaining Eq. (14) we also used the fact that $\langle\beta_n\,|\,\beta_{n-1}\rangle = \beta_{n-1}$, as it should, since subsystem $n - 1$ acts as a heat reservoir for subsystem n. By scale invariance, we assume that the distribution $f(\beta_j|\beta_{j-1})$, for $j = 1, \ldots, n$, has the same form as in Eq. (14).

We now have

$$f(\beta_n) = \int_0^\infty f(\beta_n\,|\,\beta_{n-1}) f(\beta_{n-1})\, d\beta_{n-1}. \tag{15}$$

Using this relation recursively then yields

$$f(\beta_n) = \int_0^\infty\cdots\int_0^\infty \prod_{j=1}^n f(\beta_j\,|\,\beta_{j-1})\, d\beta_1\cdots d\beta_{n-1}, \tag{16}$$

with $f(\beta_j|\beta_{j-1})$ given by Eq. (14). After inserting Eq. (16) into Eq. (11), and performing a sequence of changes of variables of the type $x_j = \alpha_j\,\beta_j/\beta_{j-1}$, one can show that the resulting multidimensional integral can be expressed in terms of known higher transcendental functions:

$$p(E) = \frac{g(E)}{Z_n}\, {}_nF_0(\alpha+\gamma+1,\ldots,\alpha+\gamma+1;-\beta_0\alpha^{-n}E), \tag{17}$$

where ${}_nF_0(\alpha_1, \ldots, \alpha_n; -z)$ is the generalized hypergeometric function of order $(n, 0)$ [10]. The small-scale partition function, Z_n, is given by

$$Z_n = Z_0(\beta_0)\left[\frac{\alpha^\gamma\Gamma(\alpha+1)}{\Gamma(\alpha+\gamma+1)}\right]^n. \tag{18}$$

One important property of the generalized hypergeometric (GHG) distribution given in (17) is that it exhibits power-law tails of the form: $p(E) \propto E^{-(\alpha+2)}$, for E → ∞. This follows immediately from the asymptotic expansion of the function ${}_nF_0$ [11]: ${}_nF_0(\alpha_1, \ldots, \alpha_n; -x) = \Sigma_{i=1}^n C_i x^{-\alpha_n}(1+O(1/x))$, as $x \to \infty$. It is also worth pointing out that the first two members of the family ${}_nF_0$ yield elementary functions, namely, ${}_0F_0(x) = \exp(x)$ and ${}_1F_0(1/(q-1), x) = \exp_q(x/(q-1))$, where $\exp_q(x)$ is the q-exponential: $\exp_q(x) = [1 + (1-q)x]^{1/(1-q)}$. The GHG distribution with $n = 0$ thus recovers the Boltzmann-Gibbs distribution, whereas for $n = 1$ it gives the q-exponential or Tsallis distribution [7]. One then sees from the preceding discussion that if a system with only one time scale is in thermal equilibrium then the Boltzmann-Gibbs distribution follows, whereas if it has two distinct time scales the Tsallis distribution should be applicable. For complex systems with more than two characteristic time scales, such as turbulent flows, GHG distributions of higher order are thus required [5, 6].

CONCLUSIONS

We have presented an alternative derivation, based on Bayesian analysis, of the multicanonical distribution, which describes the statistical equilibrium of complex systems possessing a hierarchy of time and length scales. We have shown that the multicanonical distribution can be written explicitly in terms of generalized hypergeometric functions, which exhibit a power-law asymptotic behavior. This thus shows that the emergence of power law distributions —an ubiquitous feature in nature— is intimately connected with the existence of multiple time and length scales in the system.

ACKNOWLEDGEMENTS

This work was supported in part by the Brazilian agencies CNPq and FACEPE

[1] A. Clauset, C. R. Shalizi and M. E. J. Newman, SIAM Review **51**, 661 (2009).

[2] E. Alvarez-Lacalle, B. Dorow, J. -P. Eckmann and E. Moses, Proc. Natl. Acad. Sci. USA **103**, 7956 (2006).

[3] R. A. Treumann and C. H. Jaroschek, Phys. Rev. Lett. **100**, 155005 (2008).

[4] An extensive bibliography on power-law distributions can be found in http://www.nslij-genetics.org/wli/zipf.

[5] D. S. P. Salazar, and G. L. Vasconcelos, Phys. Rev. E **82**, 047301(2010).

[6] D. S. P. Salazar, and G. L. Vasconcelos, submitted to Phys. Rev. Lett. (2012).

[7] C. Tsallis, J. Stat. Phys. **52**, 479 (1988).

[8] G. H. Wannier, *Statistical Physics* (Dover, New York,1966)

[9] A. Gelman, J. B. Carlin, H. S. Stern and D. Rubin, *Bayesian Data Analysis*, 2nd ed. (Chapman and Hall, London, 2003).

[10] A. Erdélyi, W. Magnus, F. Oberhettinger and F. G. Tricomi, *Higher Transcendental Functions,* (McGraw-Hill, New York, 1953).

[11] See, e.g., http://functions.wolfram.com/07.31.06.0041.01

A PENTABLOCK POLYMER FORMING CORE-SHELL STRUCTURES

POLÍMEROS PENTABLOQUES QUE FORMAN ESTRUCTURAS "CORE-SHELL"

K. D. Knudsen[a †], N. Beheshti[b], K. Zhu[b], A. -L. Kjoniksen[b] and B. Nystrom[b]

a) Physics Department, Institute for Energy Technology, N-2027 Kjeller, Norway, kenneth.knudsen@ife.no[†]
b) Department of Chemistry, University of Oslo, N-0315 Oslo, Norway
† corresponding author

In order to elucidate the interplay between hydrophobic and hydrophilic forces as well as electrostatic interactions for a polymer in an aqueous environment, we recently designed a new pentablock polymer, with the configuration ABCBA. This is a linear chain, where two hydrophobic blocks (B) have been attached to each side of a hydrophilic segment (C), and with negatively charged groups (A) at the ends of the chain. In this system there will be a competition between the attractive forces of the hydrophobic blocks, the repulsion between the charged groups, and the tendency for the hydrophilic group to maximize the interaction with the surrounding water. The polymer was made in two versions, with different lengths of the hydrophilic block, having 34 and 77 segments, respectively. We observed that the physical properties of the system are highly dependent on the length of this C block. A sharp and highly reproducible temperature-induced transition, related to changes in chain conformation, is seen at a temperature around 37 °C. The reason for this behavior, as well as the robustness of the transitions discussed.

Con el objetivo de dilucidar la relación entre las fuerzas hidrofóbicas e hidrofílicas, así como de las interacciones electrostáticas para un polímero en ambiente acuoso, hemos diseñado recientemente un nuevo polímero penta-bloque, con la configuración ABCBA. Se trata de una cadena lineal, donde se han unido dos bloques hidrofóbicos (B) a cada costado de un segmento hidrofílico (C), y que posee grupos cargados negativamente (A), en los extremos de la cadena. En este sistema hay una competencia entre las fuerzas atractivas de los bloques hidrofóbicos, la repulsión entre los grupos cargados, y la tendencia del grupo hidrofílico a maximizar la interacción con el agua circundante. El polímero se obtuvo en dos versiones, con diferentes longitudes del bloque hidrofílico de 34 y 77 segmentos, respectivamente. Las propiedades físicas del sistema dependen fuertemente de la longitud del bloque C. Se observa una fuerte transición inducida por temperatura altamente reproducible, alrededor de los 37 °C, relacionada a cambios en la conformación de la cadena. Se discute la causa de este comportamiento, así como la robustez de la mencionada transición.

PACS: Polymer solutions flow properties, 47.57.Ng; structure of polymer solutions , 61.25.he; preparation of polymers, 81.05.g

INTRODUCTION

A fascinating property of so-called amphiphilic block copolymers is their ability to self-assemble into micelles, vesicles, and gels of various morphologies. This can occur as a response to environmental stimuli, e.g. by incorporating temperature-responsive blocks [1]. The term amphiphilic here refers to the different properties represented by two distinct blocks along the same chain, here hydrophilic ("water-friendly") and hydrophobic ("water-unfriendly") blocks. These polymers belong to an important class of materials with a large number of applications, including drug delivery systems, adaptive lubricants, and "smart" surface coatings [2-7]. Most of the previous studies on water-soluble copolymers have been focused on diblock and triblock systems [8-14]. However, we have recently started working with copolymers with up to five well-defined blocks along the chain (pentablock polymer), which opens up for a more complex range of interactions and behaviors in the system.

We here look specifically at results obtained on a ABCBA pentablock copolymer with different lengths of the hydrophilic C-block (cfr. Figure 1). It consists of one hydrophilic *poly(ethylene glycol)block* (PEG, block C), two thermo-sensitive *poly(-Nisopropylacrylamide)blocks* (PNIPAAM, block B), and an anionic *poly(4-styrenesulfonic acidsodium)* (PSSS, block A) block at both ends of the copolymer chain.

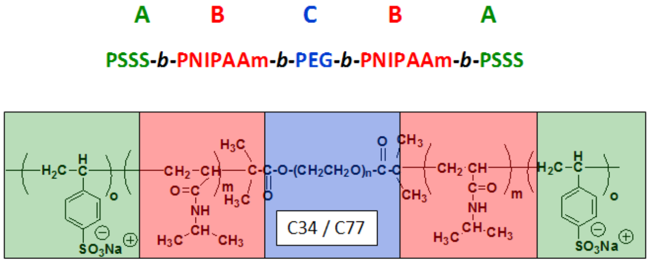

Figure 1: Schematics of the pentablock polymer used in this work. The color codes refer to hydrophobic (red), hydrophilic (blue), and charged groups (green). Here the repetition numbers for the A/B blocks are 12/63 (C34) and 14/65 (C77), respectively.

PNIPAAM is employed here since it is a highly sensitive thermoresponsive polymer that is able to associate and contract above its so-called lower critical solution temperature (LCST) of ca. 32 ºC, when being alone in solution [15]. The charged block at both ends of the chain are here introduced as an extra element of control in the system. It will amongst other factors ensure a high degree of solubility of the copolymer in water. Since the B-block becomes hydrophobic at a certain temperature, one may expect this block to combine with similar blocks from other chains and expel water, thus forming a nano-sized micellar structure.

It is of interest here to look at what kind of forces are expected to be present in this system. For polymer chains dissolved in water, there is usually a fine balance between several forces -all around or slightly higher than k_BT- that determine the actual conformation of the chain. In the case of the polymer chain studied here, we expect there to be a contribution from hydrophobic forces (entropy change for water), hydrophilic (e.g. hydrogen bonds with water molecules), Coulombic (due to the charged end groups), as well as the contribution to entropy (positive ΔS) upon any liberation of counterions from the polymer. Thus a conformational change as that depicted schematically in Figure 2 may be induced by one of these contributions dominating slightly over the others for an individual segment (monomer), and being strongly amplified by the fact that the polymer chain contains a large number of segments.

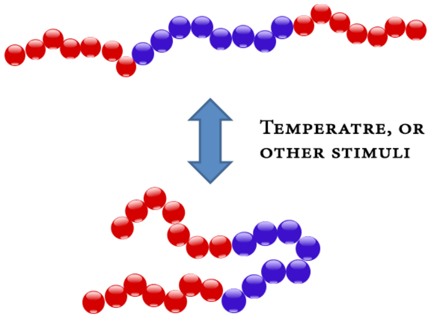

Figure 2. Simple schematics of conformational change for a polymer chain with hydrophobic (red) and hydrophilic (blue) segments.

This paper presents a summary of recent results obtained with this system, and will empasize how the length of the PEG block has a large impact on the temperature- induced viscosity and structure of the polymer. We also discuss the reversibility and cyclability of this behavior. More background information on this system can be found in ref. [16].

RESULTS AND DISCUSSION

In order to elucidate the association behavior in polymer systems, measurement of turbidity can be very useful as an initial step. Figure 3 shows how an extremely abrupt transition is observed for this system at a temperature around 37 ºC upon heating, for both chain lengths studied. The rise of the turbidity with increasing temperature indicates the formation of condensed structures, sufficiently large to scatter light. When the hydrophobic blocks of several chains interact and assemble, these will at elevated temperature contract strongly in order to avoid water exposure if there is a sufficient number of hydrophobic segments present.

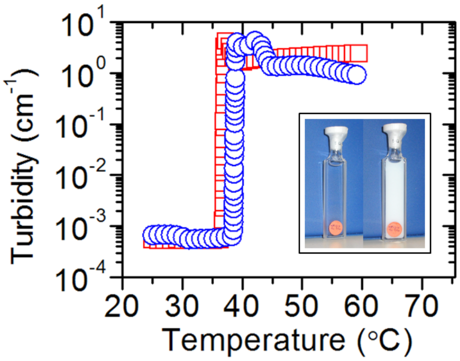

Figure 3. Change of turbidity vs. temperature for the C34 (red squares) and C77 (blue circles) system (4 *wt*.%). Inset: visual appearance at 25 ºC and 50 ºC for C34.

Also visual inspection of the system reveals that upon heating it becomes highly turbid (see inset Figure 3). Note that these changes were found to be fully reversible, thus the original character is regained upon cooling below the threshold. A series of new measurements, obtained after those presented in ref. [16] and during an extended period of several months, have shown that the heating/cooling process can be repeated nearly indefinitely without any observable loss in material properties. This behavior is actually not so common in soft-matter systems, where loss of reversibility and aggregation/ageing is seen very often. We believe that the main reason for this important property for the present system is the use of heavily charged end blocks, which stabilize the system and introduce a marked robustness in its behavior.

To gain further insight into this system, shear viscosity measurements were performed. A shear flow tends to bring polymer chains close to each other faster than from Brownian motion, thereby speeding up the assembly. This phenomenon is known as "orthokinetic" aggregation and it frequently appears in solutions or suspensions of sticky moieties at low shear rate. At high shear rate, on the other hand, the large association complexes are foreseen to break up under the influence of high shear stresses. The effects of temperature and shear rate on the viscosity of the system are illustrated in Figure 4. A much stronger temperature dependence of the viscosity is found for C77 than for C34, and an incipient shear rate effect is observed at high temperatures for C77, whereas no effect can be discerned for C34. This result clearly shows that interconnected and thus effectively larger species are formed in solutions of C77 at elevated temperatures, while only non-connected assemblies are formed in the C34 system. This interconnection between assemblies is provided by the long C-block. We may note here the dramatic viscosity increase (more than a factor 100) for the system with the longest central block upon a change in temperature. Also this change has now been found to be reproducible after long periods of repeated use.

We furthermore performed small-angle neutron scattering

(SANS) measurements on this system to gain insight about structural changes at the nanoscale. For both C34 and C77 we observe a dramatic change in the SANS pattern with increasing temperature. The low-q scattering increases more than a factor of ten, demonstrating that a significant structural reorganization takes place in the size regime probed by SANS. At 30 °C, i.e. below the threshold temperature, there is only weak scattering, as expected for a polymer that exists mainly as individual unfolded chains (unimers). We may here make use of the so-called Debye model [17] i.e. the form factor (P), developed for a flexible linear polymer chain in solution, where the scattering function is given by

$$P(x) = 2[e^{-x} + x - 1]/x^2, \qquad \text{with } x = (qR_G)^2.$$

Here q is the scalar of scattering vector, $q = (4\pi/\lambda)\sin\theta$, where λ is the neutron wavelength and θ is the scattering angle.

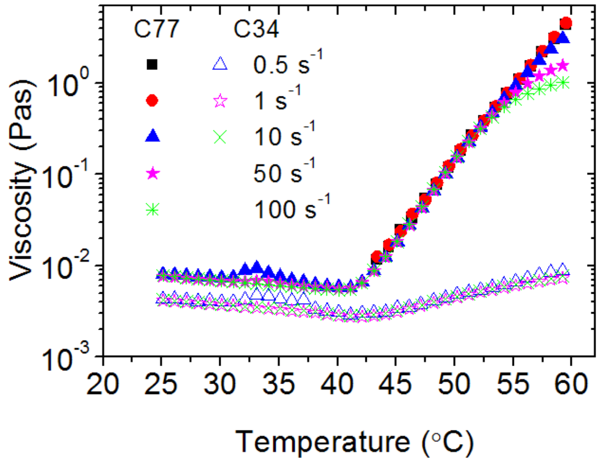

Figure 4. Viscosity dependence on temperature and shear rate, as well as on the length of the hydrophilic block for the two variants of the polymer chain.

This model results in a value for the radius of gyration (RG) of the unimer equal to 29 Å, or ca. 3 *nm* (the scattering from C34 and C77 at 30 °C cannot be distinguished in this respect). For the high temperature dataset the shape of the SANS data, including the suppression of the scattering at low q-values, encourages the use of a core-shell model [18] to fit the data. Due to the presence of charges it is necessary to include a Coulomb interaction in the model.

When using the core–shell form factor together with a screened Coulomb interaction potential [19] we obtain a good fit for the C77 polymer (as seen in Figure 5), giving an average core radius of 89 Å , and a shell thickness of 37 Å . This would correspond to an overall particle diameter of 252 Å , or ca. 25 *nm*. In this calculation we have employed the already known values of the D_2O scattering length density and the dielectric constant, i.e. 6.3×10^{-6} $Å^{-2}$ and 78, respectively. For the short PEG-chain polymer (C34) the model fit shown in Figure 5 deviates from the data at the lowest q-values, most likely due to the existence of a population of larger particles whose size cannot be determined within this q-range.

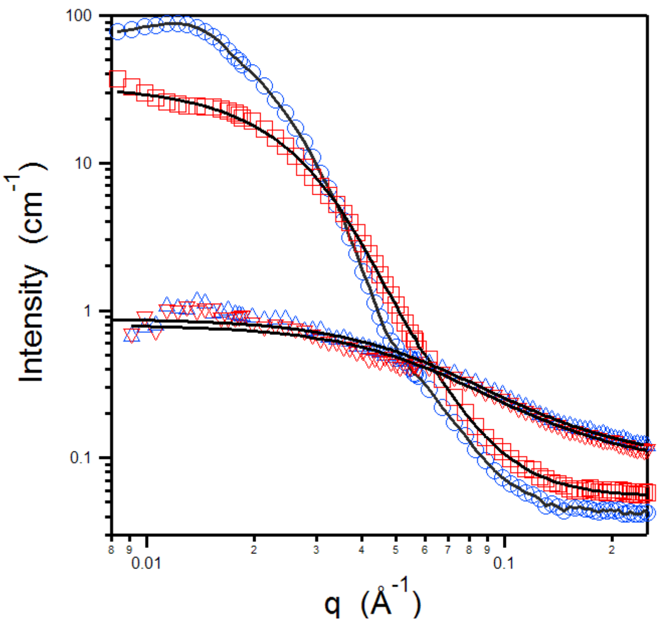

Figure 5. SANS patterns for C34 (red squares) and C77 (blue circles) at 50 °C and at 30 °C (triangles).

Overall, the SANS study shows clearly how these chains assemble to form core-shell particles upon a temperature increase above the transition, which was found to be at ca. 37 °C.

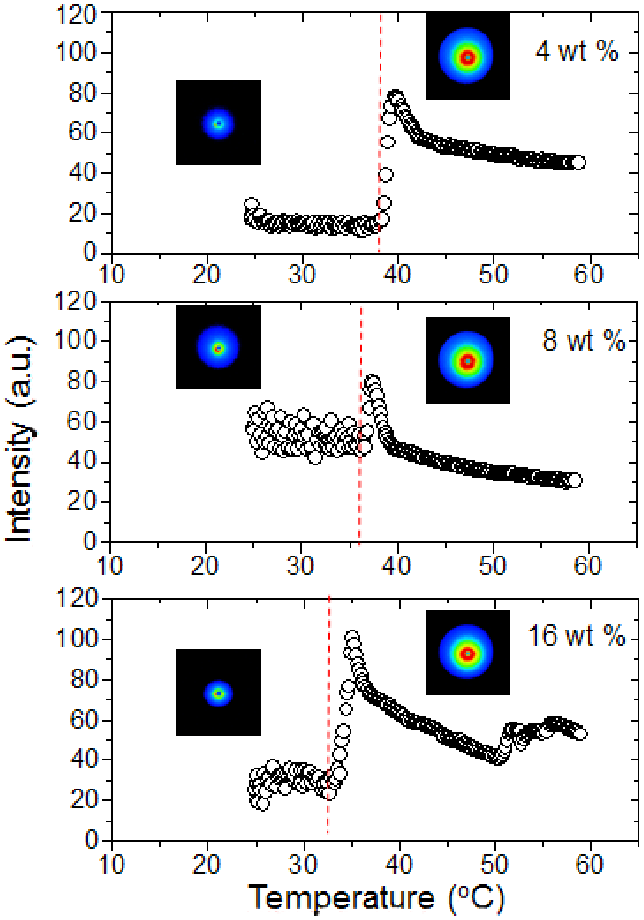

Figure 6: Small angle light-scattering (SALS) intensity vs. temperature for three different concentrations of the C34 system; 4, 8, and 16 *wt*.%. The insets show the 2D SALS patterns at low temperature and at the peak of the transition.

We have recently also studied the effect of polymer concentration on the behavior of this system. It is found that the transition temperature can be moved down in steps upon an increase in concentration. This is illustrated in Figure 6, where the change in light scattering intensity was used to probe the system through the transition region.

It can here be seen how the initial transition temperature just above 37 ^oC (4 *wt*.%) is shifted towards 35 ^oC and subsequently to 32 ^oC for the 8 and 16 *wt*.% systems, respectively. However, the increased concentration will also have strong influence on the polymer chain conformation and interaction between chains, effects that need further studies to be clarified in detail.

CONCLUSIONS

We have revisited our recent studies on thermoresponsive polymers, with a particular focus on a pentablock system (ABCBA). It is shown how a highly abrupt transition from extended chains to globular entities can be induced by proper combination of hydrophilic and hydrophobic elements. Repeated studies have shown that this behavior is not only fully reversible, but shows no signs of ageing even over extended periods of time. We have reason to believe that the incorporation of charged end groups is an important element in this respect. The well-defined changes observed in opacity together with the cyclability could be of interest in connection with e.g. adaptable surface layers without the need for external (e.g. electrical) connections.

ACKNOWLEDGMENTS

K. Z. and B. N. acknowledge support from the Norwegian Research Council through the project 177665/V30.

[1] *Block Copolymers in Nanoscience*, Ed. M. Lazzari, G. Liu, S. Lecommandoux, (Wiley-VCH, Weinheim, 2006).
[2] V. Sfika and C. Tsitsilianis, Macromolecules **37**, 9551 (2004).
[3] X. Y. Xiong, K. C. Tam and L. H. Gan, Polymer **46**, 1841 (2005).
[4] C. Xu, X. Fu, M. Fryd, S. Xu, B. B. Wayland, K. I. Winey andR. J. Composto, Nano Lett. **6**, 282 (2006).
[5] J. F. Tan, P. Ravi, H. P. Too, T. A. Hatton and K. C. Tam, Biomacromolecules **6**, 498 (2005).
[6] Y. Liu, V. Klep, B. Zdyrko and I. Luzinov, Langmuir **21**, 11806 (2005).
[7] Y. Kim, J. Pyun, J. M. J. Frechet, C. J. Hawker and C. Frank, Langmuir **21**, 10444 (2005).
[8] B. Svensson, U. Olsson and P. Alexandridis, Langmuir **16**, 6839 (2000).
[9] X. Zhao, W. Liu, D. Chen, X. Lin and W. W. Lu, Macromol. Chem.Phys. **208**, 1773 (2007).
[10] K. Zhu, R. Pamies, A.-L. Kjøniksen and B. Nystrom, Langmuir **24**, 14227 (2008).
[11] A. -L. Kjøniksen, K. Zhu, R. Pamies and B. Nystrom, J. Phys. Chem. B **112**, 3294 (2008).
[12] T. Ueki, M. Watanabe and T. Lodge, Macromolecules **42**, 1315 (2009).
[13] S. Reinicke, J. Schmelz, A. Lapp, M. Karg, T. Hellweg and H. Schmalz, Soft Matter **5**, 2648 (2009).
[14] S. De Santis, R. D. Ladogana, M. Diociaiuti and G. Masci, Macromolecules **43**, 1992 (2010).
[15] H. G. Schild, Prog. Polym. Sci. **17**, 163 (1992).
[16] N. Beheshti, K. Zhu, A. -L. Kjøniksen, K. D. Knudsen, B. Nyström, Soft Matter **7**, 1168 (2011).
[17] R. -J. Roe, *Methods of X-Ray and Neutron Scattering in Polymer Science*, (Oxford University Press, New York, 2000).
[18] J. B. Hayter, in *Physics of Amphiphiles–Micelles, Vesicles, and Microemulsions.* Ed. V. de Giorgio and M. Corti, (North Holland, Amsterdam, pp. 59–93, 1983).
[19] J. B. Hayter and J. Penfold, Mol. Phys. **42**, 109 (1981).

THE FREDERIKS TRANSITION IN AN AQUEOUS CLAY DISPERSION

LA TRANSICIÓN FREDERIKS EN UNA DISPERSIÓN ACUOSA DE ARCILLA

H. Hemmen, E. L. Hansen, N. I. Ringdal and J. O. Fossum†

Department of Physics, NTNU, Trondheim, Norway, jon.fossum@ntnu.no†
† corresponding author

We show that under certain circumstances, aqueous dispersions of Na-fluorohectorite synthetic clay display transient spatially periodic structures when subjected to magnetic fields. These nematic structures result from the deformation of a uniform director pattern, a phenomenon which is known as the Frederiks transition. We study the samples between crossed polarizers, and present birefringence images of the particle reorganization as a function of time. Repeated measurements at different magnetic field strengths show that the threshold value for the inhomogeneous Frederiks transition with this setup is just below $0.5\ T$, and that the spatial wavelength of the structures decreases when the magnetic field is increased, as is expected.

Se muestra que, bajo ciertas circunstancias, las dispersiones acuosas de arcilla sintética de Na-fluorohectorita exhiben estructuras espacialmente periódicas transitorias, cuando se someten a campos magnéticos. Tales estructuras nemáticas resultan de la deformación de un patrón uniforme director, un fenómeno que se conoce como la transición Frederiks. Se estudian las muestras entre polarizadores cruzados, y las imágenes de birrefringencia de la reorganización de partículas en función del tiempo. Las mediciones repetidas con diferente intensidad de campo magnético, muestran que el valor umbral de la transición Frederiks inhomogénea con esta configuración está justo por debajo de $0.5\ T$, y que la longitud de onda espacial de las estructuras disminuye cuando el campo magnético se incrementa, como es de esperar.

PACS: Structure of nematic liquid crystals, 61.30.-v; phase separation and segregation in colloids, 64.75.Xc; birefringence in bulk materials and thin films, 78.20.Fm

The Frederiks transition [1] is a phenomenon occurring in liquid crystals when a field is used to realign the nematic director away from its (field-free) equilibrium position. The path between the initial and final states often involve transient, spatially periodic structures, where adjacent domains rotate in opposite directions [2-3]. Due to its usefulness for determining material properties of liquid crystals (e.g. the elastic constant of the mode involved in the distortion), several theoretical and experimental studies have been performed on the Frederiks transition, both with rod-like and disk-like molecules (see e.g. [4-6]).

Liquid crystalline order in aqueous clay dispersions has attracted attention in recent years, see e.g. [7-10]. Here we report an observation of the Frederiks transition in dispersions containing the synthetic smectite clay Na-fluorohectorite. When mixed in water and left to phase separate over time, this system develops several coexisting phases in a single sample tube [7]. From bottom to top, these are: an isotropic gel region, a nematic gel region, a nematic sol region, and an isotropic sol. Due to the comparatively high viscosity and shear thinning behavior of the nematic gel, its dynamic response to magnetic fields is strongly damped [11]. However, the liquid-like nematic sol has been shown to respond relatively fast to magnetic fields [7], allowing particle reorientation with fields on the order of $0.1\ T$.

The samples used for the present experiments were dispersions of 3 % w/w of Na-fluorohectorite in $10^{-3}\ M$ NaCl suspensions, contained in 2 mm diameter glass capillaries. We let the samples settle for 4-5 months, during which the largest particle aggregates sediment out, and the four different regions appear in the samples. Before applying any magnetic fields, the clay particles in the nematic sol orient antinematically, i.e. with their particle normals spread out in the plane perpendicular to the capillary axis [7]. This is due to the circular geometry of the capillary, and the fact that the disk-like particles anchor homeotropically to interfaces [7].

In order to induce the Frederiks transition, a magnetic field of about 1 Tesla was first applied to the nematic sol phase perpendicular to the capillary axis. Due to the negative diamagnetic susceptibility anisotropy of the particles, they respond to magnetic fields by orienting their plate normals perpendicular to the magnetic field lines. Combined with the influence of the particles that are homeotropically anchored to the capillary walls, the field acts to change the nematic configuration from antinematic to uniaxial nematic, with the particle normals oriented on average along a common direction in the horizontal plane, perpendicular to the magnetic field lines.

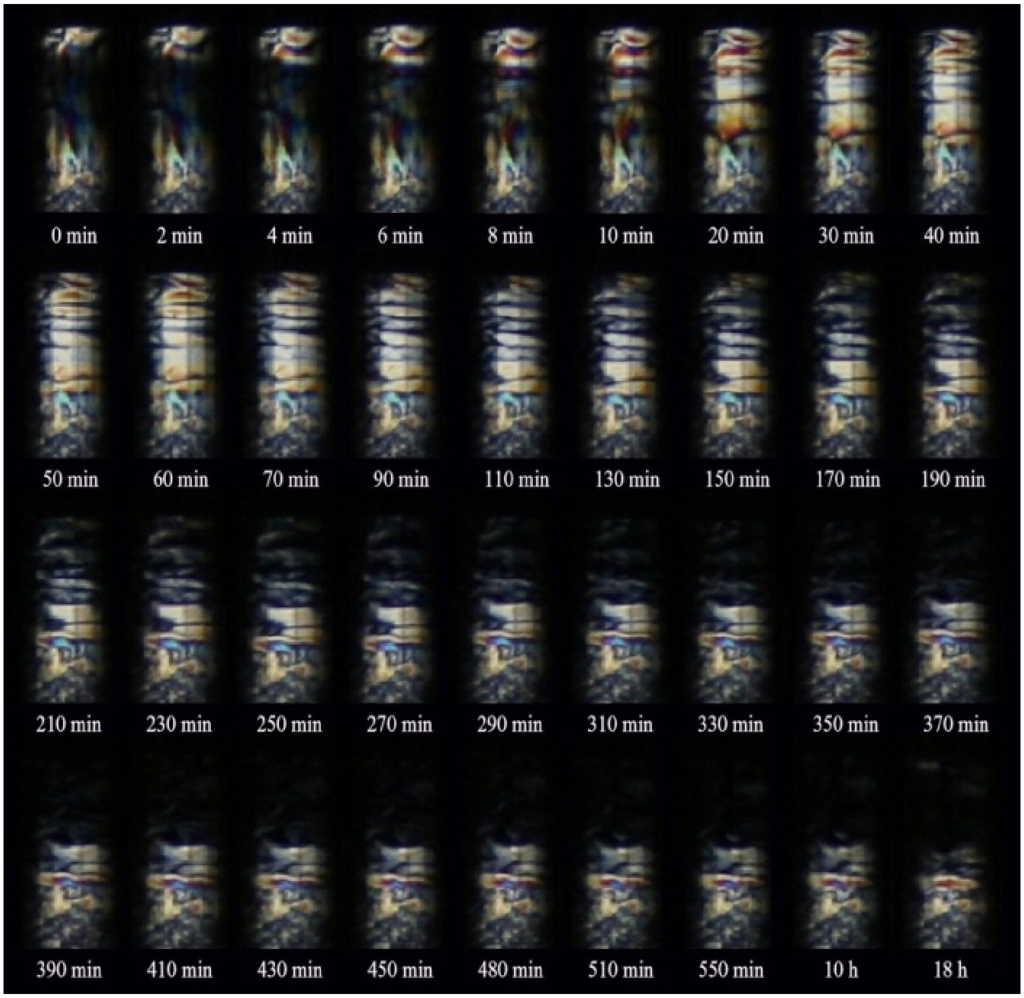

Figure 1: Photo series of the reorientation process of a nematic phase in a 1 T magnetic field. The particles are initially aligned with the director horizontally in the paper plane, and a reorientation is triggered by applying the magnetic field in the same direction. The first sign of stripes appears after a couple of minutes, being most visible in the upper part. After about 8 hours, the majority of the particles are reoriented to a stable configuration where their plate normals point along the line of sight (out of the paper) or vertically, and therefore do not contribute to the birefringence. The vertical black stripes in the pictures are reflections from the magnet

Once this particle configuration was obtained, the capillary was rotated 90 degrees around its axis, thus initially causing the clay plate normals to be aligned in the magnetic field direction. This unstable configuration promoted realignment of the nematic phase. During the subsequent realignment process, visual images were recorded through crossed polarizers, allowing a visualization of the anisotropy in the particle alignment. The polarizers were oriented such that their fast axes were respectively vertical (parallel to the capillary axis), and horizontal (parallel to the magnetic field). A time series of the recorded images with a magnetic field strength of 1 T can be seen in Figure 1. As the magnetic field reorients the particles, transient periodic stripes gradually appear and disappear during the hours-long process of reorientation. The stripes correspond to regions where the particles are oriented with the average plate normal at an angle to the transmission axes of the polarizers.

In systems of platelets with negative diamagnetic susceptibility anisotropy, the non-uniform Frederiks transition is different from that observed in systems with positive diamagnetic susceptibility, in that the first case possesses degeneracy in tilt-angles directions perpendicular to the director axis. For a round flat particle with negative anisotropy of the magnetic susceptibility, a static magnetic field cannot by itself determine which orientation the final director will obtain. In other experiments on systems of disks with this behavior [5-6], the degeneracy is removed by rotating the magnetic field or the sample in the plane normal to the final director orientation.

As these are preliminary measurements, we have not yet modified our setup in this way, and thus we are not yet able to fully characterize the nature of the transition, partly because from birefringence images using only linear polarizers one cannot unambiguously determine the orientation of the particle normals. This could have been achieved using a more complex polarizer setup, e.g. Mueller matrix ellipsometry [12]. However, based on previous experiments using small angle x-ray scattering to determine particle orientation, we expect that the particles in the top part of the nematic sol region reorients to a mainly horizontal alignment (particle normal parallel to the capillary axis), due to the anchoring to the isotropic-nematic interface. After several rotations, all particles will eventually reach this orientation, as it is the only configuration where the particle normal stays perpendicular to the magnetic field. Additionally, several factors of the clay water system, such as gelation and long range colloidal interactions, makes the nematic phase in a clay suspension different from ordinary liquid crystals. From the images of the evolution of the periodic patterns (Figure 1) it can be seen that the stripe formation commences at the top of the nematic sol, close to the isotropic-nematic interface. This could be due to a viscosity gradient in the nematic sol along the capillary axis, i.e. lower viscosity near the isotropic-nematic interface and highest near the transition to the nematic gel.

Figure 2 shows repeated measurements with identical samples, using magnetic fields from 0.5 to 1 Tesla. The threshold value for the inhomogeneous Frederiks transition with this setup is found to be just below 0.5 Tesla. Because of irregularities in the nematic domains, and the limited extent of the nematic sol region, it is with the present samples not possible to obtain precise values for the wavelength for a specific magnetic field strength. However, it seems clear that there is a decrease in wavelength when the magnetic field is increased, and close to 0.5 Tesla, the wavelength looks to diverge, as expected.

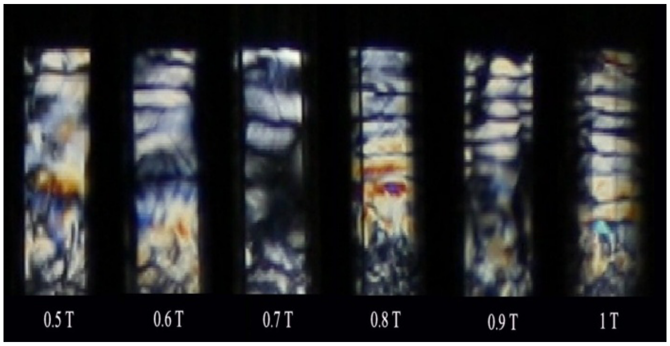

Figure 2: Stripe patterns for magnetic fields from 0.5 to 1 Tesla in the same sample. The pictures were taken at the point in time when the stripes were most clearly defined.

For all the measurements the wavelength shows a tendency to increase as we move down in the sample, which could be due to a viscosity gradient in the nematic gel as the concentration of particles in the nematic sol increases downwards. Furthermore, the duration of the instability decreases with increasing field strengths: the whole process lasts for over 3 hours with magnetic fields close to the threshold, and under 2 hours for fields of 1 Tesla. For low field strengths, the first sign of stripe formation appears after 10 minutes, while for the highest strengths it can take less than five minutes. The periodic structures are clearly transient phenomena, and are seen to decay soon after the magnet is removed. The lifetime is around 2 hours after which there is no longer any pattern with systematic structure.

---

[1] A. Repiova and V. Frederiks, J. Russ. Phys.-Chem. Soc. **59**, 183 (1929).
[2] P. G. d. Gennes and J. Prost, *The physics of liquid crystals* (Oxford University Press, Oxford, 1993), pp. xvi.
[3] A. J. Hurd, S. Fraden, F. Lonberg, and R. B. Meyer, J. Phys-Paris **46**, 905 (1985).
[4] Z. Dogic and S. Fraden, Langmuir **16**, 7820 (2000).
[5] D. van der Beek, P. Davidson, H. H. Wensink, G. J. Vroege, and H. N. W. Lekkerkerker, Phys. Rev. E **77**, 031708 (2008).
[6] M. R. Kuzma, Phys. Rev. Lett. **57**, 349 (1986).
[7] H. Hemmen, N. I. Ringdal, E. N. De Azevedo, M. Engelsberg, E. L. Hansen, Y. Meheust, J. O. Fossum and K. D. Knudsen, Langmuir **25**, 12507 (2009).
[8] N. I. Ringdal, D. M. Fonseca, E. L. Hansen, H. Hemmen, and J. O. Fossum, Phys. Rev. E **81**, 2010).
[9] J. C. P. Gabriel, C. Sanchez, and P. Davidson, J. Phys. Chem. **100**, 11139 (1996).
[10] L. J. Michot, I. Bihannic, S. Maddi, S. S. Funari, C. Baravian, P. Levitz, and P. Davidson, Proc. Natl. Acad. Sci. U.S.A. **103**, 16101 (2006).
[11] E. N. de Azevedo and M. Engelsberg, Langmuir **25**, 1175 (2009).
[12] M. Kildemo, L. M. S. Aas, P. G. Ellingsen, H. Hemmen, E. L. Hansen and J. O. Fossum, Proc Spie, **8082**, 808221 (2011).

INTERMITTENCY OF FLUID IMBIBITION IN DISORDERED MEDIA

INTERMITENCIA EN IMBIBICIÓN FLUIDA EN MEDIOS DESORDENADOS

X. Clotet[a,b], S. Santucci[a,c †] and J. Ortín[b]

a) Laboratoire de Physique, CNRS UMR 5672, Ecole Normale Supérieure de Lyon, 46 Allée d'Italie, 69364 Lyon Cedex 07, France, stephane.santucci@ens-lyon.fr†
b) Departament d'Estructura i Constituents de la Matèria, Universitat de Barcelona, Martì i Franquès 1, 08028 Barcelona, Spain
c) Centre for Advanced Study at The Norwegian Academy of Science and Letters, Drammensveien 78, 0271 N-Oslo, Norway
† corresponding author

We present an experimental study of the global velocity spatially averaged over the length scale ℓ, $V_\ell(t)$, of an air-liquid interface during the forced-flow imbibition of a viscous wetting liquid in a disordered medium. Thanks to a high resolution fast camera, we have followed directly the imbibition front and observed a complex dynamics, governed by power-law distributed avalanches on a wide range of durations and sizes [1, 2]. We characterize here this intermittent behavior by studying the statistical properties of the global velocity increments $\Delta V_\ell(\tau) \equiv V_\ell(t+\tau) - V_\ell(t)$ for various time lags τ. In particular we show that the shape of the PDF of $\Delta V_\ell(\tau)$ evolve with increasing τ from fat tail exponentially stretched PDFs towards a Gaussian PDF above a characteristic time τ_c, which corresponds to the characteristic avalanche duration.

Presentamos un estudio experimental de la velocidad global promediada espacialmente a escala ℓ, $V_\ell(t)$, de una interfaz aire-líquido en imbibición a flujo constante en un medio desordenado de un líquido viscoso que moja el medio. Mediante una cámara de alta resolución hemos seguido directamente el frente de imbibición, observando una dinámica compleja gobernada por avalanchas distribuidas en ley de potencias en un amplio rango de duraciones y tamaños [1, 2]. Caracterizamos este comportamiento intermitente estudiando las propiedades estadísticas de los incrementos de la velocidad global $\Delta V_\ell(\tau) \equiv V_\ell(t+\tau) - V_\ell(t)$, para varios intervalos de tiempo τ. En concreto mostramos que la forma de la distribución de probabilidad de $\Delta V_\ell(\tau)$, a medida que τ aumenta, evoluciona de una distribución de colas largas a una distribución Gaussiana para τ mayor que un tiempo característico, τ_c, que corresponde a la duración característica de las avalanchas.

PACS: Fluctuation phenomena statistical physics, 05.40.-a; structure and roughness of interfaces, 68.35.Ct; fluid flow through porous media, 47.56.+r; fractals fluid dynamics, 47.53.+n

INTRODUCTION

Fluid invasion in disordered media -similarly to a wide variety of slowly driven heterogenous systems such as the motion of magnetic domain walls in disordered ferromagnets [3], wetting contact lines on rough substrates [4] or crack growth in heterogenous media [5, 6], exhibits a burst-like correlated dynamics spanning a very broad range of temporal and spatial scales [7-9]. Such a complex dynamics, generically referred to as "crackling noise", is the result of several competing forces acting at different length scales: while the fluctuations in capillary forces and the heterogeneous permeability destabilize the fluid interface, viscosity and surface tension damp the resulting interfacial fluctuations, leading finally to long-range correlations along the imbibition front. The correlation length, which measures the extent of the lateral correlations, is given by $\ell_c = \sqrt{\kappa / Ca}$, where κ is the permeability of the medium, and Ca the capillary number. As a consequence, imbibition fronts in a disordered medium undergo a complex kinetic roughening process characterized by an intermittent dynamics. In the limit $Ca \to 0$ the system displays critical interfacial fluctuations [10].

More specifically, using high resolution fast imaging in quasi two-dimensional forced-flow imbibition, we have shown recently that the front motion is driven by localized avalanches, power-law distributed both in sizes and durations, with exponentially decaying cutoffs that are related to the lateral correlations of the interface and diverge as the driving velocity decreases [2]. We demonstrated that the critical spatiotemporal dynamics observed during forced-flow imbibition can be described within the framework of a pinning-depinning transition. Moreover, we have shown that these local avalanches lead to a complex temporal activity of the global advancement of the front, with in particular large global velocity fluctuations that follow an asymmetric non-Gaussian distribution with a large exponential tail, due to the presence of spatial correlations along the front and finite-size effects [1, 11].

In the present work we go further on in the investigation of the global dynamics of imbibition fronts, and quantify the global intermittent behavior. Specifically, we analyze the statistical properties of the global velocity increments $\Delta V_\ell(\tau) \equiv V_\ell(t+\tau) - V_\ell(t)$ for various time lags τ, and we show that the PDF of $\Delta V_\ell(\tau)$ evolves with increasing τ from fat tail exponentially stretched PDFs towards a Gaussian PDF above a characteristic time τ_c, which corresponds to the characteristic avalanche duration.

EXPERIMENTAL SETUP

The setup used in the present work (Fig. 1) has been previously described in Ref. [2]. It consists on a Hele-Shaw (HS) cell of 190 × 500 mm^2 (width × length), made of two parallel thick glass plates separated by a narrow gap spacing. We introduce dichotomic fluctuations in space of the gap thickness, $b = 0.46$ *mm* and $b - \delta b = 0.40$ *mm*. These spatial fluctuations are provided by copper patches of size 0.4×0.4 mm^2 and height $\delta b = 0.06$ *mm*, randomly distributed over a fiberglass substrate attached to the bottom plate and filling 35% of the total area. The patches do not overlap, and their orientation is shown in the bottom panel of Fig. 1.

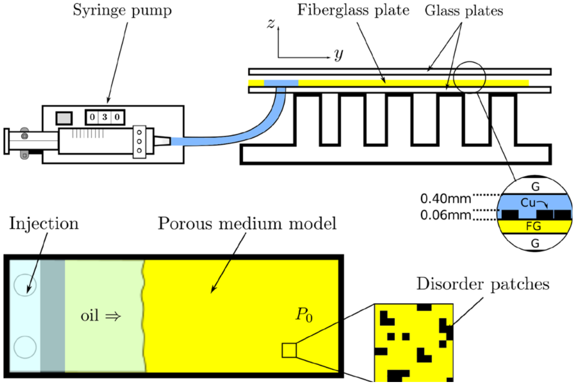

Figure 1: Sketches of the experimental setup. Top panel: the control parameter v is set by the syringe pump. The zoom on the right is a lateral view of the disordered HS cell, showing the parallel glass plates (G) and the fiberglass (FG) substrate with the copper obstacles (Cu). Bottom panel: sketch of the cell from top. The right end is open to air. The oil penetrates from the injection point at constant flow rate (constant average velocity v) and fills the porous medium model, displacing the resident fluid (air).The zoomed region shows the disorder patches and their orientation with respect to the fluid front.

We use a silicone oil (Rhodorsil 47V) as invading fluid, with dynamic viscosity $\mu = 52$ *mPa·s*, density $\rho = 1000$ kg/m^3, and oil-air surface tension $\sigma = 20.7$ *mN/m* at room temperature (23 ºC). The oil wets perfectly the glass plates, the copper patches and the fiber-glass substrate. The fluid is driven into the cell at a constant flow rate imposed by a syringe pump. Here, we will study the fluid invasion for one imposed flow rate corresponding to a mean front velocity $v = 0.131$ *mm/s*. Thus, both the local front height and the local velocity are correlated along the fluid interface up to the length scale $\ell_c = \sqrt{\kappa/(\mu v/\sigma)}$ = 7 *mm*, that corresponds to 5% of the system size $L = 136$ *mm*. We have performed 19 different experiments that explore various disorder realizations.

In the course of an experiment the interface propagates about 150 *mm* in the *y* direction before reaching a statistically stationary state with constant RMS fluctuations of the front height. The motion of the oil-air front is then recorded using a Motion Pro X3 plus video-camera with 1280 pixels in the transverse direction and 256 to 280 pixels in the direction of fluid advancement (*y*). The typical spatial resolution is $r = 0.106$ *mm*/pixel. We record about 10000 images per experiment at 100 *fps* (frames per second). An edge-tracking algorithm is applied to obtain the front position $h(x,t)$. In order to measure the local velocity $v(x, h(x,t))$ of the front we use a method developed for slow crack growth in heterogeneous materials [5], which consists on computing the waiting time $wt(x, y = h(x,t))$ that the front has spent on each position during its propagation. The local velocity map is then computed as $v(x, h(x,t)) = r/wt(x, y = h(x,t))$. Finally, from this local measurement, the global velocity of the front can be computed at any window size ℓ, as $V_\ell(t) = \frac{1}{\ell}\int_\ell v(x,t)dx$.

EXPERIMENTAL RESULTS

We will examine here the temporal fluctuations of the average velocity $V_\ell(t)$ as a function of the measuring window length scale ℓ. As shown on Fig. 3, even though the injection rate is constant, we observe that $V_\ell(t)$ is a jerky signal with a complex intermittent behavior characterized by very large positive fluctuations or avalanches [1]. We consider an avalanche as the occurrence of $V_\ell(t)$ above an arbitrary threshold, chosen here as the mean velocity $\langle V_\ell(t) \rangle$ (which would correspond to the imposed velocity *v* in an infinite system). We define the size *S* and duration *T* of an avalanche in the form shown in the bottom panel of Fig. 3. The avalanche size *S* represents the extra displacement of the average front within the duration *T*.

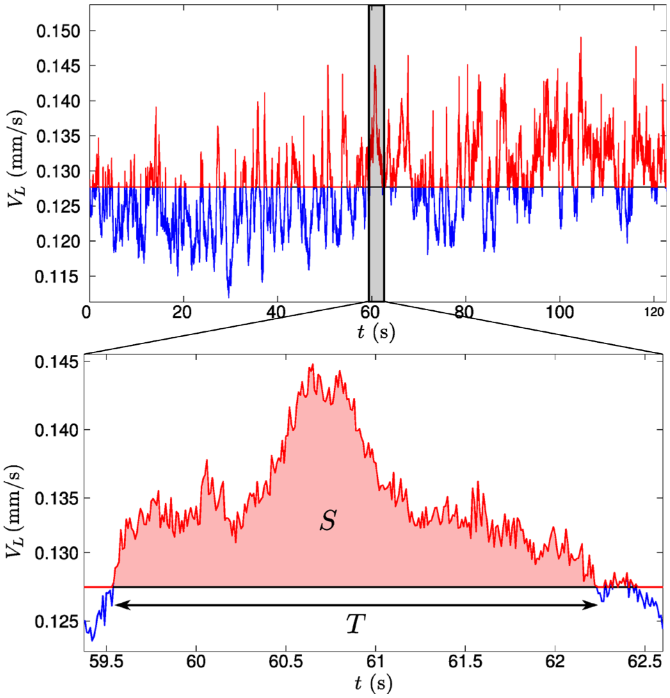

Figure 2: The top panel shows the global velocity signal for $\ell = L$, clipped by its average value. In the bottom panel a single avalanche is depicted, with size *S* and duration *T*.

We focus now on the statistics of avalanche durations in two cases, depending on whether the global velocity V_ℓ is computed for $\ell < \ell_c$ or $\ell > \ell_c$. The corresponding distributions of avalanche durations are plotted in Fig. 3. In the top panel ($\ell > \ell_c$) we observe that the PDFs follow a power law with exponential cutoffs T_c that increase as the length of the measuring window ℓ is shortened towards ℓ_c. The inset shows the evolution of these cutoffs with ℓ. In the bottom panel ($\ell < \ell_c$), in contrast, the PDFs are exponential and do not evolve.

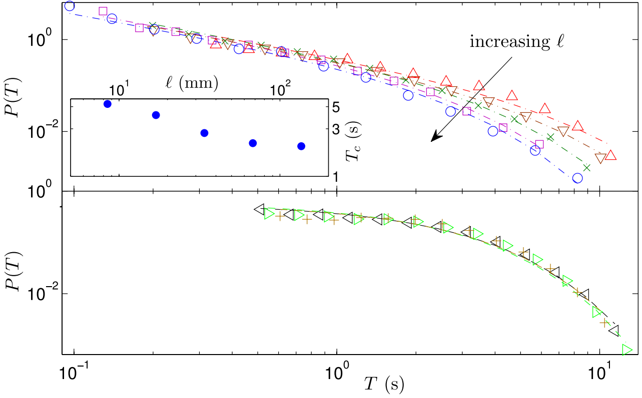

Figure 3: Top panel: PDFs of avalanche durations T, for window sizes $\ell = L/n$ ($> \ell_c$) with $n = 1, 2, 4, 8, 16$. Dashed lines are fits to power laws with exponential cutoffs. In the inset the cutoff duration T_c is plotted as a function of ℓ. Bottom panel: PDFs of avalanche durations T, for window sizes $\ell = L/n$ ($< \ell_c$) with $n = 32, 40, 50$. Dashed lines are fits to decaying exponentials with nearly the same characteristic duration $T_c = 2.06 \pm 0.06$.

In order to study the temporal fluctuations of $V_\ell(t)$, we analyze the statistical properties of the global velocity increments $\Delta V_\ell(\tau)$ for various time delays τ, and observation length scales ℓ. Such analysis has been originally proposed to study the intermittent behavior of turbulent flows [12]. We show on Fig. 4 the distributions of the normalized velocity increments $Y \equiv (\Delta V_\ell - \langle V_\ell \rangle)/\sigma_{\Delta V_\ell}$ for logarithmically increasing time lags τ and the global velocity measured at $\ell = L/8$. Interestingly, we observe that the shape of these distributions evolves through the temporal scales τ from fat tail exponentially stretched distributions at small time lags towards Gaussian distributions above a characteristic time τ_c. Such behavior is indicative of the intermittent character of the fluid invasion process, and uncovers complex temporal correlations [12-14] for durations shorter than τ_c.

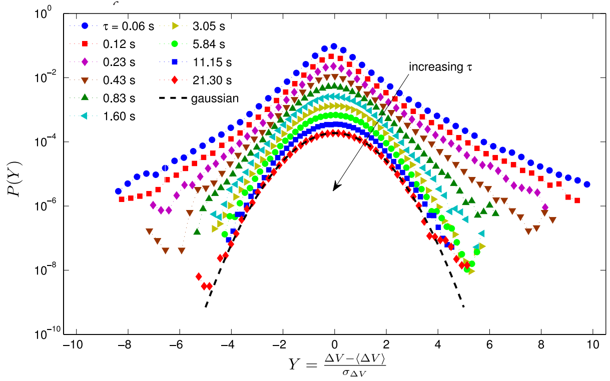

Figure 4: Semilog plot of $P(Y)$ vs $Y \equiv (\Delta V_\ell - \langle V_\ell \rangle)/\sigma_{\Delta V_\ell}$ (dotted lines) for increasing time lags τ and for $\ell = L/8$, shifted vertically for visual clarity. The PDFs evolve from fat tail distributions for $\ell < \ell_c$ to Gaussian distributions for $\tau > \tau_c \simeq 2\ s$. A Gaussian PDF (dashed line) is also plotted as a guide to the eye.

To characterize and quantify the flatness of these PDFs, we compute the kurtosis $k \equiv E(x - \langle x \rangle)^4/\sigma^4$ of the distributions $P(\Delta V_\ell(\tau))$, where E stands for the expected value. On Fig. 5 we represent the kurtosis vs. the time lag τ, varying systematically the measuring window size ℓ. We observe that the kurtosis decreases systematically as τ and ℓ increase. Above a characteristic duration τ_c it converges to the value $k_G = 3$ of a Gaussian signal whenever $\ell > \ell_c$, in agreement with the result of the previous Fig. 4. In contrast, for $\ell < \ell_c$ the kurtosis at large τ saturates to $k > k_G$, implying that the underlying statistics is not Gaussian. Below τ_c, the increase of the kurtosis at progressively shorter temporal scales seems to be close to a power law $k \propto \tau^{-\alpha}$. The power-law exponent α measures the intermittency strength of the global velocity at short durations [14]. Its evolution with the measuring window length scale is reported in the inset of Fig. 5.

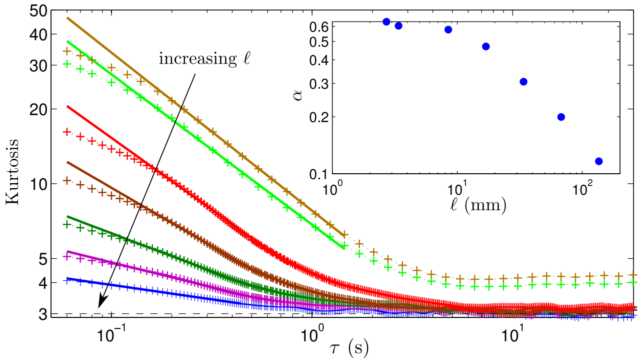

Figure 5: Kurtosis of $\Delta V_\ell(\tau)$ for $\ell = L/n$ and $n = 1, 2, 4, 8, 16, 40, 50$, in log-log scale. The kurtosis is a measure of the flatness of the distribution. The dashed line represents the value for a Gaussian distribution, $k_G = 3$. Solid lines are power-law fits, $\tau^{-\alpha}$, for small τ. Inset: exponent α as a function of ℓ.

Finally, we have extracted the characteristic time τ_c at which the kurtosis flattens out. Interestingly, the values of τ_c and especially their evolution with the measuring window size ℓ appear very close to the typical durations of the global avalanches, defined as $\langle T \rangle$. This similar trend is shown in Fig. 6.

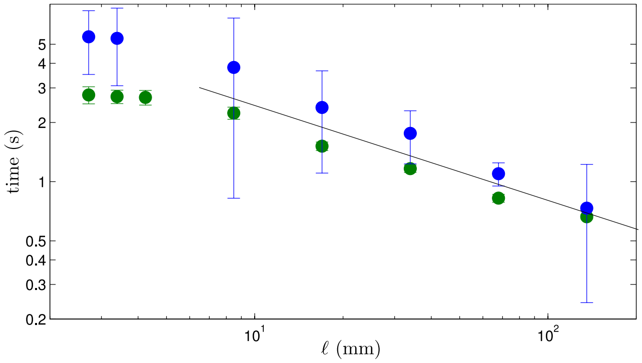

Figure 6: Characteristic times τ_c and $\langle T \rangle$ vs ℓ in log-log scale. The values of τ_c (squares) are obtained from analyzing the kurtosis of $P(\Delta V_\ell(\tau))$ with $\ell = L/n$ and $n = 1, 2, 4, 8, 16, 40, 50$. Those of $\langle T \rangle$ (circles) are the mean duration of avalanches for $\ell = L/n$ and $n = 1, 2, 4, 8, 16, 40, 50$. The solid line is plotted as a guide to the eye for $\ell > \ell_c$.

CONCLUSIONS

By analyzing the statistical behavior of the differences in the global velocity of imbibition fronts in time lapses τ and observation windows ℓ, we have shown that the dynamics displays the characteristic features of an intermittent process. The shape of the PDF of $\Delta V_{\ell}(\tau)$ evolves with increasing τ from a fat tail exponentially stretched PDF to a Gaussian PDF above a characteristic time τ_c, which corresponds to the characteristic avalanche duration.

---

[1] R. Planet, S. Santucci and J. Ortín, Phys. Rev. Lett. **102**, 94502 (2009).

[2] S. Santucci, R. Planet, K. Jørgen Måløy and J. Ortín., Europhys. Lett. **94**, 46005 (2011).

[3] G. Durin and S. Zapperi, Phys. Rev. Lett. **84**, 4705 (2000).

[4] E. Rolley, C. Guthmann, R. Gombrowicz and V. Repain, Phys. Rev. Lett. **80**, 2865 (1998).

[5] K. J. Måløy , S. Santucci, J. Schmittbuhl and R. Toussaint, Phys. Rev. Lett. **96**, 045501 (2006).

[6] D. Bonamy, S. Santucci and L. Ponson, Phys. Rev. Lett. **101**, 045501 (2008).

[7] M. Kardar, Phys. Rep. **301**, 85 (1998).

[8] D. S. Fisher, Phys. Rep. **301**, 113 (1998).

[9] J. P. Sethna, K. A. Dahmen and C. R. Myers, Nature **410**, 242 (2001).

[10] M. Alava, M. Dubé and M. Rost, Adv. Phys. **53**, 83 (2004).

[11] R. Planet, S. Santucci and J. Ortín, Phy. Rev. Lett. **105**, 029402 (2010).

[12] B. Castaing, Y. Gagne and E. J. Hopfinger, Physica D 46, **177** (1990).

[13] E. Bertin, Phys. Rev. Lett. **95**, 170601 (2005).

[14] L. Chevillard, B. Castaing, A. Arneodo, E. Leveque, J. -F. Pinton and S. Roux, arXiv:1112.1036 (2011).

Rev. Cub. Fis. **29**, 1E66 (2012) CONTRIBUTIONS

NUMERICAL STUDIES OF AEROFRACTURES IN POROUS MEDIA

ESTUDIOS NUMÉRICOS DE AEROFRACTURAS EN MEDIOS POROSOS

M. J. Niebling[a,b,c †], R. Toussaint[b,c,d], E. G. Flekkøy[a,d] and K. J. Måløy[a,d]

a) Department of Physics, University of Oslo, P.O. Box 1048, 0316 Oslo, Norway, Michael.Niebling@fys.uio.no[†]
b) Institut de Physique du Globe de Strasbourg, CNRS
c) University of Strasbourg, 5 rue Descartes, 67084 Strasbourg Cedex, France
d) Centre for Advanced Study at the Norwegian Academy of Science and Letters, Drammensveien 78, 0271 Oslo, Norway
† corresponding author

During the hydraulically induced compaction of a granular layer fracture patterns arise. In numerical simulations we study how these patterns depend on the gas properties as well as on the properties of the porous medium. In particular the relation between the speed of fracture propagation and injection pressure is here studied in detail.

Durante la compactación hidráulicamente inducida de una capa granular surgen patrones de fractura. En éste artículo estudiamos cómo éstos patrones dependen tanto de las propiedades del gas como de las del medio, utilizando simulaciones numéricas. En particular, estudiamos en detalle la relación entre la presión de inyección y la velocidad de propagación de la fractura.

PACS: Pattern formation in complex systems, 89.75.Kd; flow through porous materials, 47.56.+r; compressible flows, 47.40.-x

INTRODUCTION

Stress induced by fluid or gases can cause diverse materials to break and fracture. Such hydraulic fractures are a natural and common phenomenon in the field of volcanism and are artificially initiated to enhance the recovery of natural gas and mineral oil by fracturing the reservoir rock with pressurized fluids. Recently a new perspective on hydrofractures was added with the storage of supercritical CO_2 attracting the interest of an increasing number of researchers. In this respect two scenarios are considered. First it is one option to inject CO_2 into existing hydrofractures, and second the injection of the CO_2 can create additional fractures [1, 2]. The typical components for such fractures are a porous material and a compressible gas. Injection of pressurized fluids in a porous material, deforming beyond the elastic limit, has been studied in granular materials in Hele-Shaw cells, [3–8], with the injection of air or oil in systems with open boundary conditions, and during cyclic loading [9]. It was also studied in systems with a confinement for the grains, prevented from getting out of the cell, which allowed to observe the formation of thin fractures [10]. In this paper [10] it was found and discussed a criterion that the porous media and the fluid need to fulfill to allow the formation of fractures. For this purpose the gas' viscosity was varied. It was further discussed how the shape of the fractures depend on the properties of the porous material and of the injected gas in simple 2 dimensional (2D) numerical simulations.

In contrast to the previous article we will not change the properties of the injected gas or the porous material in this present article. Here we explore in particular the effect of the amplitude of the fluid pressure imposed in the source on the fracture morphology. Furthermore, all simulations here will be ran in a regime where fractures are created.

SIMULATION SETUP

As shown in Fig. 1 the setup consists of a cell with two glass plates separated by 1 *mm*. The gap between the plates is filled with particles. The empty space between the grains is saturated with a fluid that has the same properties as the fluid that is injected. Consequently, the only two media involved in the dynamics are the grains and the fluid. At the start of the simulations the average solid volume fraction of the grains is $\rho_s^{(0)} = 0.42$. This starting solid volume fraction is homogeneous with negligible density fluctuations although the particles are at random positions. The value of $\rho_s^{(0)} = 0.42$ is chosen to be less than the possible maximum of $\rho_s^{(\max)} = 0.60$ to allow compaction of the grains. On the inlet side of the cell the pressure is increased from a value of $P_I = 0.5 \times 10^5$ *Pa* to a value of $P_I = 2.5 \times 10^5$ *Pa* above the atmospheric pressure of $P_0 = 1.0 \times 10$ *Pa*. On the opposing side to the inlet the cell has an open boundary for the fluid but particles are not able to leave the cell here. In a real experiment, this could be achieved by using a net with a mesh smaller than the particles. The remaining boundaries are completely sealed for both media. In the simulation around 200 000 grains of diameter 140 ± 10% *μm* are involved. Finally, the pressure at the inlet is increased and maintained as a step function in time, at a steep ramp, and particles hardly move before the maximum injection pressure P_I is reached.

THEORY AND MODEL

Using a well tested numerical model we have the freedom to explore the parameter space independently. The details of the method can be found in [6, 11-17], and alternative models can be found in [18-22]. The model describes the fluid in terms of a pressure field while the porous medium is modeled by simulating discrete particles.

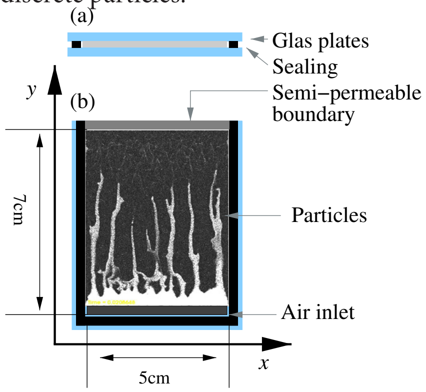

Figure 1: Numerical setup of the system.

THEORY AND SIMULATIONS

Dynamics of the gas phase. The equation for the evolution of the pressure $P = \tilde{P} + P_0$, where P_0 is the atmospheric pressure and $\tilde{P}$ the local pressure fluctuations is given by

$$\phi\left[\frac{\partial P}{\partial t} + \boldsymbol{u}\cdot\nabla P\right] = \nabla\cdot\left[P\frac{\kappa}{\mu_f}\nabla P\right] - P\nabla\cdot\boldsymbol{u} \qquad (1)$$

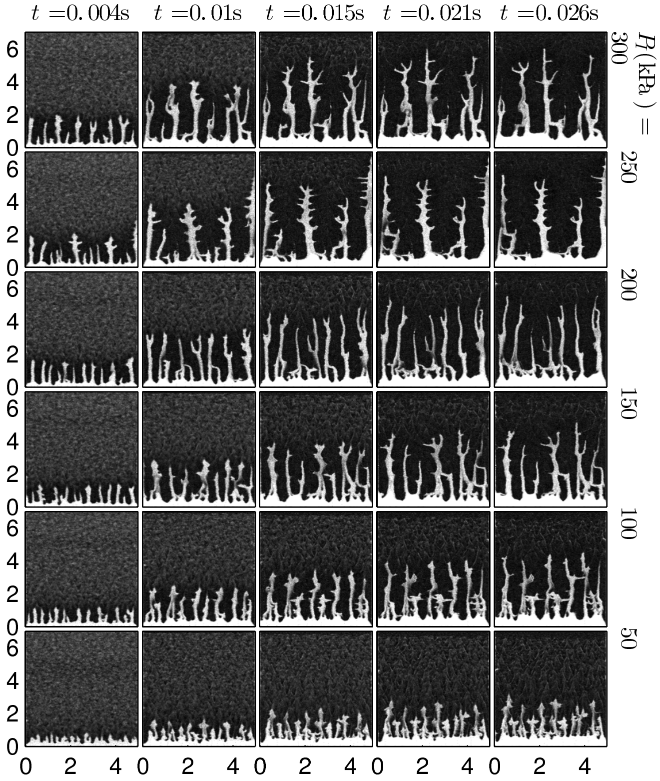

Figure 2: Snapshots during the simulations of the particle density in the Hele-Shaw cell, displayed for decreasing injection pressure P_I from top to bottom and as a function of time (left to right). Low particle density appears brighter in the snapshots. Under air injection, fractures, fingers and dispersed bubbles of low particle density emerge and propagate. *x*- and *y*-axis units are given in *cm*. The *y*-axis specifies the distance from the inlet.

In this equation, the pressure is described in terms of the local granular velocity $\boldsymbol{u}$, the viscosity μ_f of the gas, the local porosity $\phi = 1 - \rho_s$ and the local permeability κ. Eq. (1) is derived from mass conservation of the gas and the granular medium and by assuming a local Darcy law.

Dynamics of the particles. For the particles we basically use Newton's second law

$$m\frac{dv_p}{dt} = \boldsymbol{F_I} + \boldsymbol{F_d} + \boldsymbol{F}_a - \frac{\nabla P}{\rho_n}, \qquad (2)$$

with particle velocity v_p, particle mass m, particle mass density ρ_m, cell spacing h and the number density $\rho_n = \rho_s\rho_m/m$. $\boldsymbol{F_I}$ are linear inter-particle solid contact forces. $\boldsymbol{F_d}$ is a viscous damping force during particle collisions. For F_a, the interaction with the side plates we assume that the normal stress $P_g^{\perp}$ in the granular packing is proportional to the in-plane stress $P_g^{\parallel}$ by a factor λ (Janssen hypothesis). Using further a Coulomb friction model we state that the frictional force F_a per particle with the glass plates is proportional to the normal stress by a friction coefficient γ. With these two assumptions we find an expression for the friction force with the side plates.

$$F_a \leq \gamma S_a(2P_g^{\perp} + \rho_m gh) = \gamma S_a(2\lambda P_g^{\parallel} + \rho_m gh). \qquad (3)$$

$S_a = \pi a^2$ is the contact area of the particles with the plates.

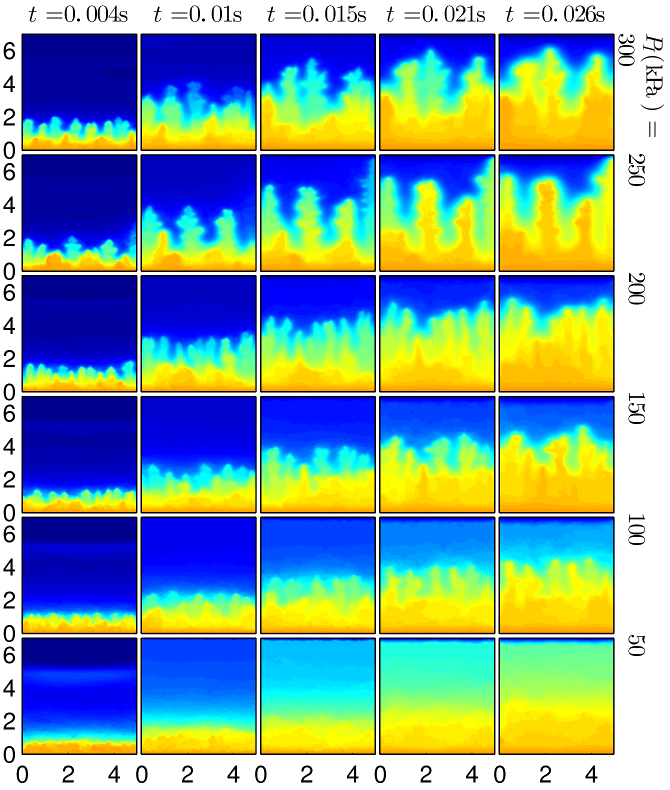

Figure 3: The pressure evolution for decreasing injection pressure P_I (top to bottom) and as a function of time (left to right). High pressure appears yellow (brighter) in the snapshots. *x*- and *y*-axis units are given in *cm*.

RESULTS

We ran a set of six simulations for injection pressures of P_I = (0.5, 1.0, 1.5, 2.0, 2.5, 3.0) × 10^5 *Pa* above atmospheric pressure P_0, a fluid viscosity of μ_f = 18.0 *mPa·s* and a friction coefficient with the side plates of $\gamma\lambda = 4.0$. The injected gas is considered as an ideal gas and has the compressibility of air $\beta_T = 1/P_0$ at P_0. The value of P_I at the inlet is reached very fast and particles start to move shortly after. During this compression of the particles fractures emerge in the granular packing. In Fig. 2 a set of snapshots of the particle density is shown. The snapshots are taken at increasing time from left to right. Each horizontal row of pictures corresponds to one of the six simulations at a different injection pressures. In Fig. 3 snapshots of the corresponding pressure field in the cell are displayed. The pressure field is normalized to one to allow a qualitative comparison.

In these plots an apparent feature is the different propagation speed and position of the emerging fractures. A high injection pressure causes the fractures to propagate faster. To quantify this observation we can plot the position of the most advanced finger tip as a function in time. This is done in Fig. 4. The plot clearly proves the previous observation. Furthermore it turns out that the systematic increase of the propagation speed is also proportional to the square root of the injection pressure. This is checked in Fig. 5. Here the rescaling of the fracture tip position by the square root of the injection pressure $\sqrt{P_I}$ results in a collapse of the graphs. The disagreement at the later stages of the simulations in this plot results from the finite size of the system, which allows fractures to grow only up to a certain size. Finally we can state that the fingers grow according to

$$Y_t = \sqrt{P_I}\, f(t), \tag{4}$$

where *f(t)* is a function which appears in the plots to be almost linear at early stages of the finger growth for $t < 0.01\ s$.

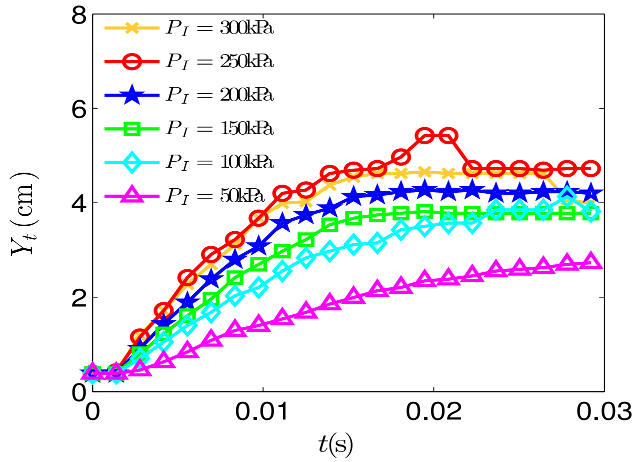

Figure 4: The position of the most advanced finger/fracture as a function of time at different injection pressure P_I. The higher the injection pressure P_I the further fingers grow.

In Fig. 2 we also observe that the fingers at high injection pressure propagate further into the packing before complete compaction of the grains takes place. This can be also seen in Fig. 4 where the finger position stops growing at longer distances from the inlet the higher the injection speed is.

Apart from the finger position, the increase of the injection pressure also affects the shape of the fingers. In Fig. 2 it can be seen that the fingers get more branched and fracture-like at higher injection pressure. At low injection pressure fingers appear to be straighter while increasing the injection pressure, fingers develop more and more branches. At the highest injection pressure of $P_I = 3.0 \times 10^5\ Pa$ the fingers clearly show characteristics of fractures.

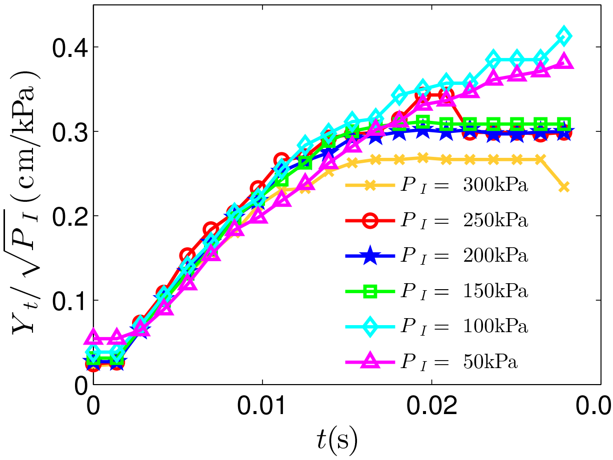

Figure 5: The position of the most advanced finger/fracture rescaled by the square root of the injection pressure $\sqrt{P_I}$. As a function of time the graphs at different injection pressure P_I collapse onto a single graph.

At high injection pressure P_I the pressure gradients are the largest. When the boundary is deformed the expected changes of the pressure gradients are therefore also higher at high injection pressure than at low injection pressure. At low P_I, one expects a lower pressure gradient everywhere, and thus a low effect of seepage forces and a slower deformation. Leading to overall smoother pressure gradients and a more stable front deformation. We thus expect faster finger propagation, and more branching at a higher injection pressure.

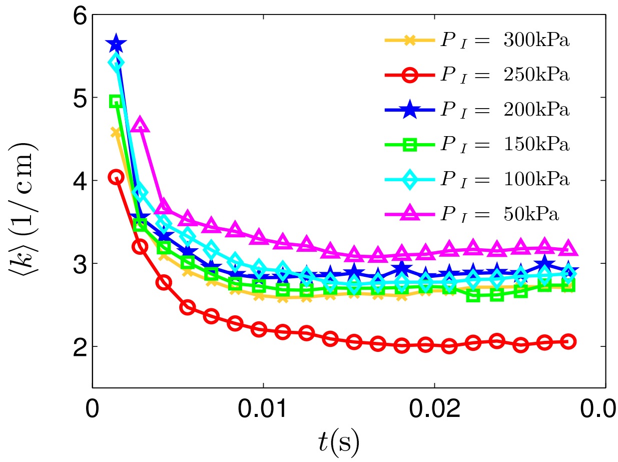

Figure 6: The average of the spatial finger wavenumber in x direction.

Finally also the spatial distance between the fingers depends on the injection pressure (see Fig. 6). At low injection pressure the number of fingers is higher than at high injection pressure, as can be also seen in Fig. 2. In general the finger spatial frequency decreases in time after injection has started and fingers propagate through the cell. This can be shown by calculating the average of the characteristic spatial finger wavenumber in x direction. First the powerspectrum S_j of each horizontal line j of the particle density is calculated. Taking the average of these power spectra results in a single power spectrum $\overline{S}$. From this average distribution of wave numbers the characteristic wave number $\langle k \rangle$ in x-direction is defined and calculated in the following way, using an average of k with the power spectra as a weight

$$\langle k \rangle = \frac{\sum_k k\bar{S}(k)}{\sum_k \bar{S}(k)}. \tag{5}$$

The results in Fig. 6 show a decrease of finger frequency in time. As a trend we notice that at higher injection pressure the finger frequency decreases faster than at low injection pressure. However the simulation at $P_I = 250\ kPa$ differs from the other simulations. In this simulation we also observe a finger propagating directly along the right boundary in Fig. 2. Close to the wall this finger appears to propagate faster than the other fingers in this simulation. Because the simulation at $P_I = 250\ kPa$ is the only simulation where this appears it also stands out in the plots for the average wave number Fig. 6. This is presumably due to a finite size effect, and such outlier is frequently met in granular systems, which are known to present a large variability and sensitivity on details of the initial state. (see e.g. [17]). Otherwise for higher injection pressure does the finger frequency not only decreases faster but also drops to a lower value before the grains get compacted.

This coarsening of the finger frequency is the result of two mechanisms. First the pressure gradient between the finger tip and the outlet gets higher the closer the finger tip moves to the outlet. Assuming a linear pressure profile though the porous media the pressure would drop to zero on a shorter and shorter distance the closer the finger advances to the outlet. At the same time the gas also leaks into the side walls of the finger. This increases the pressure in the porous material around a finger. In the areas where this pressure increase takes place less advanced neighboring fingers would thus experience a lower pressure gradient. The speed of this fingers is thus reduced. This means the more a finger advances to the outlet the faster it moves. At the same time the pressure increase in the area around an advanced finger decreases the pressure gradient in front of less advanced fingers. This causes the less advanced fingers to propagate slower or to stop completely. This mechanism will result in a coarsening of the finger frequency. Further more we expect this mechanism to be active on a typical length scale which is comparable to the skin depth of the pressure profile. This mechanism also appears in the basic Saffman Taylor instability [23].

A second mechanism that will account for a coarsening of the finger frequency is the compaction of the grains on the sides of a finger. During the propagation the finger width increases and branches at a 90 degree angle arise on the sides of fingers. This compacts the granular material on the sides of an advancing finger. How far this compaction propagates on the sides depends on the properties of the granular material and also on the finger width and how the side branches develop. Where this compaction has occur preceding fingers are slowed down or stopped. The size of the compaction front around the fingers sets a second length scale for the coarsening of the finger frequency.

CONCLUSIONS

The increase of the injection pressure primarily causes fingers to propagate faster through the granular packing. Fingers at high injection pressure also tend to be more branched and fracture-like than the fingers at low injection pressure. It was shown that the position of the fracture propagation in time increases with the square root of the injection pressure $\sqrt{P_I}$. Furthermore we discussed the observed coarsening of the characteristic spatial finger wavenumbers in terms of two mechanisms. A first mechanism that controls the coarsening arises from the fluid seepage into the granular media. Where the length scaled for this mechanism was argued to be of the size of the pressure skin depth. To further explain the coarsening a second mechanism causing the coarsening of the finger wavenumber was highlighted. This second mechanism introduces a length scale for the coarsening with the size of the compaction front in the granular material around a finger.

ACKNOWLEDGMENTS

We thank Gustavo Sanchez-Colina for help about the Spanish grammar.

---

[1] M. Bickle, A. Chadwick, H. E. Huppert, M. Hallworth and S. Lyle, Earth Planet. Sci. Lett. **255**, 164 (2007).
[2] F. C. Boait, N. J. White, M. J. Bickle, R. A Chadwick, J. A. Neufeld and H. E. Huppert, J. Geophys. Res. B: Solid Earth **117**, B03309 (2012).
[3] E. Lemaire, Y. O. M. Abdelhaye, J. Larue, R. Benoit, P. Levitz and H. Van Damme, Fractals **1**, 968 (1993).
[4] X. Cheng, L. Xu, A. Patterson, H. M. Jaeger and S. R. Nagel, Nat. Phys. **4**, 234 (2008).
[5] H. Huang, F. Zhang, P. Callahan and J. Ayoub, Phys. Rev. Lett. **108**, 258001 (2012).
[6] Ø. Johnsen, R. Toussaint, K. J. Måløy and E. G. Flekkøy, Phys. Rev. E **74**, 011301 (2006).
[7] Ø. Johnsen, C. Chevalier, A. Lindner, R. Toussaint, E. Clément, K. J. Måløy, E. G. Flekkøy and J. Schmittbuhl, Phys. Rev. E **78**, 051302 (2008).
[8] Ø. Johnsen, R. Toussaint, K. J. Måløy, E. G. Flekkøy and J. Schmittbuhl, Phys. Rev. E **77**, 011301 (2008).
[9] A. Nermoen, C. Raufaste, S. D. de Villiers, E. Jettestuen, P. Meakin and D. K. Dysthe. Phys. Rev. E **81**, 061305 (2010).
[10] M. J. Niebling, R. Toussaint, E. G. Flekkøy and K. J. Måløy, Phys. Rev. E (submitted).
[11] M. J. Niebling, E. G. Flekkøy, K. J. Måløy and R. Toussaint, Phys. Rev. E **82**, 011301 (2010).
[12] M. J. Niebling, E. G. Flekkøy, K. J. Måløy and R. Toussaint, Phys. Rev. E **82**, 051302 (2010).
[13] J. L. Vinningland, R. Toussaint, M. J. Niebling,

E. G. Flekkøy and K. J. Måløy, European Phys. J. Special Topics **204**, 27 (2012)

[14] S. McNamara, E. G. Flekkøy and K. J. Måløy, Phys. Rev. E **61**, 4054 (2000).

[15] J. L. Vinningland, Ø. Johnsen, E. G. Flekkøy, R. Toussaint and K. J. Måløy, Phys. Rev. Lett. **99**, 048001 (2007).

[16] J. L. Vinningland, Ø. Johnsen, E. G. Flekkøy, R. Toussaint and K. J. Måløy, Phys. Rev. E **76**, 051306 (2007).

[17] J. L. Vinningland, E. G. Flekkøy, R. Toussaint and K. J. Måløy, Phys. Rev. E **81**, 041308 (2010).

[18] M. A. van der Hoef, M. van Sint Annaland and J. A. M. Kuipers, Chem. Eng. Sci. **59**, 5157 (2004).

[19] N. G. Deen, M. van Sint Annaland, M. A. van der Hoef and J. A. M. Kuipers, Chem. Eng. Sci. **62**, 28 (2007).

[20] N. G. Deen, M. van Sint Annaland, M. A. van der Hoef and J. A. M. Kuipers, Prog. Comput. Fluid Dyn. **7**, 152 (2007).

[21] M. A. van der Hoef, M. van Sint Annaland, N. G. Deen and J. A. M. Kuipers, Ann. Rev. Fluid Mech. **40**, 47 (2008).

[22] C. Zeilstra, J. G. Collignon, M. A. van der Hoef and J. A. M. Kuipers, Powder Tech. **184**, 166 (2008).

[23] P. G. Saffman, G. Taylor, Proc. R. Soc. Lond. A **245**, 312 (1958).

REGISTERED PARTICIPANTS AT March*COM*eeting’12

Argentina (3)	
M. A. Aguirre	UBA
I. Ippolito	UBA
G. Miño	ESPCI (temporary)
Brazil (2)	
M. N. Moura	UFPE
G. L. Vasconcelos	UFPE
Colombia (1)	
A. Castro	ESPCI (temporary)
Cuba (23)	
E. Altshuler	University of Havana/CAS
A. J. Batista-Leyva	Instec
A. Batista	University of Havana
A. Borroto	University of Havana
L. Cruz	University of Havana
O. Díaz	Institute of Meteorology
R. Díaz-Méndez	CUJAE
E. Dominguez	University of Havana
N. Figueroa	University of Havana
K. García	CIM
A. González	University of Havana
A. Henrnández	University of Havana
A. Lage	University of Havana
A. Lam	University of Havana
K. León	CIM
E. Martínez	University of Havana
J. M. Nieto-Villar	University of Havana
L. del Río	University of Havana
A. Rivera	University of Havana
G. Sánchez	University of Havana
O. Sotolongo	University of Havana
F. Tejera	University of Havana
H. Torres	University of Havana
Denmark (2)	
M. H. Jensen	Niels Bohr Institute
J. Mathiesen	Niels Bohr Institute
France (14)	
S. Atis	FAST
E. Clement	ESPCI
H. Van Damme	ESPCI
O. Dauchot	ESPCI
P. Dommersnes	University of Paris-Diderot/CAS
E. Fort	ESPCI
J. Ch. Geminard	University of Lyon
M. Hoyos	ESPCI
O. Ramos	University of Lyon
B. SaintYves	CEA-Saclay
S. Santucci	ENS-Lyon/CAS
P. Tabeling	ESPCI
R. Toussaint	IPGS/CAS
L. Tuckerman	ESPCI
Mexico (2)	
C. Ruiz-Suárez	CINVESTAV-Monterrey
J. L. Arauz-Lara	University of San Luis Potosí
Norway (17)	
J. Bergli	University of Oslo
R. Castberg	University of Oslo
J. A. Eriksen	University of Oslo
E. G. Flekkøy	University of Oslo/CAS
J. O. Fossum	NTNU/CAS
G. Helgesen	IFE/University of Oslo/CAS
H. Hemmen	NTNU
T. H. Johansen	University of Oslo/CAS
K. D. Knudsen	IFE/CAS
H. Mauroy	IFE
K. J. Måløy	University of Oslo/CAS
M. J. Niebling	University of Oslo
S. Raaen	NTNU
Z. Rozynek	NTNU
B. Sandnes	NTNU
J. I. Vestgården	University of Oslo
V. V. Yurchenko	University of Oslo
Spain (1)	
J. Iñiguez	University of Salamanca
UK (2)	
D. Barkley	University of Warwick
I. Guillamón	University of Bristol
USA (8)	
R. Behringer	Duke University
D. Durian	University of Pennsylvania
H. Jaeger	University of Chicago
L. P. Kadanoff	University of Chicago
R. Pynn	Indiana University/CAS
G. Reiter	University of Houston
T. Shinbrot	Rutgers University
S. Waitukaitis	University of Chicago

Poster session. (Photo: O. Ramos)